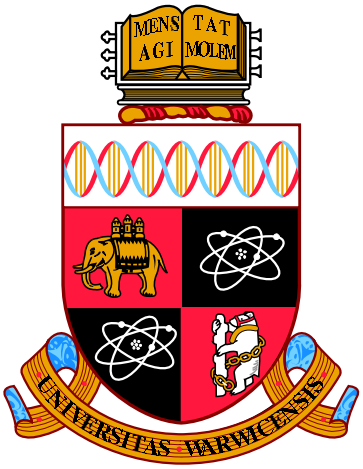

Band alignments within 2-dimensional van der Waals heterostructures

by

Natalie Christine Teutsch

Thesis

Submitted to the University of Warwick

for the degree of

Doctor of Philosophy

Department of Physics

January 2020

WARWICK
THE UNIVERSITY OF WARWICK

Contents

List of Tables

List of Figures

Acronyms

μ-ARPES	micro angle-resolved photoemission spectroscopy.
1D	1-dimensional.
2D	2-dimensional.
AFM	atomic force microscopy.
ARPES	angle-resolved photoemission spectroscopy.
BL	bilayer.
BP	black phosphorus.
BZ	Brillouin zone.
CB	conduction band.
CBM	conduction band minimum.
CVD	chemical vapour deposition.
DFT	density-functional theory.
DOS	density of states.
FET	field effect transistor.
hBN	hexagonal boron nitride.
HS	heterostructure.
IMFP	inelastic mean free path.
KFGM	Kelvin force gradient microscopy.
LED	light emitting diode.
ML	monolayer.
OSA	order sorting aperture.

PC	polycarbonate.
PDMS	polydimethylsiloxane.
PL	photoluminescence.
PVD	physical vapour deposition.
SOC	spin-orbit coupling.
SPCM	scanning photocurrent microscopy.
SPEM	scanning photoemission microscopy.
SPIM	scanning photocurrent microscopy.
SPM	scanning probe microscopy.
STM	scanning tunnelling microscopy.
STS	scanning tunnelling spectroscopy.
TL	trilayer.
TMD	transition metal dichalcogenide.
UHV	ultra-high vacuum.
VB	valence band.
VBM	valence band maximum.
XPS	X-ray photoemission spectroscopy.

Acknowledgments

I owe a great deal of thanks to a great many people for supporting me during my PhD. Firstly, I would like to thank my supervisor, Dr. Neil Wilson, without whom none of this would have been possible. His support and instruction helped me throughout my PhD, and I appreciate every second of time and patient guidance that he gave me.

I'd also like to thank the whole Microscopy group here at Warwick, including the academics, students and technicians who helped me and made me feel so welcome. I'd like to thank Xue and Abi, who joined me on many synchrotron runs, for helping to get us through those late nights together!

In that vein, I would also like to thank all the staff at the synchrotrons I visited, especially Alexei Barinov at Elettra and Pavel Dudin at Diamond. Their expertise and instruction was crucial to my work, and helped make these experiments possible.

I'd like to thank my friends, as they have played a large part in keeping me sane during this PhD. I would like to thank Punit for his immeasurable support, kindness, and friendship along the way. You've helped me far more than I can say. Thanks, also, to the Lunch crew for providing daily entertainment and b...eers to keep me going. Thanks to Lisa, Sophie and Catherine for always being there to talk to, usually over a cocktail or two.

Lastly, I'd like to thank my family, which has continued to grow and provide more support with every new addition. Thanks to my siblings, old and new, for the comfort and amusement they bring. And finally, thank you to my mother and father for their unquestioning love and encouragement throughout my life.

Declarations

I declare that this thesis contains an account of my research work carried out at the Department of Physics, University of Warwick, between October 2015 and September 2019 under the supervision of Dr. N. R. Wilson. The research reported here has not been previously submitted, wholly or in part, at this or any other academic institution for admission to a higher degree.

Parts of this thesis have been published by the author between October 2015 and September 2019:

- Nguyen, P. V., Teutsch, N. C., Wilson, N. P., Kahn, J., Xia, X., Graham, A. J., Kandyba, V., Giampietri, A., Barinov, A., Constantinescu, G. C., Yeung, N., Hine, N. D. M., Xu, X., Cobden, D. H., Wilson, N. R. Visualizing electrostatic gating effects in two-dimensional heterostructures. *Nature* **572**, 220 (2019).

Other parts of the thesis are to be published shortly:

- Teutsch, N. C., Nguyen, P. V., Wilson, N. P., Kahn, J., Xia, X., Graham, A. J., Kandyba, V., Giampietri, A., Barinov, A., Constantinescu, G. C., Yeung, N., Hine, N. D. M., Xu, X., Cobden, D. H., Wilson, N. R. Field-dependent band-structure measurements across two-dimensional heterostructures. (In preparation, for submission to *Nano Letters*.)

- Teutsch, N. C., Nguyen, P. V., Nunn, J., Graham, A. J., Xia, X., Kandyba, V., Giampietri, A., Barinov, A., Dudin, P., Hoesch, M., Xu, X., Cobden, D. H., Wilson, N. R. Photo-current during angle-resolved photoemission spectroscopy with in-situ gating. (In preparation, for submission to *Journal of Synchrotron Radiation*.)

All the work presented here was completed by myself, except for the following:

- The ARPES data was acquired with the help of V. Kandyba, A. Giampietri, and A. Barinov at Elettra Sincrotrone, P. Dudin and M. Hoesch at Diamond Light Source and M. Ascensio, J. Avila, and A. Levy at Synchrotron Soleil.
- The majority of exfoliated samples were made by P. V. Nguyen as part of D. H. Cobden's group at the University of Washington.
- Photoluminescence data was obtained by D. H. Cobden's and X. Xue's groups at the University of Washington.
- The sample shown in Fig. 2.15 was made by K. Novoselov's group at the University of Manchester.
- DFT and GW calculations were performed by G. C. Constantinescu, N. Yeung and N. D. Hine at the University of Warwick.

Additional publications the author has contributed to (not contained within this thesis) between October 2015 and September 2019:

- Hamer, M. J., Zultak, J., Tyurnina, A. V., Zólyomi, V., Terry, D., Barinov, A., Garner, A., Donoghue, J., Rooney, A. P., Kandyba, V., Giampietri, A., Graham, A. J., Teutsch, N. C., Xia, X., Koperski, M., Haigh, S. J., Fal'ko, V. I., Gorbachev, R. V., Wilson, N. R. Indirect to Direct Gap Crossover in Two-Dimensional InSe Revealed by Angle-Resolved Photoemission Spectroscopy *ACS Nano* **13** 2, 2136 (2019).
- Rösner, B., Dudin, P., Bosgra, J., Hoesch, M., David, C. Zone plates for angle-resolved photoelectron spectroscopy providing sub-micrometre resolution in the extreme ultraviolet regime *Journal of Synchrotron Radiation* **26** 2, 467 (2019).

Abstract

Since graphene's discovery in 2004, a new world of 2-dimensional (2D) materials has been discovered. These new materials range from metals, semi-metals, semiconductors and insulators, and reveal new physics and possibilities in the world of 2D electronics. Transition metal dichalcogenides (TMDs) are a family of materials which stand out as potential candidates for 2D device design. A subgroup within this family, MX_2 layers (M for the transition metal element, X for the chalcogen element) are made up of covalently bonded MX_2 sheets held together vertically by weaker van der Waals bonds. They are easy to isolate as monolayers (MLs) and have a number of interesting electronic features, including being direct bandgap semiconductors in their ML form. These MLs can be stacked into van der Waals heterostructures (HSs) to form a range of functioning 2D devices.

Here, *in situ* angle-resolved photoemission spectroscopy (ARPES) with electrostatic doping has been used to directly measure the electronic structure of MX_2 MLs and HSs and study both carrier concentration and field dependent effects. The band structure of exfoliated ML MX_2 materials have been characterised, along with the layer dependent electronic structure of WS_2 and WSe_2. Using this technique, the band alignments within a number of 2D HSs have been measured, including gr/MX_2 and MX_2/MX_2 HSs.

In situ gated ARPES measurements of electrostatically gated MX_2 MLs and HSs are reported. By controlling the carrier concentration within these flakes, the conduction band of these materials has been directly resolved, enabling measurement of the bandgap for WS_2, WSe_2, MoS_2 and $MoSe_2$. These values have been long disputed in literature, in part due to bandgap renormalisation; an effect observed here in WSe_2. By controlling the carrier concentration, direct measurements of the layer dependent transition from indirect to direct bandgap were made. textitIn situ gating probed the field dependent effects of MX_2 MLs by observing the gate dependent band shifts across HSs, showing that the flakes within these HSs act as capacitors in series to each other, a fact which could help future device design.

In situ ARPES was used here to study the origin and behaviour of photocurrent in 2D HSs. By measuring the current and the photon-assisted tunnelling through a functioning device, a model was formed to describe the generation and behaviour of carriers within the sample. Combining these measurements with other surface science techniques, such as Kelvin force gradient microscopy (KFGM), gave insight into the electronic behaviour within HSs and can be used to identify conductive and insulating regions, as well as study gate dependent effects and effective geometry for charge dissipation within HSs.

Combining these results demonstrates that *in situ* gated ARPES is a powerful technique for studying 2D materials and HSs as it effectively probes their band structure, band alignments and interlayer effects. This helps to develop our understanding of the fundamental physics behind these 2D materials and could help improve future device design.

Chapter 1

Introduction

1.1 Introduction

The 2010 Nobel Prize in Physics was awarded to Andre Geim and Konstantin Novoselov "for ground-breaking experiments regarding the two-dimensional material graphene" [1]. The award focused on their work in isolating graphene in its monolayer (ML) form, using adhesive tape to exfoliate bulk graphite, then studying the effect of changing carrier concentration by electrostatically doping the sample through the use of a back gate. This opened the door for research into 2-dimensional (2D) materials and a vast catalogue of new 2D materials have subsequently been discovered, developed and synthesised including; metals, semi-metals, insulators, semiconductor and even superconductors [2–5]. There is great interest in studying the fundamental physical, optical, electronic and thermal properties of these new materials, such as their layer dependent band structure, spin splitting effects, valley physics and even quantum confinement [3, 4, 6].

Beyond the MLs themselves, research is also exploring the potential for stacking MLs into vertical 2D heterostructure (HS) held together by van der Waals forces. These HSs can effectively modify and even enhance the electronic capabilities of the constituent materials and open the door to probing interlayer band alignment, interlayer coupling, exciton behaviour and contact engineering. These HSs also facilitate the design and creation of new 2D applications from electronic and optoelectronic devices, tunnelling devices including field effect transistors (FETs), photodiodes, light emitting diodes (LEDs) and even flexible electronics.

This new area of research and device creation relies heavily on the ability to change carrier concentration through electrostatically doping the sample, just as Novosleov and Geim did originally. The back-gate geometry employed in their study

of graphene is still used widely as a contact in a range of studies. The control the gate provides over electric field and carrier concentration is especially important for 2D materials because they typically have a low density of states (DOS), which is easily manipulated. The gating is therefore crucial, as the easy manipulation of DOS and chemical potential enables a wide range of fundamental physics to be explored and helps to improve device design and operation.

In order to develop our understanding of these new materials, we need to be able to measure the electronic properties in 2D materials and how they change in 2D HSs and devices. The measurement of these electronic structures will be the focus of this work, using *in situ* gated angle-resolved photoemission spectroscopy (ARPES) to measure electrostatically doped 2D materials and HSs.

1.2 2D materials

1.2.1 Graphene

The first material to be isolated and studied in its ML form was graphene [7]. Exfoliated from its bulk forebearer graphite, graphene is made up of a single layer of sp^2-bonded carbon atoms arranged in a 2D crystalline honeycomb lattice composed of two interspersed triangular sub-lattices; A and B, as illustrated in Fig. 1.1 a).

Each carbon atom is bound to its nearest neighbours by 3 covalent σ bonds, with an average bond length $a_0 = 1.42\,\text{Å}$, which are formed by the hybridisation of one s and two p electron orbitals [8]. The remaining unbound electron on each carbon atom forms delocalised π bands which are responsible for graphene's electronic band structure. The unit cell of graphene has a two atom basis, one from each of the independent A and B sub-lattices. The lattice vectors for the unit cell are:

$$\mathbf{a}_1 = \frac{a_0}{2}(3, \sqrt{3}),\ \mathbf{a}_2 = \frac{a_0}{2}(3, -\sqrt{3}) \tag{1.1}$$

which both have a magnitude given by the lattice constant, $a = \sqrt{3}a_0 = 2.46\,\text{Å}$ [8, 9].

In reciprocal, or k-, space graphene's lattice vectors become:

$$\mathbf{b}_1 = \frac{2\pi}{3a_0}(1, \sqrt{3}),\ \mathbf{b}_2 = \frac{2\pi}{3a_0}(1, -\sqrt{3}) \tag{1.2}$$

which have a magnitude of $2.95\,\text{Å}^{-1}$.

Two high symmetry points which are particularly interesting for graphene

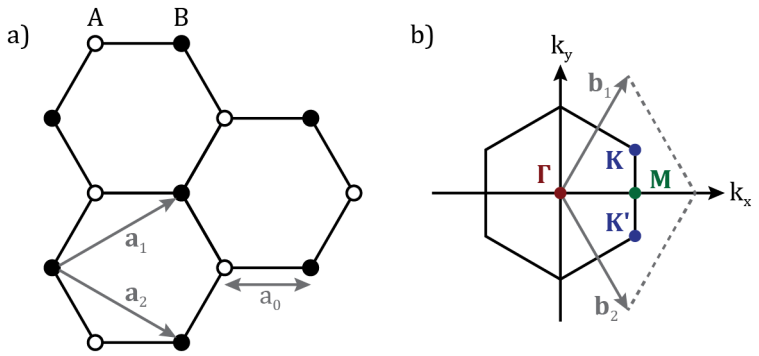

Figure 1.1: a) The crystal structure of graphene showing the A and B sub-lattices, the C-C bond length a_0, and the unit cell vectors, $\mathbf{a}_1$ and $\mathbf{a}_2$. b) Graphene's hexagonal 2D BZ highlighting the following critical points: $\mathbf{\Gamma}$ at the centre, $\mathbf{K}$ and $\mathbf{K'}$ at alternating corners (also known as the Dirac points), and $\mathbf{M}$ which lies in the centre between the two corners. Also shown are graphene's reciprocal lattice vectors, $\mathbf{b}_1$ and $\mathbf{b}_2$.

are the Dirac points at $\mathbf{K}$ and $\mathbf{K'}$ which are located at the corners of the hexagonal Brillouin zone (BZ), shown in Fig. 1.1 b). Their positions are given by:

$$\mathbf{K} = \left(\frac{2\pi}{3a_0}, \frac{2\pi}{3\sqrt{3}a_0}\right), \ \mathbf{K}' = \left(\frac{2\pi}{3a_0}, -\frac{2\pi}{3\sqrt{3}a_0}\right) \tag{1.3}$$

and are of particular importance for graphene's electronic characteristics [8].

Graphene's electronic structure can be determined by applying the tight binding approach to the half-filled π bands. Two independent Bloch wavefunctions for the inequivalent A and B sub-lattices are constructed and superimposed onto one another, while only considering nearest neighbour interactions, to give a total eigenfunction for the system [10]. The resultant dispersion relation can be written as [9]:

$$E(k_x, k_y) = \pm t\sqrt{1 + 4\cos\frac{k_x\sqrt{3}a}{2}\cos\frac{k_y a}{2} + 4\cos^2\frac{k_y a}{2}} \tag{1.4}$$

where t is the nearest neighbour overlap integral and k_x and k_y are wavevectors. This dispersion is shown in Fig. 1.2.

Also shown in Fig. 1.2 are the points where the dispersion relation reaches zero energy, called the Dirac points in graphene. At these points the valence and conduction bands meet to make graphene a zero bandgap semimetal. For small energies, close to the Fermi level, expansion about one of these points in k gives the following linear energy-momentum dispersion relation [11]:

$$E = \hbar v_{\mathrm{F}} |\mathbf{k}| \tag{1.5}$$

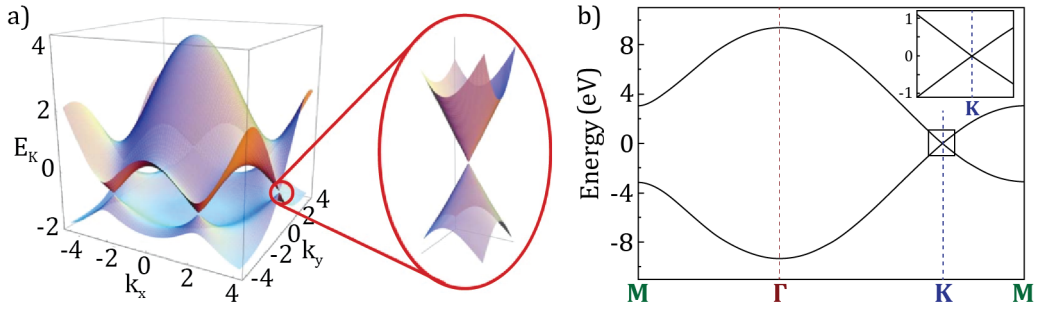

Figure 1.2: a) Band structure visualisation of graphene showing the valence and conduction band. Inset is close up of Dirac point, showing the bands meeting. Adapted from [8]. b) Valence and conduction band structure along the **M** - **Γ** - **K** - **M** direction of graphene's BZ. Inset showing linear dispersion relation around the Dirac point. Adapted from [10].

where E is the energy, $|\mathbf{k}|$ is the wavevector measured from **K**, v_F is the Fermi velocity and $\hbar$ is the reduced Plank constant.

This linear dispersion relation where the valence and conduction bands meet makes graphene very attractive to researchers as it resembles the behaviour of massless Dirac fermions [12]. For graphene, instead of the particles travelling at the speed of light, the electrons are travelling at a Fermi velocity of $v_\mathrm{F} = \frac{3ta}{2} \approx 1 \times 10^6\,\mathrm{ms}^{-1}$, lending graphene its remarkably high electron mobility [9]. From the dispersion relation in Eq. 1.5, the DOS of graphene, ρ, can be derived near the Dirac point and is given by the following [13]:

$$\rho = \frac{2}{\pi\left(\hbar v_\mathrm{F}\right)^2}|E|. \tag{1.6}$$

This dispersion relation importantly shows that the DOS increases linearly with energy, around the **K** points. For doped graphene, the change in carrier concentration, n, is given by

$$n = \frac{1}{\pi\left(\hbar v_F\right)^2}\left(E_\mathrm{D}\right)^2 \tag{1.7}$$

where E_D is the energy of the Dirac point measured relative to the Fermi level.

1.2.2 Boron Nitride

Hexagonal boron nitride (hBN), often referred to as 'white graphene', is another example of a bulk material from which one can isolate a single layer, either by bottom-up growth or top-down bulk exfoliation. hBN has the same hexagonal lattice as graphene, except that the carbon A and B sites are replaced with boron (B) and nitrogen (N) atoms respectively while still held tightly together by covalent

σ bonds. The same vectors given in Eq. 1.1, 1.2 and 1.3 may be used to describe hBN, but with a slightly larger lattice constant $a = 2.51\,\text{Å}$ [14].

While hBN has a similar physical structure to graphene, it is an insulator, or a large bandgap semiconductor, rather than a zero bandgap semimetal. The tight binding model can similarly be applied to hBN to estimate its band structure, though due to longer range effects between the alternating B and N atoms it is more appropriate to go up to third nearest neighbour approximations which opens a bandgap of 5.6 eV [15].

hBN is interesting not only for its standalone properties, but when stacked next to graphene within a device it has been shown to greatly improve the electrical properties [16], making it ideal to incorporate into HSs. The combination of graphene and hBN is particularly interesting as encapsulating graphene in hBN dramatically increases its mobility [17].

1.2.3 Transition metal dichalcogenides

There are a number of other 2D materials, one of the largest families is that of transition metal dichalcogenides (TMDs). Commonly referred to as MX_2 where M stands for the transition metal element and X for the chalcogen element; materials within this family consist of strong covalently bonded layers held together in vertical stacks by weaker van der Waals bonds. It is therefore often possible to break the van der Waals bonds and isolate a ML by exfoliation or synthesis using chemical vapour deposition or molecular beam epitaxy [18]. Of the MX_2 family, this study focuses on MoWSeS materials, where the M = Mo, W and X = Se, S. They are particularly stable and exhibit interesting electronic features, mentioned later.

Fig. 1.3 a) shows the top down view of a standard, hexagonal MX_2 crystal where blue and orange spheres for M and X atoms, respectively, and the unit cell highlighted with the yellow parallelogram. Fig. 1.3 b) shows the atoms within the blue triangle, illustrating the profile of a single ML consisting of a layer of X atoms on the top and bottom which are covalently bonded to a central M atom. Fig. 1.3 c) shows the BZ for these MLs, which is the same as graphene and hBN as they all have a 2D hexagonal crystal. The most common stable structure of these quasi-2D MLs is a 2H crystal structure, shown in Fig. 1.3 d). In bulk, each plane is rotated 180° to the next such that the unit cell contains two layers held together with van der Waals bonds. Other crystal phases such as 1T, 1T' and 3R are possible but will not be discussed here [18].

The MoWSeS materials have a number of interesting properties. They are semiconductors in both bulk and ML. However, as the number of layers decreases

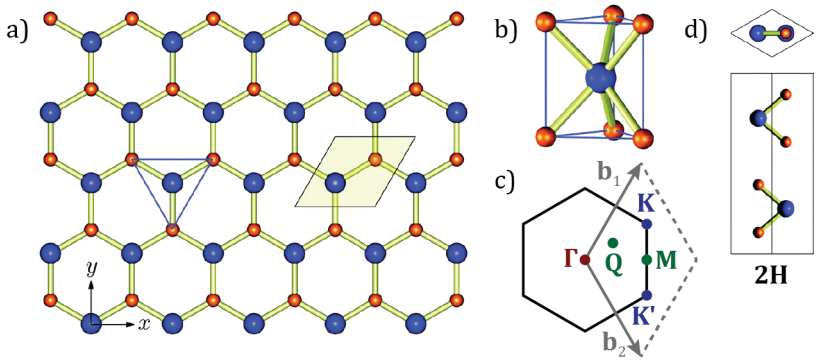

Figure 1.3: a) Top down view of a 2H-MX_2, with the unit cell shown in yellow. Blue and orange spheres are for the M and X atoms respectively. b) Side view of blue triangle in a), which shows the top and bottom X atoms bonded to a central M atom. These three layers: two of X atoms and one of M atoms, form a single MX_2 ML. c) First BZ of the 2H-MX_2 crystal structure, showing the high symmetry points: **Γ**, **Q**, **M**, **K** and **K′**. d) Top down, and side, view of the unit cell. Two MX_2 layers, rotated 180° to each other, form the bulk unit cell. Adapted from [18].

they go from having an indirect bandgap in bulk, and even down to bilayer (BL), to direct bandgap in ML. This is true for all four materials, and was first predicted theoretically for WSe_2 [19] and MoS_2 [20].

Fig. 1.4 shows the density-functional theory (DFT) predicted band structure of all four materials in for a) ML and b) bulk, where the purple arrows show the bandgaps. In bulk, the valence band maximum (VBM) is located at **Γ** while the conduction band minimum (CBM) is at **Q**, creating an indirect bandgap. As the number of layers decrease, the valence band (VB) at **Γ** shifts downward in energy while the conduction band (CB) at **Q** increases. Both the VB and CB at **K** remain largely unchanged with layer number, therefore in the MLs both the VBM and CBM shifts to **K**, giving rise to a direct bandgap.

The first experimental evidence of a direct bandgap was from photoluminescence measurements where MLs were found to have orders of magnitude increase in luminescence response compared to that of bulk [21, 22]. Due to the increased photoluminescence, the direct bandgap makes MLs particularly useful for optoelectronic devices and is one of the main reasons these materials are favourites in the drive towards 2D devices [3].

Another interesting feature of the electronic structure is a result in the change in symmetries from bulk to ML. Due to strong spin-orbit coupling (SOC) from the *d* orbitals of the metal atoms, the bands at **K** are spin split in ML and bulk and spin non-degenerate in ML. In ML, due to mirror symmetry conservation and time reversal symmetry breaking, the two **K** points, **K** and **K′**, are inequivalent and

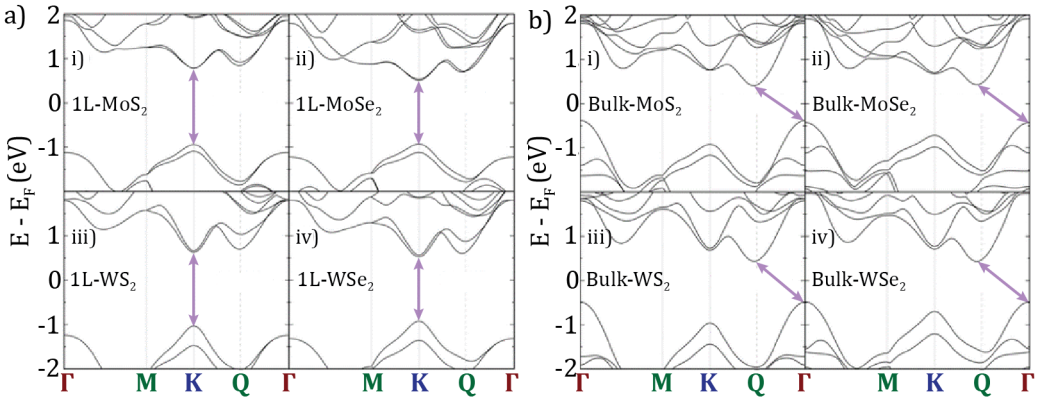

Figure 1.4: Predicted band structure of MoWSeS materials, showing the **Γ** - **M** - **K** - **M** - **Γ** direction for a) ML, and b) bulk. Purple arrows indicate the bandgaps for each. Adapted from [29].

have an alternating valley index [23]. Due to the interaction with SOC and valley pseudospin the spin index is locked to the valley index such that there is only spin up at **K** and only spin down at **K′**. This spin-valley locking results in valley-dependent optical selection rules where, depending on the chirality of circularly polarised light used, there will be optical excitation from either **K** or **K′** only [24, 25]. This interesting aspect of MLs could lead to novel application in the world of valleytronics [26–28].

1.2.4 Other 2D materials

There is a wide range of other bulk materials that can be isolated in ML form to get 2D materials beyond graphene and MoWSeS MLs [2, 3, 30]. The family of 2D materials ranges from metals such as NbS_2 [31], to semimetals such as M_2X_2 transition metal dichalcogenides (TMDs) [2] or WTe_2, other insulators like PbO or MoO_3, semiconductors from outside the MoWSeS family including other TMDs [4], SiC [2], black phosphorus (BP) [32] and even superconductors such as $TaSe_2$ and $NbSe_2$ [33, 34].

With such a wide range of attributes, one can pick and choose materials according to the desired electronic properties [4, 30]. However, in order to bring these materials into functioning 2D devices, we need to be able to make electrical contact, often with graphene, and have precise control over the device's electronic properties. This can be achieved by stacking different MLs together, in a specific order and arrangement, in order to get the desired electronic features and control [18, 35, 36].

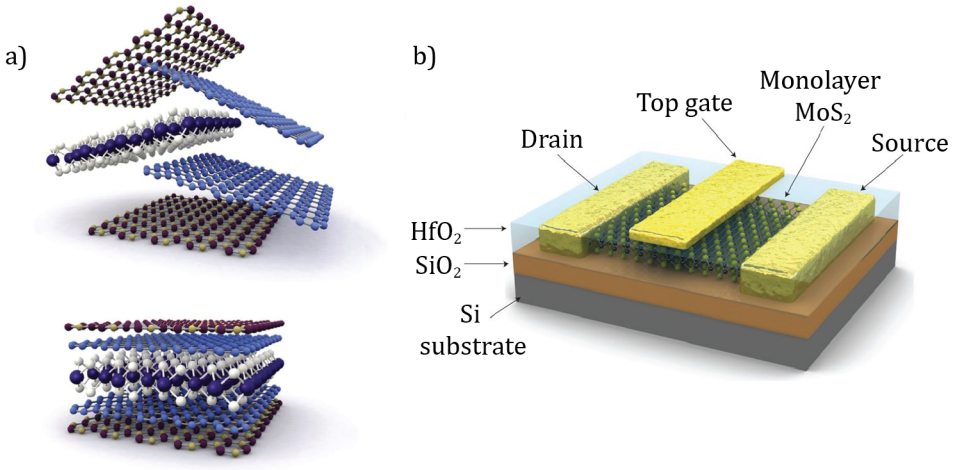

Figure 1.5: a) Schematic of stacking ML flakes into a single, multilayer structure. Adapted from [4]. b) Example of a functional MoS_2 transistor, fabricated by stacking flakes as desired. Adapted from [37].

1.3 Heterostructures

1.3.1 Layering TMDs

Research is now being aimed at stacking these 2D materials into HSs, in order to study fundamental physics and enable the engineering of electronic and optoelectronic devices [6]. In principle, fabricating these HS is a case of isolating each individual ML and then stacking them on top of one another, as illustrated in Fig. 1.5 a). A popular analogy for such fabrication, coined by Geim and Novoselov, is that of stacking with LEGO© blocks in order to build a structure [3]. In the case of van der Waals HSs, the strong covalent bonds provide the in-plane stability while weaker van der Waals interactions hold the stacks together.

By stacking flakes in this manner, sophisticated multilayer samples can be made with regularity. However, the quality of these HSs is limited by the purity of the initial MLs and the cleanliness of the transfer process.

To address flake quality, the majority of samples are made using the top down method of exfoliation of MLs from bulk, as bulk has fewer defects and is easier to synthesise in general [38]. This gives final flakes sizes of the order 10 µm [39].

In order to get larger flakes, attempts have been made to use bottom up approaches which directly grow the ML from its constituent elements, such as physical vapour deposition (PVD), chemical vapour deposition (CVD), molecular beam epitaxy [40] or beam lithography [41]. CVD can give exceptional control over size and material, under correct growth conditions. It is even possible to alternate conditions

during growth in order to make lateral HSs [42, 43]. However, the final specimens tend to have more defects and lower electrical performance than exfoliated samples [4, 39, 44].

A sharp atomic interface between layers is required in order to study interlayer effects within HSs. Efforts are made to clean the sample during production including the use of clean rooms and/or solvent cleaning followed by annealing [45, 46]. After fabrication, the samples are usually annealed again. During this anneal, the HSs exhibit a key self-cleaning mechanism by which the dirt between layers bind together to form bubbles of contamination, surrounded by an otherwise pristine, atomically-sharp interface [47]. This ensures that the final custom HSs are of sufficient quality and with high electronic performance.

As not all TMDs or 2D materials are stable in air, an increasing number of studies use graphene, or hBN, to encapsulate the sample and thus protect it from degradation in air [48]. HBN has also been shown to improve the electrical performance of the flakes when used to encapsulate it, for example in MoS_2 [49]. This allows a wider number of techniques to be used to analyse the more sensitive TMDs, such as $NbSe_2$ [50]. Graphene is also commonly used as an electrical contact for such HSs, which opens the door to studying the electronic properties of engineered van der Waals HSs and devices [51–53].

1.3.2 TMD devices and gating

Rational band structure engineering requires understanding of the layer dependent electronic structure of individual 2D materials and how they change when combined into multi-layer structures. It is possible to tailor the electronic structure of the stack such that the band alignments create functioning 2D devices.

Graphene is commonly used as a contact for 2D devices as it can be preferable over 3D metals [51, 54]. Metal contacts can cause charge redistribution within the MX_2, creating an interface dipole [55]. The deposition of the metal itself can cause damage to the ML, e.g. MoS_2, which then creates defect states within the bandgap causing Fermi level pinning to hinder the contact [56, 57].

Graphene, on the other hand, is van der Waals bonded to the ML so does not damage the ML or create defect states [55]. It also has remarkably high strength and carrier mobility [8, 60]. It is possible to fine-tune the work function of graphene easily with a back-gate, thanks to the linear dispersion relation at the **K** points discussed earlier. This creates the ability to tune the carrier concentration with precise control and a low resistance within graphene, shown in Fig. 1.6 a). Therefore, the Schottky barrier height between graphene and MX_2 shows large gate modulation, making it

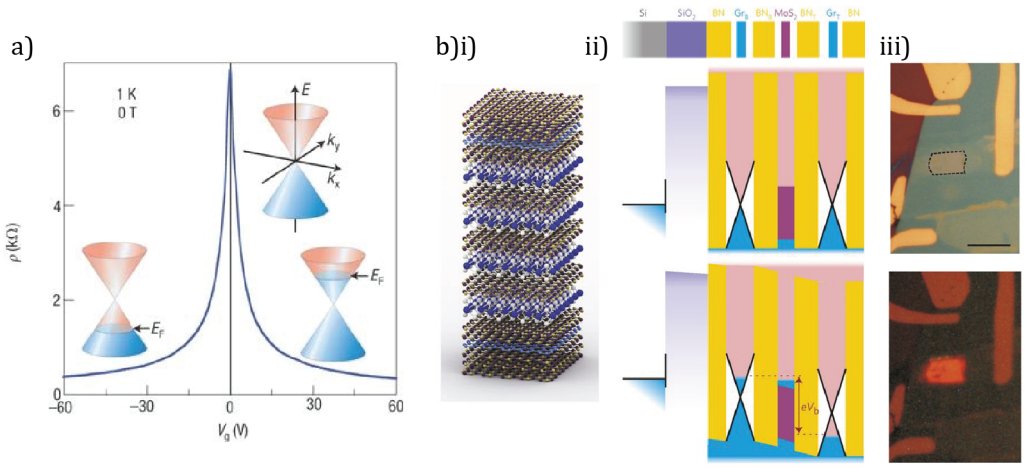

Figure 1.6: a) Schematic showing the electric field effect in graphene, with inserts showing the shift in work function with respect to gating. The rapid decrease in resistivity, ρ, indicates high carrier mobility. Adapted from [58]. b) Example of a functioning 2D LED, where i) shows the architecture of the sample, ii) shows the band alignment within the sample, with the shift in band under gating which allows the efficient charge injection required for the device to function as an LED, iii) shows an optical micrograph and electroluminescence micrograph of the device during operation. Adapted from [59].

an ideal contact [53, 61, 62].

It is possible to create electronic devices with graphene as the contact, ML or few layer TMDs as the semiconducting layer, and hBN as the gate dielectric, an example of which is shown in Fig. 1.5 b). To date, a wide number of devices have been fabricated and studied, including; capacitive devices, tunnelling devices, optoelectronic devices and photo detector, photovoltaic applications and LEDs [6, 37, 63–66].

A key example is by Withers *et al.*, of a functioning 2D LED shown in Fig. 1.6 b). Fig. 1.6 b) i) shows the architecture of a typical MoS_2 LED [59]. Fig. 1.6 b) ii) shows the band alignment within the device with zero gate voltage, and then with applied gate voltage. When enough gate bias is applied to the graphene there is electron injection from the back-gate and hole injection from the top gate into the MoS_2, which then causes radiative recombination within the MoS_2 layer. The ability of this LED to function is entirely dependent on the band alignment between layers and on being able to control carrier concentration within the graphene.

Other devices which rely on band alignment include excitonic devices, particularly ones which feature interlayer excitons. For example, stacks of WSe_2 on $MoSe_2$ (both direct bandgap semiconductors in their ML form [33]) have demonstrated electrically tuneable interlayer excitons where the hole and electron originate

from different layers, due to the type II band alignment between the layers [67].

As well as studying excitons, HSs allow us to probe a range of other fundamental physics such as; valley and spin physics [23, 68–70], interlayer hopping [50], and plasmonic devices [71, 72].

1.4 Measurement of electronic structure in 2D materials and heterostructures

All these applications depend on knowing and understanding how the devices operate under electrical load and how the individual materials respond to electrostatic gating, as well as combinations of layers. This requires the measurement of key band parameters such as band alignments, bandgaps, layer dependent band structures, as well as Schottky barrier heights and the role of any surface effects such as Fermi level pinning.

Plenty of studies have studied the electronic structure in 2D materials and HSs, with a wide range of techniques. ARPES is a surface science technique which can be used to measure band structure within the top few layers. Measuring the photoelectrons emitted from a surface, with both energy and angular resolution, gives information on the initial occupied electron states, the band structure, and the Fermi level of a sample. As this technique relies on photoemission, it is extremely surface sensitive and only probes the top few layers of a sample. This makes it ideal to study 2D materials and devices, though not useful for conventional semiconductor devices.

ARPES has been used extensively to study a wide range of layer dependent materials [73]. ARPES was successfully used to study the band structure of graphene in a study by Bostwick *et al.* which achieved high resolution band imaging of the full BZ of graphene on SiC, in order to study the many body interactions amongst the charge carriers [**Bostwick2006**]. Bilayer graphene has also been studied, showing the change in band structure and introduction of a bandgap with additional layers [74]. Both studies show the typical trigonal warping expected in graphene at the **K** points, as well as the linear dispersion of the Dirac cones.

ARPES has also been used to study a range of TMD samples. For bulk samples, various studies have focused on examining the valley and spin dependent properties of the **K** points, with high energy resolution, as well as mapping the surface band structure [75, 76]. Typically, these samples are cleaved from bulk crystals while in vacuum which reveals a pristine surface, without contamination from air, and enables these high resolution studies [75]. Other bulk materials beyond

the MoWSeS family have been successfully studied using ARPES, including Bi_2Se_3 [77], $ReSe_2$ [78], black phosphorous [79].

Both bulk and CVD grown samples have been studied across the range of the MoWSeS family [80–82]. However, the highest quality of ML is still achieved by exfoliation, which typically gives small flake sizes. The ARPES technique has classically been limited by the beam spot size, which therefore limits the minimum size of sample or domain which can be studied. However, additional focusing of the photon beam (described in Chapter 2) allows smaller samples to be studied. Micrometre sized spots are now achievable, meaning samples of atomically thin exfoliated flakes, typically of order $\sim$ 10 µm - 50 µm or less, and HSs can now be studied.

As such, micro angle-resolved photoemission spectroscopy (µ-ARPES) has been performed on small, exfoliated ML flakes and HSs in recent years. Jin *et al.* used ARPES to study the thickness dependent structure of MoS_2, in order to observe the band progression with additional layers [83]. Similar layer dependent studies have been performed on both WSe_2 [84] and InSe [85] as well as CVD grown samples [81]. ARPES enables the study of other fundamental physics, for example observing the charge density wave transition in $TiSe_2$ [86].

ARPES studies have also examined a range of 2D HSs. It can be used to study a range of electronic features, such as the formation of moiré bands within a twisted hBN/graphene HS, and can study interlayer hybridisation, for example in graphene/MoS_2 HSs [87] as well as $MoSe_2$/WSe_2 HSs [88].

ML and HS band alignments and interlayer effects can be studied using indirect methods. These methods also can enable measurements of carrier concentration dependent effects, by incorporating gating. Photoluminescence (PL) was the first technique to show experimental evidence of the transition from indirect to direct bandgap for MoS_2 by measuring an order of magnitude increase in signal for ML [89] and is still a dominant technique for studying the optical properties of 2D TMD materials [5, 27, 90]. PL peak positions give good agreement to expected excitonic energies, and are used to study the optical bandgap and response of MLs and HSs [67, 91–93].

The electronic bandgap and alignment can be probed using scanning tunnelling techniques such as scanning tunnelling microscopy (STM) and scanning tunnelling spectroscopy (STS). Graphene has been studied extensively with these techniques, to quantify its electronic properties [60]. There have also been STS and STM studies of graphene/TMD devices and HSs [94]. These studies have been able to probe the electronic bandgap of ML TMDs [92, 95–97]. Raman spectroscopy is

also regularly used to study the flake's physical and electronic qualities [41, 98–100].

These techniques combined, along with further transport measurements [101], can give good indirect insight into the band structure and alignments. However, the ability to directly measure the effects of doping on 2D materials and devices is desirable. ARPES gives direct mapping of the band structure and gives detailed information on the VB without inference. However, it only measures the filled states and as such the CB, and therefore bandgap, of semiconductors can not be measured without additional doping. Conventionally, doping in ARPES measurements is achieved by alkali metal deposition. This introduces excess electrons to dope the top layer of a material. Under enough n-type doping, the occupied electron states within a sample can be increased to the point where the conduction band becomes occupied and is visible on the measure photoemission spectra.

This method has been used to successfully dope and study a range of TMD materials and HSs including the full family of bulk MoWSeS materials [102], bulk $MoSe_2$ [68], epitaxially grown ML $MoSe_2$ [103] and quasi free-standing ML MoS_2 [104]. Alkali doping has also been used to study the tuneable spin splitting in WSe_2 [105] as well as the spin splitting and trion effects within WS_2 on hBN [106].

From these studies, researchers have been able to get estimates for band structure including bandgaps, band alignment and spin splitting. However, this technique has many limitations. The doping levels are hard to control or measure accurately, and it is only reversed by a high-temperature anneal which can potentially damage the sample. It also does not dope uniformly and can change the chemical nature of the sample in an unpredictable manner.

In order to get accurate measurement of carrier concentration and then observe how the bands behave as a function of carrier concentration, we want to incorporate electrostatic doping, with the back-gate geometry used in STS and PL measurements, into spatially resolved ARPES of MLs, similar to the kind seen recently in [107].

In this work, we show that this combination is possible and by using the same technique for fabricating these ARPES samples as for making functioning 2D devices, thus opens the path for using spatially resolved μ-ARPES to study the electronic structure of gated heterostructures during their operation. This work will show that such techniques give direct visualisation of the band structure within 2D van der Waals HSs and devices during operation. This helps give greater insight and understanding into how these types of samples behave under different electrical regimes and open a new platform for probing fundamental physics within ML materials and understanding 2D device design.

Chapter 2

Experimental methods

2.1 Angle-resolved photoemission spectroscopy

In this work, ARPES is used as the dominant technique employed for examining 2D HSs. This technique utilises the photoelectric effect to probe the in-plane electronic structure of a material near its surface, which is ideal for studying MLs and observing band hybridisation within HSs.

2.1.1 Photoemission theory

The photoelectric effect is the process by which an incoming photon of sufficient energy may excite and emit an electron from within a material. By measuring the final energy of the photoelectron, one may gain insight into its original states and subsequently the core levels and electronic bands within the material.

The photoelectric process is often described with a simple three-step model [108], shown in Fig. 2.1. The steps consist of:

1. The incoming photon excites an electron from within one of the filled energy levels such that it escapes the atom (i.e. the creation of a photoelectron),
2. The photoelectron travels to the surface,
3. The photoelectron escapes the surface of the material.

Also shown in the figure is the one-step model. In that model the photon absorption, electron removal, and electron detection are treated as a single process where the photoelectron is excited into a single damped surface state. This model is particularly complex and discussed in detail by Hüfner [108]. Despite the three-step model being purely phenomenological, it is sufficient to describe the process and will be discussed here.

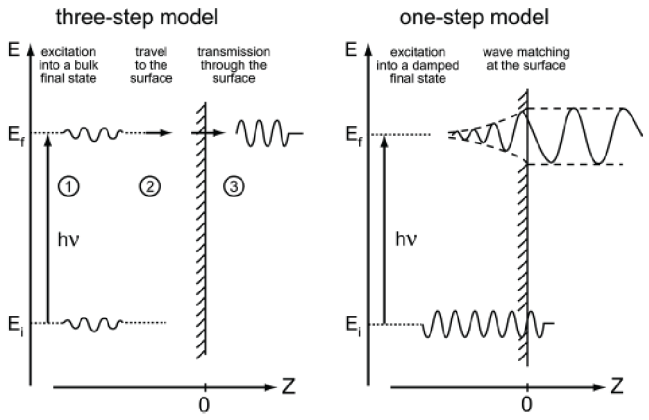

Figure 2.1: Three-step (left) and one-step (right) models of photoemission. The three-step shows creation, travel and transmission of the photoelectron. The one-step model shows the photoelectron excited directly into a damped final state. Figure from [108].

Step one

In the first step, the probability of a photoemission event occurring can be described using Fermi's golden rule. This describes the probability of a transition per unit time from an initial to a final state, w_{fi}, given by

$$w_{fi} = \frac{2\pi}{\hbar} |\langle \Psi_f^N | H_{\text{int}} | \Psi_i^N \rangle|^2 \delta(E_f^N - E_i^N - h\nu) \tag{2.1}$$

where Ψ_f^N and Ψ_i^N are the wave functions of the final and initial states, E_f^N and E_i^N are final and initial energies of an N-electron system. $h\nu$ is the energy of the photon beam and the perturbing interaction Hamiltonian, H_{int}, is given by:

$$H_{\text{int}} = -\frac{e}{2mc}(\mathbf{A}\cdot\mathbf{p} + \mathbf{p}\cdot\mathbf{A}) = -\frac{e}{mc}\mathbf{A}\cdot\mathbf{p}, \tag{2.2}$$

e is elementary charge, m is the electron mass, c is the speed of light, $\mathbf{A}$ is the vector potential and $\mathbf{p}$ is the momentum operator, $\mathbf{p} = \mathrm{i}\hbar\nabla$. The above equation is given by using commutation relations and approximating the final state as a dipole, i.e. a hole is created by the photoelectron leaving [108, 109].

By assuming the photoemission process is immediate under the sudden-approximation, i.e. there are no interaction between the post collision photoelectron and the remaining system, then the N-particle final state can be written as

$$\Psi_f^N = \mathcal{A}\phi_f^{\mathbf{k}}\Psi_f^{N-1} \tag{2.3}$$

where $\mathcal{A}$ is the asymmetry operator, $\phi_f^{\mathbf{k}}$ is the electron's final wave function and

Ψ_f^{N-1} is the final state wave function of the $(N-1)$-electron system. The initial state can similarly be written as

$$\Psi_i^N = \mathcal{A}\phi_i^{\mathbf{k}}\Psi_i^{N-1} \tag{2.4}$$

where $\phi_i^{\mathbf{k}}$ is the electron's initial wave function and Ψ_i^{N-1} is the initial state wave function of the $(N-1)$-electron system.

By combining Eqs. 2.1, 2.2, 2.3 and 2.4, the total photoemitted intensity for a given momentum, $\mathbf{k}$, and kinetic energy, E_{kin} is given as the sum over all final states

$$I(\mathbf{k}, E_{\text{kin}}) = \sum_{f,i} |M_{f,i}^{\mathbf{k}}|^2 \sum_m |c_{m,i}|^2 \delta\left(E_{\text{kin}} + E_m^{N-1} - E_i^N - h\nu\right) \tag{2.5}$$

where $M_{f,i}^{\mathbf{k}}$ is the matrix element and $\sum_m |c_{m,i}|^2$ is related to the spectral function, $A(\mathbf{k}, E)$, given by

$$A(\mathbf{k}, E) = \sum_m |c_{m,i}|^2 = |\langle \Psi_m^{N-1} | \Psi_i^{N-1} \rangle|^2. \tag{2.6}$$

The spectral function encapsulates the many body effects [108]. For a single particle, it can be written as

$$A(\mathbf{k}, \omega) = -\frac{1}{\pi} \frac{\Sigma''(\mathbf{k}, \omega)}{[\omega - \epsilon_{\mathbf{k}} - \Sigma'(\mathbf{k}, \omega)]^2 + [\Sigma''(\mathbf{k}, \omega)]^2} \tag{2.7}$$

where $\epsilon_{\mathbf{k}}$ is the band energy, $\Sigma(\mathbf{k}, \omega)$ is the self-energy of the system which captures the effect of interactions, $\Sigma'(\mathbf{k}, \omega)$ captures energy renormalisation and $\Sigma''(\mathbf{k}, \omega)$ captures lifetime broadening [109].

This ultimately lets us re-write the intensity for a 2D system as

$$I(\mathbf{k}, \omega) = I_0(\mathbf{k}, \nu, \mathbf{A}) f(\omega) A(\mathbf{k}, \omega) \tag{2.8}$$

where $I_0(\mathbf{k}, \nu, \mathbf{A})$ is proportional to $|M(\mathbf{k}, \omega)|^2$, $M(\mathbf{k}, \omega)$ is again the matrix element, and $f(\omega)$ is the Fermi function which describes the occupation probability as a function of temperature and chemical potential, μ, given by

$$f(E) = \frac{1}{e^{(E-\mu)/k_{\text{B}}T} + 1}. \tag{2.9}$$

The matrix element is dependent on the incident photon energy and modulates intrinsic intensities according to experimental geometries.

The matrix element captures the description of the variation in intensity across a band for ARPES experiments, i.e. the spectral weight of the bands. This encapsulates experimental handedness, polarisation effects and dichroism [110]. It also shows that both beam energy and polarisation ultimately effect the photoemission cross section [38, 111].

One of the implications of the matrix element for ML MX_2 materials is that they are more intense at $\mathbf{\Gamma}$ than at $\mathbf{K}$, though this also depends on the interaction cross section which varies with beam energy. Also, depending on polarisation, due to the valley polarisation then either $\mathbf{K}$ and $\mathbf{K'}$ is more intense which can effect measurements.

For graphene, the matrix element encapsulates the fact that bands are more intense within the first BZ. Practically this means that if we measure an energy-momentum slice through a Dirac point into the second BZ then one side of the cone will be considerably fainter [110]. This asymmetry in the Dirac cone, known as the dark corridor, is also a result of interference between photoelectrons from the A and B sub-lattices [112] and is observed multiple times throughout this thesis.

Step two

The second step of the three-step model describes the photoelectron propagating to the surface. When electrons travel within a solid, they can undergo inelastic scattering and lose energy. A photoelectron created with energy E_{kin} at depth z beneath the surface has a given probability of reaching the surface before being inelastically scattered [111]. The probability decreases exponentially away from the surface at a length scale of λ, given by

$$I(z) = I_0 e^{(-z/\lambda)} \tag{2.10}$$

[113] where I_0 is the initial intensity of electrons, z is the distance travelled from creation and λ is inelastic mean free path (IMFP). When λ is large, the greater the likelihood of the photoelectron will travel further before being inelastically scattered, and the higher the likelihood that the photoelectron will reach the surface. Therefore, a high λ indicates a larger sampling depth into a solid. Fig. 2.2 shows λ against kinetic energy, known as the universal curve, which is roughly the same for all materials.

The approximate form of λ in Å can be estimated empirically through testing multiple elements [108, 113]. At low energies, λ goes roughly as E^{-2} which can be explained by considering that fewer states are available at lower energy. At high

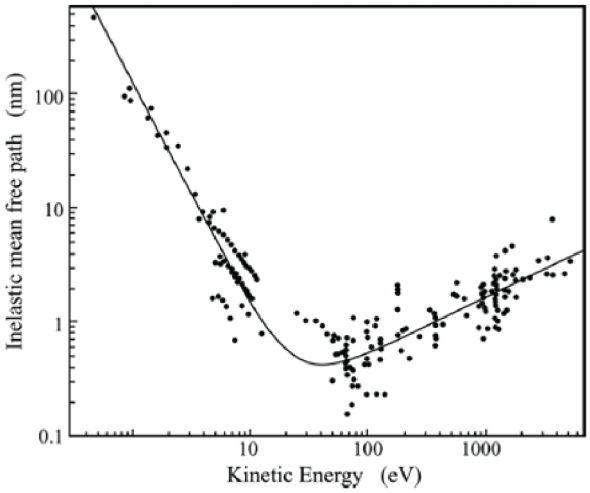

Figure 2.2: Universal curve for the inelastic mean free path of electrons with different kinetic energies within a material. Figure from [113].

energies, λ increases which can be explained by considering that the electrons have more kinetic energy to travel further before scattering. So, at either high or low energies, the sampling depth into the material is high and the photoelectrons are from a large proportion of the material near the surface.

There is a minimum in λ at roughly 50 eV, where electrons of that energy must have travelled from within the top $\sim$ 10 Å of the surface. This means the sampling depth is only the top few layers making it extremely surface sensitive. For our studies the photon beams, and therefore photoelectrons, are of order $20 - 100$ eV. Therefore, we only probe the top few layers of a sample, which is very advantageous for surface studies. This, along with the fact they are easy to focus and detect, make electrons ideal for studying 2D samples and HSs.

Step three

In the third step of the three-step model, the photoelectrons must escape the surface. This is dependent on them having sufficient kinetic energy. From energy conservation considerations, the kinetic energy, E_{kin}, of the measured photoelectron is given by

$$E_{\text{kin}} = h\nu - E_{\text{B}} - \Phi, \tag{2.11}$$

where $h\nu$ is the energy of the incident photon, E_{B} is the original binding energy of the electron and Φ is the work function of the system, which encapsulates the work function of both the sample and analyser [109, 114]. By measuring the kinetic energy

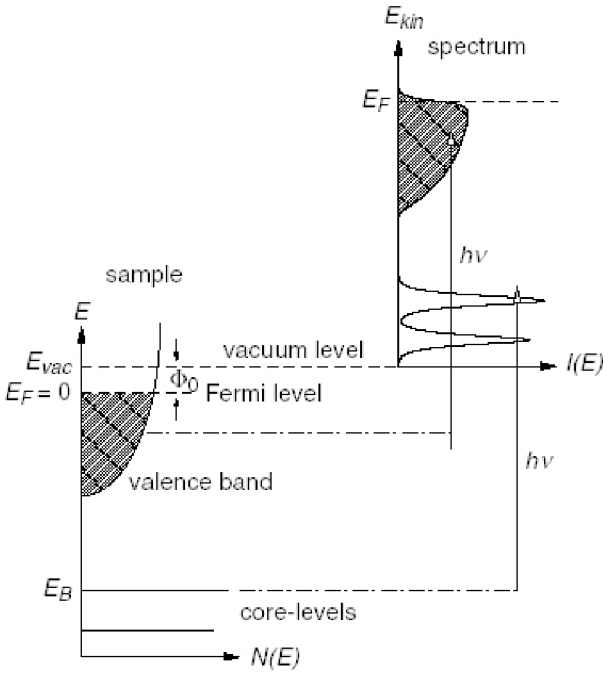

Figure 2.3: Schematic for the kinetic energy of emitted photoelectrons from an incident photon energy of $h\nu$ from within a material, with respect to vacuum level, E_{vac}. Figure adapted from [108].

of the emitted photoelectrons, one can determine the binding energy of the state they came from. Fig. 2.3 shows the final measured spectrum for photoelectrons excited by a photon of energy $h\nu$, with kinetic energy measured relative to vacuum level. In practise the energy for solids is quoted as binding energy, given by $E_{\text{B}} = E_{\text{kin}} - E_{\text{F}}$.

2.1.2 Angular resolution

Fig. 2.4 shows the typical sample geometry for photoemission. The incoming photon beam excites photoelectrons, which exit the sample at an angle of θ, measured from the z-direction, and ϕ, measured from the x-direction. By measuring the emission angle of the photoelectrons along with the final electron's kinetic energy, one can map the electronic bands within the sample. This is possible because the wavevector parallel to the surface, $\mathbf{k}_{||}$, is conserved during photoemission. The perpendicular wavevector, however, is not conserved, complicating 3D measurements. For the case of 2D materials, this is not an issue and one may ignore the perpendicular k_z component [114]. From energy and momentum conservation considerations, it is possible to write the final parallel momentum of the photoelectron, $\mathbf{k}_{||}$, as [108,

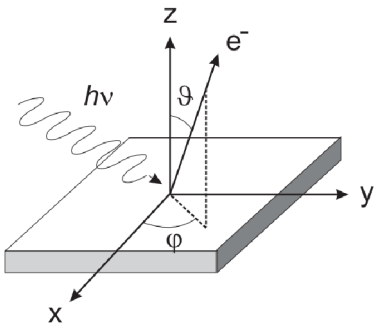

Figure 2.4: Schematic of the incoming photon, $h\nu$, and outgoing photoelectron, e^-, during photoemission. θ is measured from the surface normal and ϕ from the x-direction.

115]:

$$\mathbf{k}_{||} = \sin(\theta)|\mathbf{k}| = \sin(\theta)\frac{\sqrt{2m_e E_{\text{kin}}}}{\hbar} \tag{2.12}$$

where θ is the polar emission angle, m_e is the rest mass of an electron and $\hbar$ is the reduced Plank's constant. By combining Eq. 2.12 with the kinetic energy given in Eq. 2.11, an image of the initial, filled band structure is created.

In order to measure different emission angles the sample, or detector, may be physically rotated in θ and/or ϕ accordingly. The emitted electrons are measured using a hemispherical analyser, with a 2D detector, shown schematically in Fig. 2.5. The analyser consists of two hemispherical plates held at different potentials. The electrons enter through a series of focusing lenses into the hemisphere where only electrons of a desired energy range may pass through the exit slit. The desired energy range is centred on E_P, where the full range is $E_P \pm \Delta E$, and is controlled during experiment by setting the pass energy of the analyser and helps determine energy resolution [114]. The electrons are then detected by the 2D detector, typically a 2D channel plate with a phosphorous screen imaged using a CCD camera, which allows energy resolution along its length as shown in Fig. 2.5 (a).

Fig. 2.5 (b), shows the flight of electrons within a hemispherical analyser for angular resolution. As they travel, electrons emitted with slightly different angles have different flight paths. These electrons are detected by the 2D detector within an angular range of $\pm\beta$. These angles can then be transformed back to wavevector using a process known as k-warping which takes angular data (which is non-linear in momentum) and interpolates it into a new grid which is linear in momentum, using Eq. 2.12. By this process, direct mapping of the electronic bands with energy and momenta parallel to the surface can be achieved.

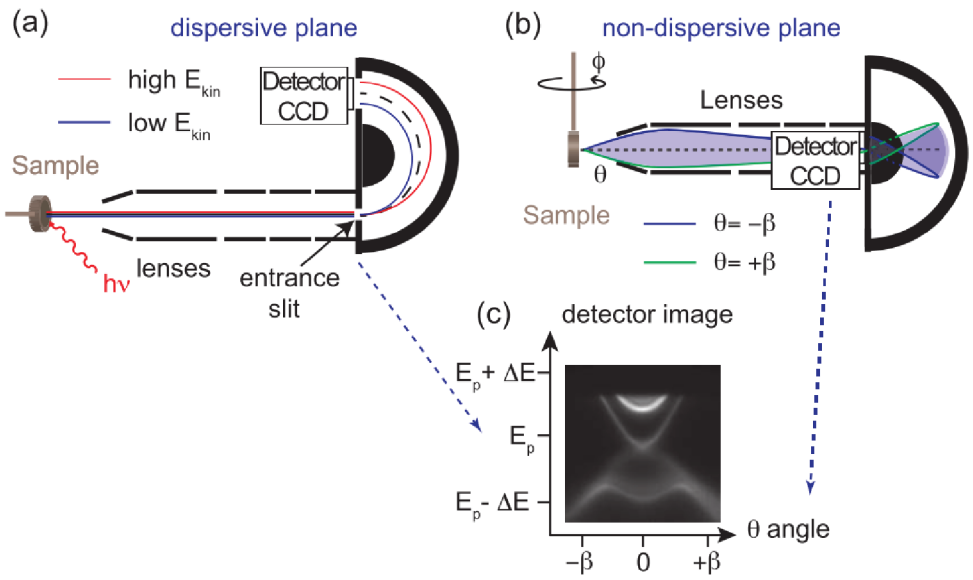

Figure 2.5: Schematic of the sample and detectors commonly used for ARPES measurement. Figure adapted from [114].

2.2 Synchrotron radiation

2.2.1 Generation

ARPES experiments require an incoming photon beam within an ultra-high vacuum (UHV) system. While laboratory X-ray and laser sources are often used for X-ray photoemission spectroscopy (XPS) and very high resolution ARPES measurements, in order to get the high resolution required for band mapping and to achieve greater spatial resolution, synchrotron sources are usually required. This is because a large proportion of photons are lost during focusing, so an intense original source is required to illuminate the final sample with sufficient photons [114].

Synchrotron radiation is generated when highly relativistic charged particles are accelerated radially, emitting a beam of photons perpendicular to the acceleration. A synchrotron is a type of particle accelerator, which typically begins with a linac used to accelerate electrons (or other charged particles) into a closed loop storage ring. The main ring is used to accelerate the electrons to speed, then keep them on course using focusing and bending magnets. Radiation is produced by the bending magnets as well as insertion devices known as wigglers and undulators. These devices are made up of a series of magnets which are designed to oscillate the electron beam along its path in order to create radial acceleration. The multiple

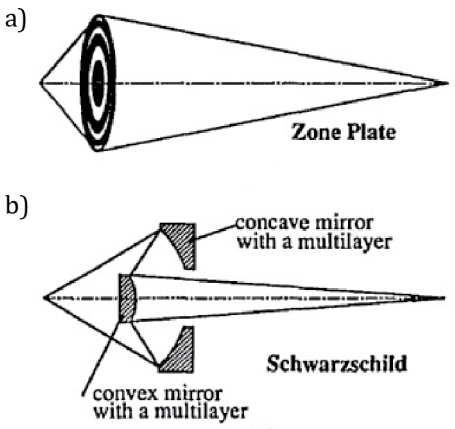

Figure 2.6: Schematic of a) zone plate and b) Schwarzschild objective optics, used for focusing a photon beam to the spot size required for spatially-resolved ARPES. Figure adapted from [116].

bends increase synchrotron emission and increase the spectral brilliance of the final emitted photon beam [111].

The final, intense beam is then passed to an analysis end-station through a series of gratings and monochromators. Depending on beamline design, the spacing of the monochromators and gratings can be varied to dictate the energy of the final beam received into the analysis chamber. Focusing mirrors are used to keep the beam on track and create a typical ARPES spot size of $\sim$ (10 - 100)^2 µm^2.

Regular ARPES with spots of this size can be used to study large structures such as bulk crystals, where the relatively large spot size is not an issue. However, such a spot size is not appropriate for small structures, such as samples with smaller crystal domains. For example, exfoliated TMD flakes are typically $\lesssim$ 10 µm, with areas of interest in HSs as small as 1 or 2 µm. As such, additional focusing of the beam is required to achieve greater spatial resolution.

2.2.2 Spatial resolution

In order to achieve greater spatial resolution, the beam is focused to a spot size of roughly 500 nm - 1 µm. This is currently achieved with two types of optics systems: a zone plate or a Schwarzschild objective.

A zone plate is a circular diffraction grating which gets combined with an order sorting aperture (OSA) to filter out higher order diffractions, shown in Fig. 2.6 a). A zone plate system can achieve a focused ARPES spot size of $\sim$ 400 nm [117]. A single zone plate can be used for a range of wavelengths and beam energies by exploiting different focal lengths. However, they experience a significant loss of

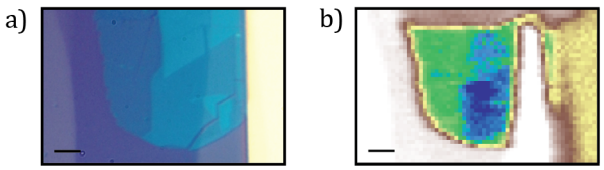

Figure 2.7: a) Optical micrograph and b) SPEM map of a WS_2 sample, showing the spatial resolution achievable. Scale bar 5 µm.

brilliance.

A Schwarzschild objective consists of two concentric, spherical mirrors separated by the focal length of the system, shown in Fig. 2.6 b). An incoming beam can be focused to a final spot size of $\sim 600\,\text{nm}$ [118]. The benefit of this system is that it loses less brilliance than other schemes. However, each objective is optimized for a single beam energy only therefore there is no beam energy tuneability unless the objectives are swapped.

Once the beam is focused to a sufficiently small spot size, this allows for spatially-resolved ARPES. A sample can be mapped using scanning photoemission microscopy (SPEM), where each pixel relates to the photoemission intensity at that point. The analyser is set to measure a specific energy and angular range, then the beam spot is moved across the sample in the x- and y-direction. Each pixel is given by the integrated intensity across both energy and angle of the 2D detector. The intensity will change depending on the material, as different materials will have different bands within the energy and angular range of the detector.

SPEM mapping allows a very effective mapping technique and can be used to identify different flakes. Fig. 2.7 shows a) an optical micrograph and b) a SPEM map of the same area of a WSe_2 sample to illustrate how features can be matched. This allows the relevant area to be identified and studied with sub-micron precision. Other uses for SPEM mapping will be discussed in Chapter 6.

2.2.3 SPECTROMICROSCOPY, Elettra

The spatially-resolved endstation, SPECTROMICROSCOPY, at Elettra Sincrotrone Trieste uses a Schwarzschild objective to achieve a final spot size of 600 nm, with two possible beam energies: 27 eV and 74 eV. Fig. 2.8 a) shows the path of the beam through focusing mirrors and monochromators to the Schwarzschild objective and analyser chamber.

The electron analyser used is a custom-built in-house version of a hemispherical analyser. The analyser is considerably smaller than standard, with an

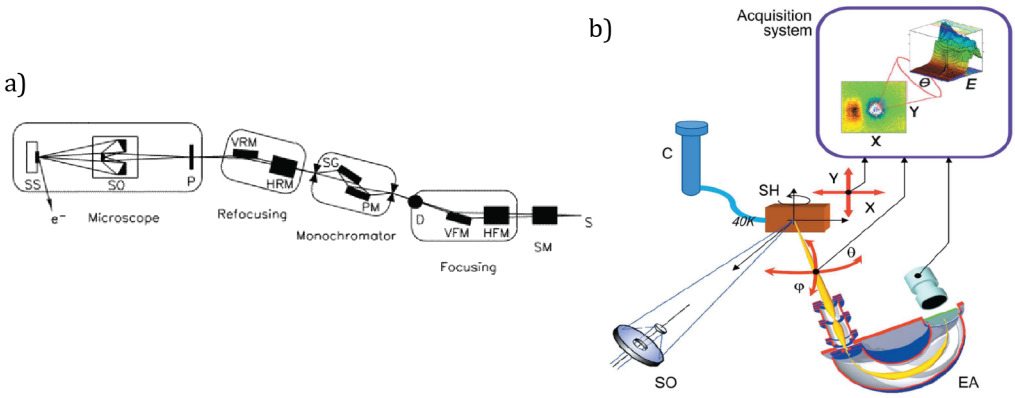

Figure 2.8: Schematic of the endstation at SPECTROMICROSCOPY, Elettra. a) shows the focusing and beam alignment from the ring to the analysis chamber. b) shows the geometry within the analysis chamber, including Schwarzschild objective (SO), sample holder (SH), cryostat (C) and electron analyser (EA). Figure adapted from [118, 119].

outer radius of only 60 mm verses 200 mm for a standard Scienta R4000 hemispherical analyser. The analyser is small because it is moved around within the vacuum chamber, whereas most ARPES analysers are attached externally.

Fig. 2.8 b) shows the geometry of the sample and analyser at SPECTROMICROSCOPY, and shows how the sample can be moved in the x- and y- direction to form a SPEM map. The sample can be tilted in the polar axis, around the z-direction, and is usually rotated to 45° with respect to the incident photon beam during measurements. The sample holder is attached to a cryostat and the sample was cooled to $\sim 100\,\mathrm{K}$ for the measurements reported here.

The majority of the angular control is given by moving the analyser itself. It can be tilted on its own angular system, P and T, which are shown in Fig. 2.9 a). The range for P goes from 90°, where measured photoelectrons have been emitted perpendicularly, or normal, to the surface, to 0°. The range for T goes from 0°, where photoemission is normal to the surface, to 60°. The full range of safe angles available are shown in Fig. 2.9 d), $P = 92$ to 45° and $T = -2$ to 50°, which is less than the full range of the motors due to the geometry within the chamber.

These angles are not the same as θ and ϕ defined in Fig. 2.4. In order to k-warp from P, T into $\mathbf{k}_{||}$, the follow relations are used

$$k_x = \frac{1}{\hbar}\sqrt{2m_e E_{\mathrm{kin}}}\left(\cos(P - P_{\mathbf{\Gamma}})\cos(\nu)\sin(T - T_{\mathbf{\Gamma}}) + \cos(T - T_{\mathbf{\Gamma}})\sin(\nu)\right) \quad (2.13)$$

$$k_y = \frac{1}{\hbar}\sqrt{2m_e E_{\mathrm{kin}}}\left(\cos(\nu)\sin(P - P_{\mathbf{\Gamma}})\right) \quad (2.14)$$

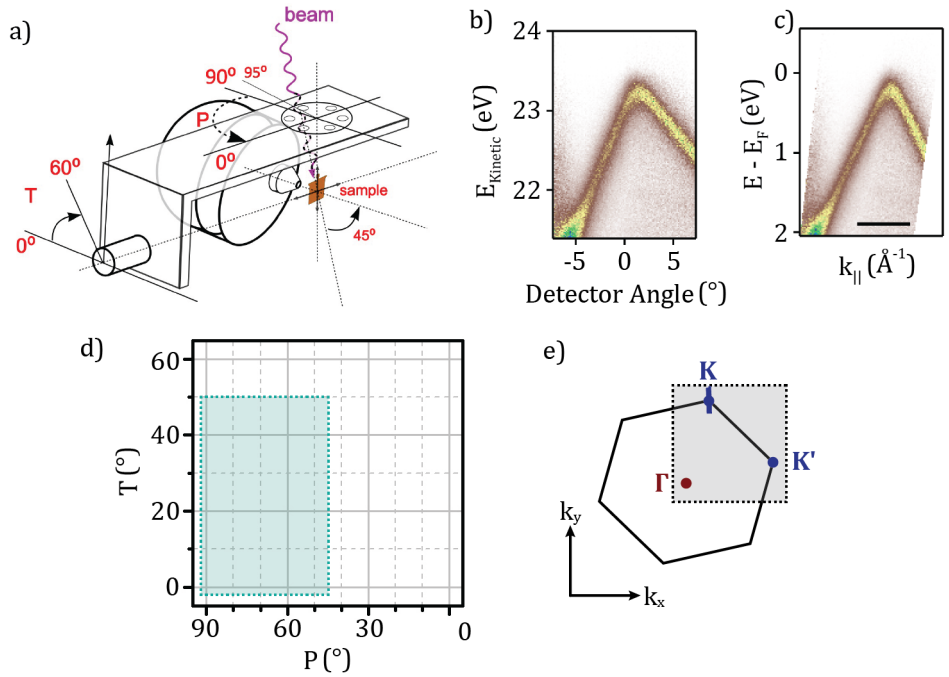

Figure 2.9: a) Schematic of sample and analyser geometry at SPECTROMICROSCOPY. Analyser can be rotated in P and T, with the sample held at 45° to incoming photon beam. This measures an emitted photoelectron normal to the surface when $P = 90°$, $T = 0°$. Figure adapted from [120]. b) Energy-angle slice taken from the detector, through a graphene Dirac cone, measured with a beam energy of 27 eV. c) Energy-momentum slice of the same data, which has been k-warped to momentum space. d) Graph showing available P and T angles for the detector shown by the shaded blue region, limited by the space accessible within the UHV analysis chamber. e) First BZ of graphene, with the shaded region showing the momentum space accessible with the detector. The orientation of the BZ matches that of the data shown in b) and c), with the blue line through **K** to show the direction of the slice.

where P, T are the angles of the slice and $P_{\mathbf{\Gamma}}$, $T_{\mathbf{\Gamma}}$ are the angles of **Γ** for the sample.

In order to image the bands, a single energy-angle slice is taken from the analyser, an example for a graphene **K** point is shown in Fig. 2.9 b). This is then k-warped into an energy-momentum slice using the above relations, with an example of the conversion shown in Fig. 2.9 c).

Fig. 2.9 e) shows the BZ of graphene in reciprocal space, and the blue line shows the position of the energy-momentum slice shown in Fig. 2.9 b) and c). In order to map out a region in k-space to image the full **Γ** - **K** dispersion, multiple energy-momentum slices are taken while changing the angles in between slices. These are stitched together to form a 3D dataset, then a **Γ** - **K** profile is extracted. The grey shaded box shows the region in k-space accessible for the detector at a beam energy of 27 eV.

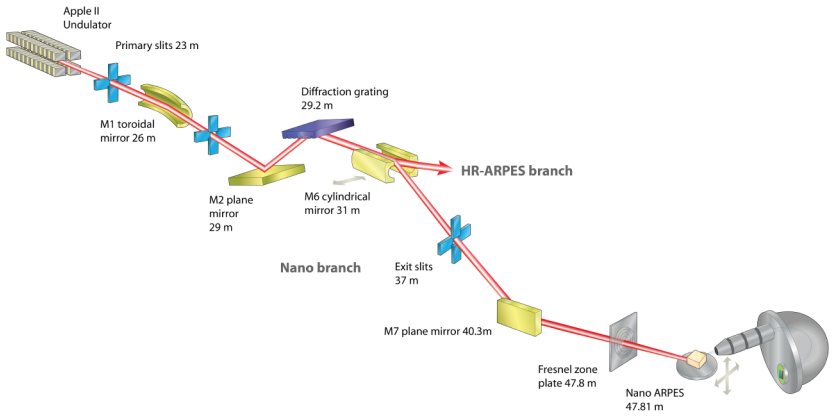

Figure 2.10: Schematic of the spatially-resolved ARPES endstation at I05, Diamond. The beam is focused through mirrors and monochromators, through a zone plate and OSA to the sample and into the hemispherical electron analyser. Figure adapted from [121].

The final system has spatial resolution of 600 nm, energy resolution of ∼30 meV and angular resolution equivalent to 0.03 Å^{-1} [118].

2.2.4 I05, Diamond

The spatially-resolved ARPES endstation, I05, at Diamond Light Source uses a zone plate and OSA optics to achieve a spot size of 400 nm, shown in Fig. 2.10. The zone plate system can be used for a range of beam energies, from 50 eV to 90 eV.

The sample stage can be moved in x-, y-, z-, polar and azimuthal directions. A Scienta R4000 hemispherical analyser is attached externally to the analysis chamber and can be rotated in the polar angle around the chamber. The accessible region in k-space is therefore a band across the BZ. The analyser also has a deflection mode, which allows a larger area of k-space to be imaged by changing the acceleration voltages of the analyser [122].

The final system has energy resolution of $\sim 30 - 50$ meV and angular resolution of 0.2° [117, 123].

2.2.5 ANTARES, Soleil

The spatially-resolved endstation, ANTARES, at Soleil Light Source uses a zone plate and OSA optics, shown in Fig. 2.11.

The sample can be moved in x-, y-, z-, polar and azimuthal directions. It uses a fixed Scienta R4000 analyser. In order to map in k-space, the sample is rotated

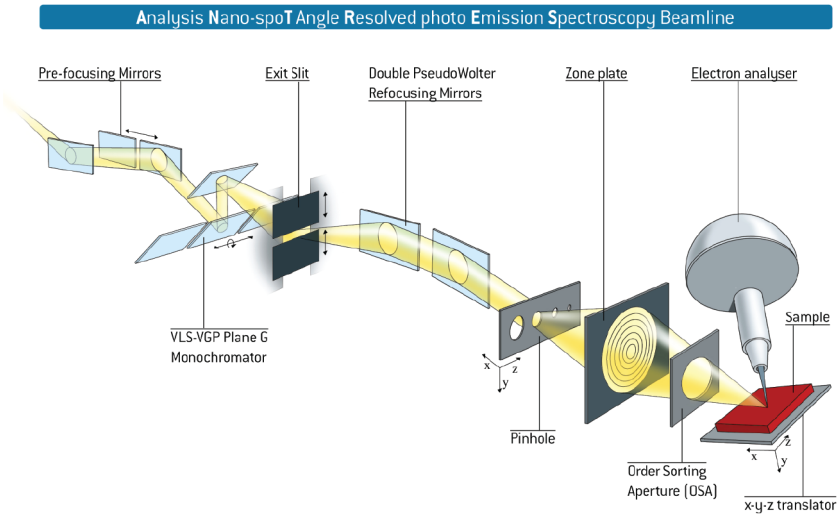

Figure 2.11: Schematic of spatially-resolved ARPES endstation at Antares, Soleil. The beam is sent through focusing mirrors, through a zone plate and OSA to the sample and electron analyser. Figure adapted from [124].

azimuthally. Therefore, the accessible region in k-space is a radial band around the BZ.

The final system has spatial resolution of $\sim$ 500 nm, energy resolution of $\sim$30 meV and angular resolution of 0.2° [124].

2.3 Atomic force microscopy

Atomic force microscopy (AFM) is a scanning probe microscopy (SPM) technique which relies on attractive and repulsive forces in order to "feel" a surface. A simplified schematic of AFM operation is shown in 2.12 a). A tip is mounted on the end of a cantilever, controlled using an x-, y-, z- piezoelectric. As the tip approaches the surface of a sample, forces between the tip and the surface cause the cantilever to bend. The amount that the cantilever is deflected is measured by reflecting a laser off the top of the cantilever into a four-quadrant photodiode. The deflection is a measure of the local forces experienced by the tip and can be used to map the topography of a surface.

Two techniques are commonly used for mapping a sample with AFM: contact mode and tapping mode. In contact mode, the tip is pressed into the surface which causes the cantilever to deflect due to repulsive van der Waals forces. As the tip is scanned over a surface, the amount of deflection is kept constant by moving the

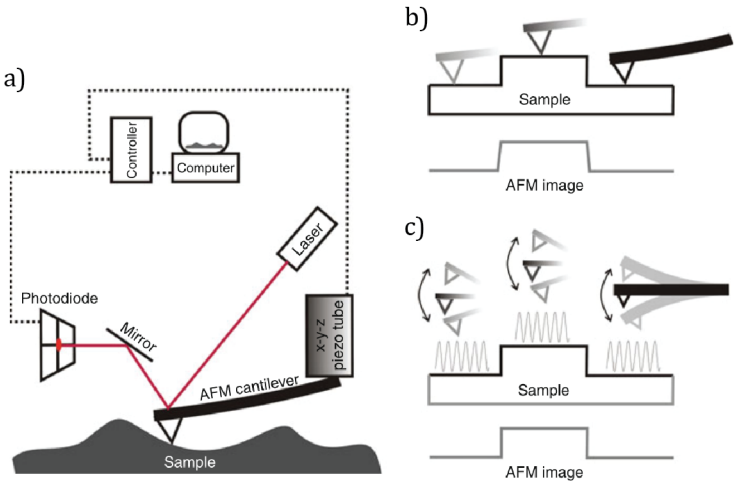

Figure 2.12: a) Schematic of an atomic force microscope. The tip is moved across the surface, with a laser reflected into a photodiode to track deflection. b) Showing contact mode passing over a feature on the surface, maintaining tip deflection by raising/lowering the tip. c) Showing tapping, or AC, mode where the tip is oscillated and the amplitude of oscillation is maintained over a feature by raising/lowering the tip. Figure adapted from [126].

cantilever up and down in z using the piezoelectric, i.e. the height above the surface. A topographic map is then given by recording the z-height, illustrated in Fig. 2.12 b). As the tip is in physical contact with the surface, this technique can easily damage or change the sample during imaging [125].

In tapping, or AC, mode, the tip is not brought into direct contact with the sample but rather it is oscillated above the surface. As the tip approaches the surface, the amplitude of oscillation is reduced due to tip-surface forces. The amplitude is then kept constant by using a feedback loop to control the height of the cantilever stage in z. As with contact mode, a topographic map is given by recording the change in height, shown in Fig. 2.12 c). As the surface only experiences minor lateral forces in tapping mode, it is much less destructive than contact mode and is used more often for topography imaging [126].

The motion of the tip and cantilever in tapping mode can be described by modelling it as a mass on a spring, or rather as a sinusoidally driven, damped harmonic oscillator of effective mass, m. The equation of motion for such a system is given by

$$\ddot{z} + \beta\dot{z} + \omega_0^2 z = A_{\text{drive}} \cos(\omega t) \tag{2.15}$$

where ω_0 is the natural frequency of the cantilever, given by

$$\omega_0 = \sqrt{\frac{k}{m}}, \tag{2.16}$$

A_{drive} is the amplitude of driven oscillation on the cantilever and k is the spring constant of the cantilever. β is related to the damping term, given by

$$\beta = \frac{1}{Q\omega_0} \tag{2.17}$$

where Q is the quality factor of the cantilever. The steady-state solution for the equation of motion in Eq. 2.15 has the form

$$z(t) = A_{\text{cant}} \cos(\omega t - \psi) \tag{2.18}$$

where A_{cant} is the amplitude of oscillation of the cantilever given by

$$A_{\text{cant}} = \frac{A_{\text{drive}}}{\sqrt{\left(\omega_0^2 - \omega^2\right)^2 + \omega^2\beta^2}} \tag{2.19}$$

and ψ is the phase response of the cantilever given by

$$\psi = \arctan\left(\frac{\omega\beta}{\omega_0^2 - \omega^2}\right). \tag{2.20}$$

The resonance frequency of the oscillator, ω_{res}, is defined as the driving frequency at which A_{cant} is maximised. For small damping that is equal to the natural frequency i.e. $\omega_{\text{res}} = \omega_0$.

By substituting in Eq. 2.17, these become

$$A_{\text{cant}} = \frac{A_{\text{drive}}}{\sqrt{\left(1 - (\omega/\omega_0)^2\right)^2 + \omega^2/\left(Q\omega_0^2\right)}} \tag{2.21}$$

and ψ is the phase response of the cantilever given by

$$\psi = \arctan\left(\frac{\omega}{Q\omega_0\left(1 - \omega^2/\omega_0^2\right)}\right). \tag{2.22}$$

The phase response is defined as the phase lag of the cantilever behind the

driving force phase, ϕ, and is given by

$$\phi = \psi - \frac{\pi}{2} \tag{2.23}$$

Therefore, at resonance $\psi = \pi/2$. Combining Eqs. 2.22 and 2.23 gives

$$\phi = \arctan\left(\frac{Q\omega_0\left(1-\omega^2/\omega_0^2\right)}{\omega}\right). \tag{2.24}$$

Considering a small shift in frequency about the resonant frequency, i.e. $\omega \mapsto \omega_0 + \Delta\omega$, gives

$$\phi\left(\Delta\omega\right) = \arctan\left(\frac{Q\omega_0\left(1-\left(\omega_0+\Delta\omega\right)^2/\omega_0^2\right)}{\left(\omega_0+\Delta\omega\right)}\right). \tag{2.25}$$

Expanding with a Laurent expansion to the first order gives

$$\phi\left(\Delta\omega\right) = \arctan\left(-2Q\frac{\Delta\omega}{\omega_0}\right). \tag{2.26}$$

Expanding the function further using $\arctan\left(x\right) = x - \frac{x^3}{3} + ...$, valid for small ϕ, and noting that in tapping mode, the driving frequency is fixed thus ω_0 is varied, not ω, gives that

$$\Delta\phi\left(\Delta\omega_0\right) = 2Q\frac{\Delta\omega_0}{\omega_0} \tag{2.27}$$

which is valid for $\Delta\omega_0 \ll \omega_0$. The same holds for small changes in the phase response, therefore

$$\Delta\psi\left(\Delta\omega_0\right) = 2Q\frac{\Delta\omega_0}{\omega_0}. \tag{2.28}$$

From this equation, we note that a change in frequency gives a change in phase response.

Now consider that in tapping mode the driving force usually cancels the damping which, combined with Eq. 2.16, gives an equation of motion of

$$m\ddot{z} + kz = 0. \tag{2.29}$$

Adding in a weak perturbing potential from tip-sample interactions, F, gives

$$m\ddot{z} + kz - F = 0. \tag{2.30}$$

By performing a linear expansion of the force we can obtain that a frequency shift

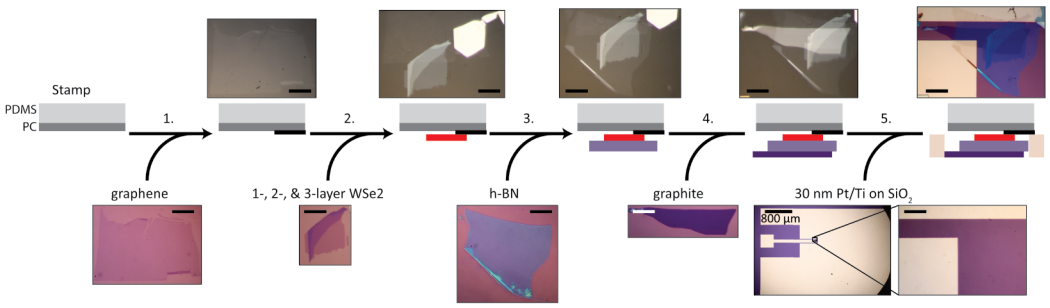

Figure 2.13: Schematic of sample fabrication using exfoliation and dry transfer. The stamp, consisting of polycarbonate (PC) on polydimethylsiloxane (PDMS), is used to pick up each flake and then place and release the heterostructure stack onto the SiO_2 substrate, bridging the two Pi/Ti electrodes.

is proportional to the force gradient such that [125]

$$\frac{\Delta\omega}{\omega} = -\frac{1}{2k}\frac{\partial F}{\partial z}. \tag{2.31}$$

This gives that

$$\Delta\omega_0 = -\frac{\omega_0}{2k}\frac{\partial F}{\partial z} \tag{2.32}$$

which shows that a change in frequency is related to the force gradient. Combining Eqs. 2.28 and 2.32 also gives that

$$\Delta\psi = -\frac{Q}{k}\frac{\partial F}{\partial z} \tag{2.33}$$

i.e. a change in phase is also related to the force gradient, or in summary $\Delta\psi \propto \Delta\omega \propto \frac{\partial f}{\partial z}$. These relations will be used later in Chapter 6, but for now it means tapping mode AFM can be used to map the topography of a surface.

2.4 Sample preparation

2.4.1 Fabrication

The MX_2 samples and gated HSs were fabricated by collaborators from the Cobden Group at the University of Washington, using the technique previously reported [88, 127]. A summary of the method will be given here.

Fig. 2.13 shows the dry transfer technique for fabricating van der Waals HSs [46]. The sample shown in this figure is the same sample as shown in Fig. 4.5. The final sample is graphene on top of 1, 2 and 3-layer WSe_2 on multilayer hBN on graphite, all on a SiO_2 substrate i.e. gr/WSe_2/hBN/graphite/SiO_2.

Fig. 2.13 *step 1.* shows the graphene pick-up. Graphene was mechanically exfoliated from graphite using the Scotch-tape method, at 100 °C onto SiO_2 which had immediately previously been oxygen plasma treated at 50 W for 5 min. The graphene flake was picked up onto a polycarbonate (PC) coated polydimethylsiloxane (PDMS) stamp, mounted onto the end of a glass slide. The slide was connected to a motorized micro-manipulator to give fine control of the pick-ups. The stamp was brought into initial contact with the graphene at 130 °C. The substrate was then heated to 150 °C to give a good pick-up and prevent delamination of the PC from PDMS. The system was then cooled to 70 °C to begin detaching the graphene. The stamp with graphene flake was moved upwards, away from the SiO_2 substrate, at a speed of $\sim 1\,\mu m s^{-1}$.

Fig. 2.13 *step 2.* shows the WSe_2 flake pick-up. WSe_2 was exfoliated onto another plasma cleaned SiO_2 substrate, this time carefully heating the sample to 120 °C, then cooling down to room temperate before slowly removing the Scotch tape. The flake was identified using optical contrast, then aligned to the graphene on the stamp. The same press down and release described in step 1 was used to pick up the WSe_2 flake onto the graphene stamp.

Fig. 2.13 *step 3. and 4.* show the hBN and graphite flake pick-up, respectively. As with the graphene, the hBN has been exfoliated onto SiO_2 at 100 °C and topographic AFM was used to check the thickness of the flake. The same alignment, press down and release technique was then used to pick up the hBN onto the stamp. The same process was performed for graphite.

Fig. 2.13 *step 5.* shows the stick down of the HS onto the final substrate. The final substrates have two 30 nm thick Pt/Ti electrodes, on a SiO_2 chip. The electrodes were prepared by e-beam lithography and cleaned by annealing in an Argon/Hydrogen 95 %/5 % atmosphere at 400 °C. The sample was placed across the bridge of these two electrodes such that the small electrode contacts the graphite back-gate and the bigger electrode contacts the graphene. The large electrode is connected to ground during measurements and covers most of the sample in order to minimise electrostatic distortion of the photoelectron spectrum, when gating is applied. The system was then heated to 175 °C which is the point at which the PC detached from the PDMS, and the stamp was raised and removed. This leaves the heterostructure and PC on the substrate. The remaining PC was then removed by repeated rinsing in alternating chloroform/IPA baths. The sample was then rinsed with IPA, dried under N_2 gas and annealed in Ar/H_2 at 225 °C for 30 min.

The SiO_2 substrate was mounted into a dual-inline package using UHV compatible, high temperature resistant and electrically conductive silver epoxy. The

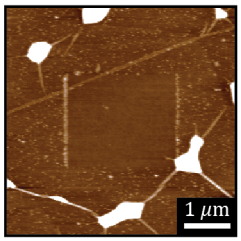

Figure 2.14: Topographic AC mode AFM image of graphene transferred onto silicon substrate. The 2 µm square in the centre of the image area has been cleaned using contact mode AFM, to push the dirt aside, seen clearly as a build-up around the central square.

electrodes were then connected to the package frame with gold-wire-bonding. This sample design can be used for both UHV ARPES experiments as well as ambient AFM, incorporating gating into both, given appropriate custom-made holders to connect to the package pins.

2.4.2 Measurement preparation

AFM cleaning

After sample fabrication, additional steps of cleaning can be done before measurements to improve the quality of photoemission results. Some residue is left on the surface after fabrication, even after annealing, which is often seen in AFM measurements. This is likely residue from the solvent dissolving the PC film, which then clumps up during the annealing, seen as small specks over the surface in AFM, and contributes to background signal in ARPES measurements. Fig. 2.14 is a tapping mode AFM topography map which shows a sample of graphene transferred onto a SiO_2 substrate and shows the white specks of contamination.

It is worth noting that there are contamination bubbles visible in this AFM image. These are a result of the self-cleaning mechanism seen in a number of 2D HSs, a process by which contamination between layers migrate together to form bubbles between the layers during the final annealing process in fabrication, leaving regions of atomically sharp interface in-between the pockets [47].

A method of improving samples which have this residue is to use the AFM tip in contact mode to push the contamination away from a small region. In the centre of this image is a square region which has been manually cleaned in this manner, leaving a cleaner 2 x 2µm^2 region in the centre. In order to use the AFM tip in this manner, one must balance the number of lines in a scan with the size of the tip. For example, the diameter of tip, if modelled as a ball at the end, used in this example was roughly 10 nm [125, 128]. In order to cover the entire 2 x 2µm^2

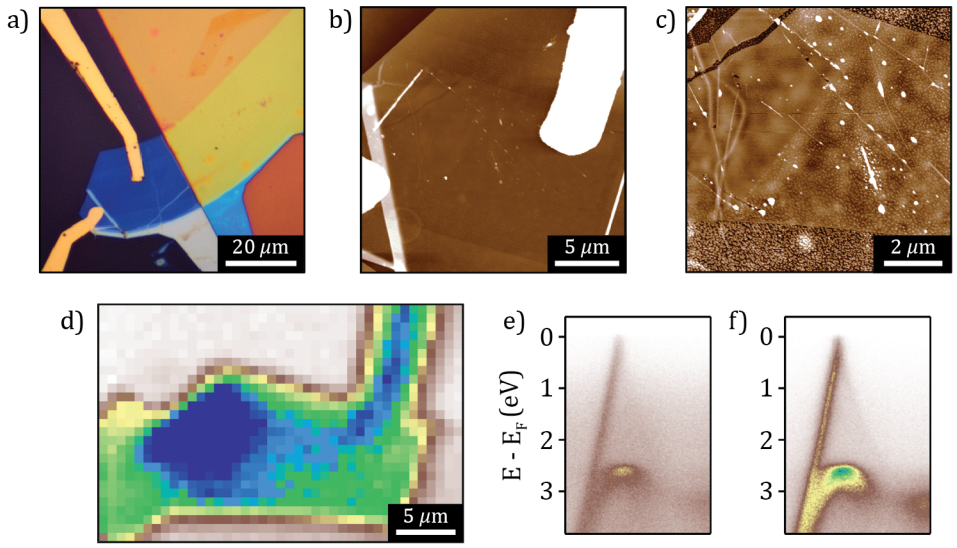

Figure 2.15: Graphene/hBN HS, courtesy of K. Novoselov's group at the University of Manchester. a) Optical micrograph of the HS. b) and c) AC mode AFM topography images of the sample, with the contact mode cleaned regions shown in c) as a cleaner region with residue build-up around the edges. d) SPEM map of the sample, with the cleaned region show clearly by the brighter blue box, indicating a change in photoemission. Energy-momentum slice through the graphene Dirac point from e) an untreated region and f) an AFM cleaned region.

square, the tip would need to take at least 200 passes to fully cover the scan region from top to bottom. To ensure it was fully covered, the AFM was set to do 512 lines per scan. The build-up of dirt is clearly visible around the cleaned region.

Fig. 2.15 shows a sample which has been AFM cleaned and then studied using ARPES. Fig. 2.15 a) is an optical micrograph of the sample. Fig. 2.15 b) and c) are AFM topography images of the sample, with a cleaned region shown by the build-up of dirt around a cleaned square, made up of four 2μm^2 cleaned regions next to each other. The same area is seen in the SPEM image in Fig. 2.15 b) as the darker blue region. Fig. 2.15 e) and f) show energy-momentum slices of the Dirac cones of graphene of the untreated and cleaned region respectively. In the cleaned region, the background is reduced and the graphene band is considerably sharper, which indicates taht this technique is effective for improving ARPES measurement of transferred samples. This technique was used effectively on a number of samples, prior to ARPES, in order to improve the quality of the measurements.

UHV considerations

ARPES measurement were performed within UHV, making controlling the electrical contacts more complicated. Both Elettra and Diamond have the capacity to apply gate voltage and current to a sample during measurements, though require careful sample prep.

Typically, ARPES samples can be affixed directly onto a UHV plate, either with silver epoxy or strip welding. For gated samples, sample mounting was more complex to account for electrical connections, and different across beamlines. At Diamond, the package was placed into a custom alumina holder, fixed to the UHV plate as shown in Fig. 6.1. The legs from the package were in physical contact to electrical slots within the holder. These slots where then in contact with pins at the bottom of the plate once in UHV, which made electrical connection once in the analysis chamber. Current was measured using a DDPCA-300 Sub Femto Ampere Current Amplifier.

At Elettra, a riser was attached to a UHV plate, with three contact pins at the bottom, shown in Fig. 6.5. The package was glued with silver epoxy onto the riser, and manually fixed down with a wire running over the top of the package, affixed to the plate. Bare wire was wrapped around the legs of the package, connected to the electrodes and the wire was held in place using silver epoxy. The other ends of the wire were then connected directly to the pins at the bottom of the UHV plate. These then make an electrical connection once in the analysis chamber of the UHV system, with voltage controlled with a Keithley 487 Picoammeter which also measured the current.

One of the main issues with ARPES is the surface sensitivity of the technique. AFM cleaning helps to remove fabrication contamination. However, as the samples are constructed and transported in air, particles will adsorb onto the surface during the time between fabrication and loading into UHV. These particles contaminate the sample and hinder ARPES results, leading to incoherent scattering and can effect the exit and flight of photoelectrons. In order to achieve cleaner samples, it is typical to anneal samples within UHV, before measurement. This acts to remove most of the surface contamination from transporting the samples.

For our samples, we found the most effective method was to slowly increase the temperature of the anneal, whilst observing the UHV chamber pressure in order to monitor any out-gassing, then continue to anneal the sample for $1 - 12\,\mathrm{h}$.

We found that simple MX_2 samples without encapsulation could be annealed to roughly $300 - 400\,^{\circ}\mathrm{C}$ for a few hours. For example, the data in Chapter 4 of exposed WSe_2 was taken from a sample which had been annealed at $350\,^{\circ}\mathrm{C}$ for

roughly 4 h. This gave a clean sample with sharp bands.

Samples can usually be annealed at a higher temperature if they are encapsulated by either graphene or ML hBN, as the encapsulation acts to protect the flakes underneath and graphene can withstand higher temperatures in UHV. Graphene samples could be annealed hotter, for a shorter length of time, usually because they have undergone less transfer processing and therefore have less contamination. For instance, a sample consisting of graphene grown on copper foil only needed to be annealed at 200 °C for 1 h in order to achieve sharp bands.

It is worth noting that this annealing procedure also works well for other materials. For example, we performed similar annealing on an InSe sample which was successful cleaned by annealing 350 °C for roughly 2 h [85].

Electrically gated samples which were mounted on chip carriers required longer anneal times, typically overnight or up to 12 h. Higher out-gassing rates were observed, likely due to the slightly porous nature of the chip carrier material.

By combining all of the above sample preparation, sufficiently clean exfoliated and transferred samples were achieved, making it possible to study them with a very surface sensitive technique such as ARPES.

Chapter 3

Layer dependent electronic structure of MX_2 monolayers and heterostructures

3.1 Introduction

The electronic properties of MLs can vary dramatically; from semiconductors to semi-metals to insulators. This makes them interesting for a number of different applications including optoelectronics [129] and electronics [3, 130].

A particularly interesting character of several TMD MLs, including the MX_2 family, is the change from indirect bandgap in bulk and BL to direct bandgap in ML [33, 103]. This is particularly useful in optoelectronics due to increased photoluminescence from MLs [38].

While these materials are of interest in isolation, research is being focused on stacking these 2D materials into HSs, enabling the engineering of new electronic and optoelectronic devices [3, 4, 87, 131–133]. For example, stacks of WSe_2 on $MoSe_2$ (both direct bandgap semiconductors in their ML form [33]) have demonstrated electrically tuneable interlayer excitons due to the type-II band alignment between the layers [59, 67].

Such rational band structure engineering requires understanding of the layer dependent electronic structure of the individual materials, and how they change when combined into multi-layer structures [87, 134, 135]. Indirect measurements of band structures have typically been used such as Raman spectroscopy [38, 136], photoluminescence [88, 137, 138], STS and STM [92, 139, 140].

Direct measurements of the layer dependent electronic structure have been

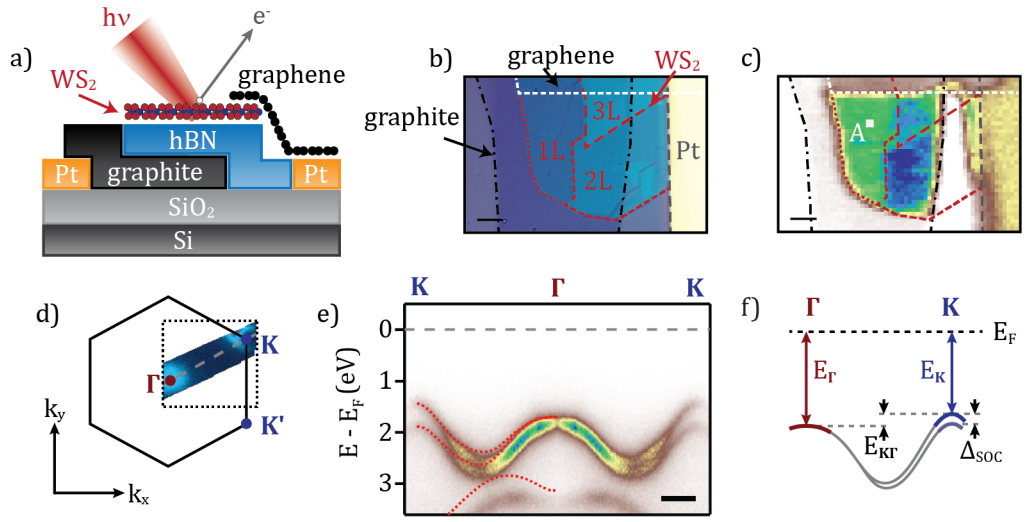

Figure 3.1: a) Schematic of ML WS_2 sample for photoemission. b) Optical micrograph of sample with outlines for Pt electrode (tan), graphite back-gate (black), WS_2 (red) and graphene top contact (white). c) SPEM map of the same sample location. Scale bars are 5 µm. d) First Brillouin zone of WS_2, with the constant energy slice of the **Γ** - **K** region mapped using ARPES, at a binding energy of (1.675 ± 0.005) eV. e) Band dispersion along the **Γ** - **K** direction, indicated with the dashed grey line in d). The data has been symmetrised around **Γ**, with DFT overlaid in red. Scale bar 0.3 $Å^{-1}$. f) Schematic of ML band dispersion showing measurable band parameters.

implemented using ARPES. The technique is sensitive to the top few layers of the materials; thus it can be used to study both MLs and HSs [88].

This chapter will focus on band structure mapping of ML MX_2 materials, graphene encapsulation and MX_2 HSs. It shall demonstrate measurements of band alignment between layers and subsequent quantification of crucial band parameters such as: band offsets at high symmetry points **Γ** and **K**, **Γ** - **K** band alignment, effective masses and SOC. These will be used to help illustrate the orbital contribution of the bands in order to understand how they combine and interact together.

3.2 Results and discussion

3.2.1 Characterising MX_2 monolayers

We have used spatially resolved ARPES to measure the band structure of mechanically exfoliated MX_2 materials. Fig. 3.1 illustrates the technique being used to study a WS_2 sample. The sample is made by mechanical exfoliation, as outlined in Chapter 2, with the HS stack shown in the schematic in Fig. 3.1 a). Fig. 3.1 b) shows an optical micrograph of the sample, with flake outlines labelled. The hBN

layer acts to isolate the WS_2 from the graphite, while the graphene strip along the top grounds the flake to an electrode.

Fig. 3.1 c) shows a SPEM map of the same region shown in Fig. 3.1 b). For SPEM, the pixel value is given by the integrated intensity of photoemission measured by the analyser's detector. The photoemission intensity is related to the band structure of the material being probed so changes in contrast can be used to identify different regions, explained in more depth in Chapters 2 and 6. It is worth noting that the graphene flake noticeably reduces the intensity of photoemission from the WS_2. This can decrease the signal to noise ratio for ARPES measurements, so where possible exposed flakes have been used to study ML band structures.

The white box, labelled A, on Fig. 3.1 c) shows the location on the exposed ML WS_2 region chosen to map the band structure. Fig. 3.1 d) shows the first BZ of WS_2 with the high symmetry points $\mathbf{\Gamma}$, $\mathbf{K}$ and $\mathbf{K'}$ labelled. A constant energy slice, at binding energy $(1.675 \pm 0.005)\,\mathrm{eV}$, is shown within the dashed box showing the region of k-space that was mapped out. To obtain this dataset, the beam was held stationary at A, then the angular coordinates of the detector were varied while taking an energy-momentum slice at a number of discrete coordinates. These energy-momentum slices were then stitched together to form a 3D dataset in k_x, k_y and energy, E. A 2D image was then extracted from the 3D dataset, along the $\mathbf{\Gamma}$ - $\mathbf{K}$ direction (the grey line in Fig. 3.1 d)). The full band dispersion is shown in Fig. 3.1 e), with the slice symmetrised around the $\mathbf{\Gamma}$ point. Therefore, this slice shows the $\mathbf{K}$ - $\mathbf{\Gamma}$ - $\mathbf{K}$ direction, rather than the $\mathbf{K'}$ - $\mathbf{\Gamma}$ - $\mathbf{K}$ one might expect by taking a slice extended across the whole BZ. Fig. 3.1 f) is a band schematic showing the band parameters and energies which have been fit, measured and extracted from the energy-momentum slice in Fig. 3.1 e).

Fig. 3.1 e) includes overlaid DFT calculations for 1L WS_2, aligned such that the calculated VBM at $\mathbf{K}$ matches that of the measured band structure. The DFT is courtesy of Nicholas Hine's group at the University of Warwick, calculated using Quantum ESPRESSO code [88].

The DFT, which includes spin-orbit interactions, is in good qualitative agreement with results. It correctly predicts the number and alignment of bands at both $\mathbf{\Gamma}$ and $\mathbf{K}$. However, quantitatively the DFT is not accurate. It does not give the correct $\mathbf{\Gamma}$ - $\mathbf{K}$ band offset and underestimates the band width. This shows that while DFT calculations can be used to qualitatively understand and estimate the band structure it cannot be used to make exact predictions. Theoretical calculations can be improved by using GW approximations, which include many-body interactions and can therefore improve the accuracy of predicted band structures, but are most

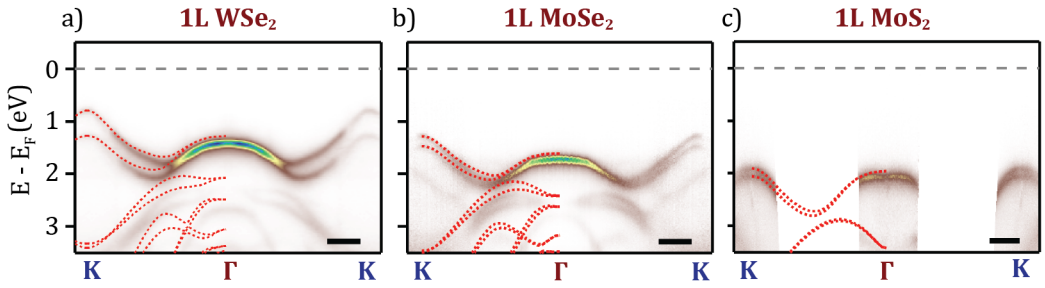

Figure 3.2: Band dispersion along the **Γ** - **K** direction of 1L a) WSe_2 and b) $MoSe_2$. c) Band dispersion slices around **Γ** and **K** of ML MoS_2. DFT predictions overlaid in red. Scale bars are $0.3\,\text{Å}^{-1}$.

effective when used in conjunction with direct experimental results [29, 141, 142].

From fitting the bands around **Γ** and **K** with parabolic functions, the band parameters have been calculated for ML WS_2 including: band maximum at **Γ**, $E_{\mathbf{\Gamma}}$; and band maximum at **K**, $E_{\mathbf{K}}$; band alignment between **Γ** and **K**, $E_{\mathbf{\Gamma K}}$; effective mass at K, $m^*_{\mathbf{K}}/m_e$; and SOC, Δ_{SOC}. These values are given in Table 3.1.

The same band parameters have been measured for the full family of MoWSeS MLs using the same sample fabrication and experimental techniques. Fig. 3.2 shows the band structure of a) ML WSe_2, b) ML $MoSe_2$ and c) ML MoS_2. Fig. 3.2 a) and b) are full **Γ** - **K** energy-momentum slices. Fig. 3.2 c) shows energy-momentum slices at **Γ** and **K** individually. From these data sets, the band parameters have been measured and are displayed in Table 3.1. All have been symmetrised around **Γ** with the DFT aligned to the band maximum at **K**. As with WS_2, the DFT shows reasonable qualitative agreement with measurements but underestimates **Γ** - **K** alignments, and band width, and thus should be used with caution.

From the measured band structure, we note a few key features. Each ML has a local VBM at **Γ** and a global VBM at the **K** point, indicative of a direct bandgap. The dominant contribution to the states at **Γ** is a linear combination of the metals' out-of-plane d_{z^2} orbitals and the chalcogens' out-of-plane p_z orbitals [18, 38, 88]. For ML MX_2, this results in a single band and local maximum at **Γ**.

The dominant contribution to the states at the **K** points are from the metals' in-plane d_{xy} and $d_{x^2-y^2}$, which then hybridise to the p_x and p_y orbitals of the chalcogen. This results in global valence band maxima at the **K** points.

The bands at **K** are split due to spin-orbit effects of the metals' d orbitals, and a lack of inversion symmetry within the crystals [38]. In the region of the **K** points, **K** and **K′**, the strong SOC leads to an effective coupling between the spin and the pseudospin of the **K** valleys [29]. This results in the spin index of the VBM

Material	$E_{\mathbf{\Gamma}}$ (eV)	$E_{\mathbf{K}}$ (eV)	$E_{\mathbf{\Gamma K}}$ (eV)	Δ_{SOC} (eV)	$m^*_{\mathbf{K}}/m_e$
1L WSe_2	1.42 ± 0.02	0.80 ± 0.01	0.62 ± 0.01	0.49 ± 0.01	0.42 ± 0.05
1L $MoSe_2$	1.52 ± 0.02	1.04 ± 0.02	0.48 ± 0.03	0.22 ± 0.03	0.5 ± 0.1
1L MoS_2	2.07 ± 0.02	1.93 ± 0.02	0.14 ± 0.04	0.17 ± 0.04	0.7 ± 0.1
1L WS_2	1.83 ± 0.02	1.44 ± 0.02	0.39 ± 0.02	0.47 ± 0.02	0.40 ± 0.05
2L WS_2	1.32 ± 0.02	1.42 ± 0.02	-0.10 ± 0.02	0.48 ± 0.02	0.37 ± 0.05
3L WS_2	1.23 ± 0.02	1.44 ± 0.02	-0.21 ± 0.02	0.47 ± 0.02	0.31 ± 0.05

Table 3.1: Measured band parameters from ARPES band dispersions for ML MX_2 materials and few layer WS_2, including: band maxima at $\mathbf{\Gamma}$, $E_{\mathbf{\Gamma}}$; band maxima at $\mathbf{K}$, $E_{\mathbf{K}}$; band alignment from $\mathbf{\Gamma}$ - $\mathbf{K}$, $E_{\mathbf{\Gamma K}}$; magnitude of SOC, Δ_{SOC}; and effective mass, $m^*_{\mathbf{K}}$, in units of an electron's rest mass, m_e.

being locked to the valley index at $\mathbf{K}$, i.e. spin up at $\mathbf{K}$ and spin down at $\mathbf{K'}$. This also results in valley dependent optical selection rules, which are important for ARPES as either $\mathbf{K}$ or $\mathbf{K'}$ will have greater photoemission, depending on the beam polarisation, and this influences the experimental limits for imaging the bands.

The magnitude of SOC is heavily dependent on the metals as its orbitals provide most of the spin-orbit interaction [143]. This is seen clearly in Table 3.1 where Δ_{SOC} is much larger for W compared to Mo compounds [38]. We also see that the band alignment of $E_{\mathbf{\Gamma K}}$ depends more on the chalcogen than the metal with larger band offset for Se than S compounds, which agrees with theory [141]. However, no simple relation controls the $E_{\mathbf{\Gamma K}}$ although studies show it relies more on the X-M-X bond angle, and therefore varies with each compound [69].

3.2.2 Layer dependent band structure of WS_2

We have also used ARPES to study the layer dependent evolution of the band structure of WS_2. It is a well-known phenomena that MX_2 materials progress from a direct bandgap in ML form, to indirect bandgap in BL, trilayer (TL) and bulk [18]. The main cause for changes in the band structure of MX_2 materials is due to overlapping orbital contribution from additional layers. Therefore, we expect to see the largest structural change in the part of the band associated with the out-of-plane orbitals, i.e. around $\mathbf{\Gamma}$.

Fig. 3.3 shows the measured band structure of 1L, 2L and 3L WS_2. Fig. 3.3 a) is a SPEM map of the same sample as Fig. 3.1. Angle integrated spectra are extracted from the locations indicated by the three white squares to give the line profiles in Fig. 3.3 b). The spectra are different due to the different number of layers and can be used to easily identify each region. Fig. 3.3 c) shows a map of

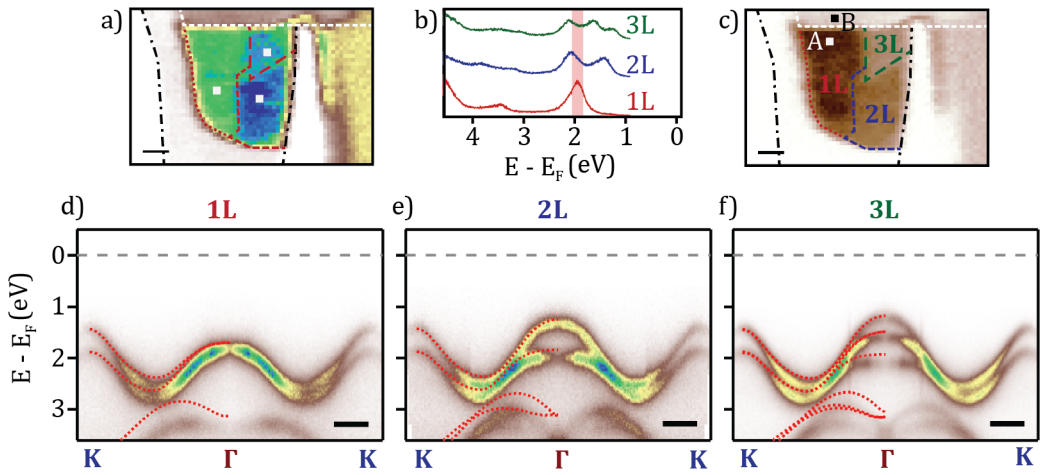

Figure 3.3: a) SPEM map of the WS_2 sample shown in Fig. 3.1. b) Angle integrated spectra, taken from the white squares in a), to identify the different number of layers: 1L, 2L, and 3L. c) Map showing integrated intensity of a), integrated in the energy region shaded red in b). Highest intensity is from the 1L as it has the largest peak in this energy range. Scale bars are 5 µm. Band dispersions along the **Γ** - **K** direction for d) 1L, e) 2L, and f) 3L WS_2. Each has been symmetrised around **Γ** with DFT overlaid in red and aligned to $E_{\mathbf{K}}$. Scale bars are 0.3 Å^{-1}.

integrated intensities within the energy range given by the shaded red box in Fig. 3.3 b), across the whole map of Fig. 3.3 a) to emphasise the different regions. Fig. 3.3 d), e) and f) are the band dispersions extracted along **Γ** - **K** for 1L (ML), 2L (BL) and 3L (TL) respectively. Each has been symmetrised around **Γ** with DFT overlaid and aligned to match the measured band maximum at **K**. The fitted band parameters and band alignments are all given in Table 3.1.

The biggest change visible with an increase in layers is an increase in the number of bands at **Γ** and a corresponding increase in the local band maximum. The global VBM shifts from **K** in 1L to **Γ** in 2L and 3L. The change in band structure at **Γ** and shift from direct to indirect bandgap is a consequence of interlayer hopping. The overlap in the transition metal d_{z^2} orbital, and the chalcogen p_z orbital to a lesser extent, at **Γ** increases with additional layers [144]. This leads to large interlayer hoping and band hybridisation due to the relatively delocalised, antibonding nature of the orbitals [38].

The band at **Γ** splits into two bands for 2L, three bands for 3L etc. The size of the split between the bands at **Γ** is indicative of hopping strength. If one could see the conduction band, we would also see the minima at the **Q** point hybridising, though to a much smaller extent as it has contributions from overlapping p_z orbitals. As a result, the **Q** point is brought down in energy, while the **Γ** band is brought up,

and the band maximum rises to overtake the bands at **K** as VBM, as seen in the figure. While only the VB is visible here, the CB will be discussed in Chapter 4.

As the bands at **K** are dominated by in-plane orbitals, there is no noticeable difference in band structure at **K** between layers. The energy maximum, $E_{\mathbf{K}}$, given in Table 3.1 does not change with 1L, 2L, or 3L. The spin-splitting, Δ_{SOC}, is also independent of the number of layers. This is because the spin orbit interaction and lack of inversion symmetry does not change with additional layers, therefore Δ_{SOC} remains roughly constant from ML to bulk, and interlayer hopping effects are suppressed. Similarly, if we could image the CB then the minima at **K** would remain unchanged and exhibit a small Δ_{SOC} of a few meV.

Therefore, as the valence band at **Γ** increases with layers and the conduction band at **Q** lowers, while **K** remains stationary, then the bandgap shifts from direct in MLs to indirect in multilayers, as predicted theoretically [3, 29, 103, 130].

The DFT predictions overlaid in Fig. 3.3 exhibit the same band behaviour, and it is this direct bandgap that is one of the features that make ML MX_2 attractive for device design.

3.2.3 Band alignment with graphene

In addition to changes in the electronic structure with multilayer stacking, it is important to understand how interlayer interactions effect band structure when stacked with different materials. For instance, the out-of-plane interactions are regularly drawn on when creating 2D devices. In a number of these devices, graphene is used as a 2D contact, layered next to or on top of the flake in question. It is important to understand how the out-of-plane interactions effects graphene's band structure, and that of the flake itself. Graphene is also used to form a protective encapsulation layer on top of samples which is especially useful for air sensitive materials [48]. Many studies show that graphene protects the sample from air, and also help keep it clean [47]. During annealing, dirt between layers come together to form blisters of contamination in an otherwise pristine interface. In this study, and our previous studies, we find that graphene is effective at preserving the band structure and creates clean samples.

Thus, it is important to understand how graphene affects the band structure. Previous studies have shown that graphene and MX_2 layers interact weakly [87]. For larger binding energies, away from the Fermi energy by a few eV, they observed bandgaps and anti-crossing where the Dirac cone crossed the MX_2 bands. Otherwise the band structure remained unchanged, especially for the highest valence bands. This was a result of the weak interlayer van der Waals bonds, much weaker than

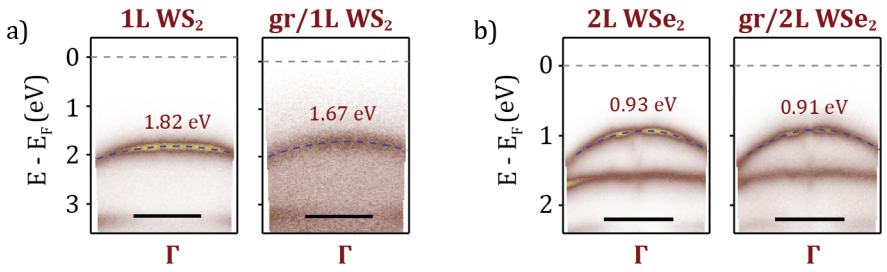

Figure 3.4: a) Band dispersion around $\mathbf{\Gamma}$ for exposed 1L WS_2 (left) and graphene capped i.e. gr/1L WS_2 (right). b) Band dispersion around $\mathbf{\Gamma}$ for exposed 2L WSe_2 (left) and graphene capped i.e. gr/2L WSe_2 (right). Band maxima were calculated from fitting a parabolic function to the band. Scale bars are 0.3 Å^{-1}.

the in-plane covalent bonds that dictate most of the band structure.

It is interesting to look for any charge transfer between graphene and MX_2 layers. Efficient charge transfer is required for HS devices. Some studies have shown fast transfer of injected charge [145]. This effective charge transfer could also effect stationary band alignment within graphene capped MX_2 HSs.

Fig. 3.4 shows the bands at $\mathbf{\Gamma}$ for two different materials, both with and without graphene encapsulation. Fig. 3.4 a) shows 1L WS_2, exposed (left) and graphene capped (right). Fig. 3.4 b) shows the same for exposed (left) and encapsulated (right) 2L WSe_2. The energy of the local band maximum at $\mathbf{\Gamma}$, $E_{\mathbf{\Gamma}}$, has been calculated from a parabolic fit to the bands, and is shown. The faint band seen in both panels below 3eV originates from the hBN layer below the WSe_2 and is not relevant to the discussion here.

Similar measurements have been taken for a number of MX_2 flakes with the results shown in Table 3.2. Both the exposed and encapsulated band maxima are given, with the shift between them defined as $\Delta E_{\mathbf{\Gamma}} = E_{\mathbf{\Gamma}}^{\text{exposed}} - E_{\mathbf{\Gamma}}^{\text{capped}}$. These results show a small but quantifiable shift in band maxima, from exposed to encapsulated regions, shifting $\mathbf{\Gamma}$ closer to the Fermi level when encapsulated.

This shows that the graphene has shifted the chemical potential of the MX_2 flake. The shift is likely due to a combination of the change in dielectric environment and some amount of charge transfer between layers. Previous studies have shown that a ML bandgap on TMD materials is highly sensitive to the dielectric environment [146]. The dielectric leads to a change in screening of the potential and leads to renormalisation of the bandgap [147]. Usually, higher dielectrics will reduce the bandgap [146]. Studies have demonstrated this with ML WSe_2 on graphite versus hBN [145]. For the samples encapsulated here, the graphene would therefore shift the band maximum upward, which we observe as the increase in $E_{\mathbf{\Gamma}}$.

Material	$E_{\mathbf{\Gamma}}^{\text{exposed}}$ (eV)	$E_{\mathbf{\Gamma}}^{\text{capped}}$ (eV)	$\Delta E_{\mathbf{\Gamma}}$ (eV)
1L WS_2	1.82 ± 0.03	1.67 ± 0.03	-0.15 ± 0.03
1L MoS_2	2.06 ± 0.03	1.80 ± 0.03	-0.26 ± 0.03
2L MoS_2	1.61 ± 0.03	1.32 ± 0.03	-0.29 ± 0.03
2L WSe_2	0.93 ± 0.03	0.91 ± 0.03	-0.02 ± 0.03

Table 3.2: Binding energies, $E - E_{\text{F}}$, of the band maxima at $\mathbf{\Gamma}$, $E_{\mathbf{\Gamma}}$, for exposed and graphene capped TMD flakes. The difference is calculated as $\Delta E_{\mathbf{\Gamma}} = E_{\mathbf{\Gamma}}^{\text{exposed}}$-$E_{\mathbf{\Gamma}}^{\text{capped}}$.

We also attribute some of the shift as a result of charge transfer between layers as $E_{\mathbf{\Gamma}}$ is not shifted by the same amount in each case. The graphene used is pristine, seen by sharp Dirac cones in Chapter 4. However, there is sometimes a small amount of doping seen in the graphene, potentially from trapped charge or gap states within the MX_2 flake [139]. MX_2 can exhibit doping, whether from natural or synthesised sources. This can come from defects, vacancies, substitutions or adsorbents [148]. For MoS_2, the primary source is from sulphur vacancies, especially from CVD grown crystals which leads to n-type doping [149, 150]. Charge transfer between the layers would shift the chemical potential upwards, which would be seen as a shift downwards in $E_{\mathbf{\Gamma}}$, which we observe.

The final shift observed is likely a combination of these effects. While it is not a massive change, of order less than a few 100meV, it is still significant as it is measurable, and the magnitude of this effect varies from sample to sample. The VB structure remains unchanged for the upper-most bands; therefore it is possible to quote relative band positions with respect to the graphene, and the relative alignments will hold for exposed flakes.

We can also compare these to the Kelvin force gradient microscopy (KFGM) results which show changes in the chemical potential for exposed and encapsulated regions, discussed in more depth in Chapter 6.

3.2.4 Band alignment within heterostructures

2D devices use the stacking of different 2D materials in order to achieve useful functional properties. For instance, several 2D devices have been created which use the relevant band alignment of the materials used [59]. As such, it is important to understand interlayer effects and hybridisation between different MX_2 layers when stacked on top of one another to form heterostructures.

HSs are samples of different ML materials stacked on top of one another. Each ML is held together in-plane with strong covalent bonds, while weaker van der

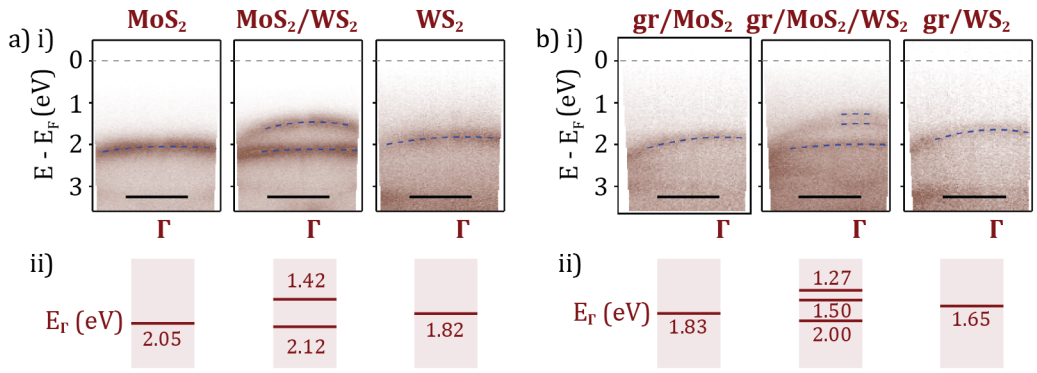

Figure 3.5: a) i) Band dispersion at **Γ** for commensurate MoS_2/WS_2 HS, showing bands for 1L material and heterobilayer region. b) Band dispersion at **Γ** for a $gr/MoS_2/WS_2$ HS with contributions from both commensurate and incommensurate regions. a) and b) ii) Schematic of the measured VBM at **Γ**, i.e. $E_{\mathbf{\Gamma}}$. Scale bars are $0.3\,\text{Å}^{-1}$.

Waals hold each adjacent layer together, in the same manner as multilayer samples. As such, we expect the same rules for out-of-plane interactions and potential hybridisation as observed in homobilayers.

HSs can be constructed in a number of different ways. One approach is to use bottom up techniques, e.g. using chemical vapour deposition to build layers individually from constituent elements. Another approach is to use top down techniques, by mechanically exfoliating MLs from bulk then manually stacking them, as done here. This can lead to different stacking arrangement, depending on the angle between layers [3, 38]. Aligned MX_2 layers can stack in either AA or AB stacking sequences. For AA stacking, the M/X sits directly above a M/X site in the layer beneath. For AB stacking, the M/X sits directly above a X/M site in the layer beneath.

A study by Constantinescu and Hine evaluated the factors that influence MX_2 HS hybridisation and found that hybridisation can occur between layers when the interlayer spacing brings the layers close enough together [151]. They found that provided the layers were close enough, hybridisation between layers would always been seen to some extent at **Γ**, where the bands are repelled by each other. The hybridisation is seen at **Γ** because there is momentum overlap, and **Γ** is rotationally invariant within the BZ. The extent to which the layers hybridise and the bands are repelled is dependent on the angle of rotation between the two layers. The greatest hybridisation occurs when the layers are well aligned, $<1°$, as the layers are closest together and one would expect to see a greater shift in the bands at **Γ**. This explains why strongly hybridised bands are seen in AB stacked homobilayers

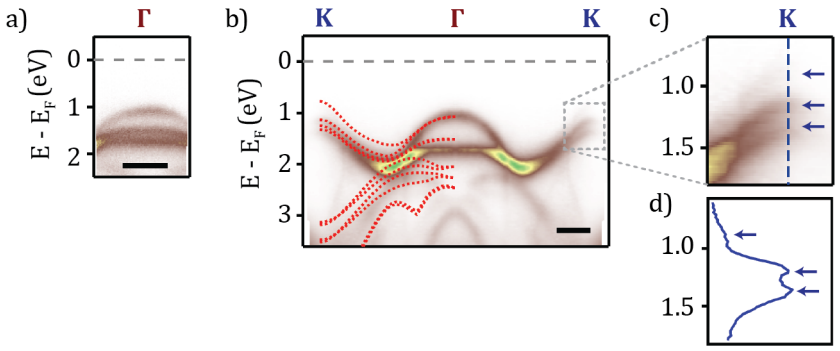

Figure 3.6: Band dispersion of a $MoSe_2/WSe_2$ HS. a) Taken at **Γ** on a region exhibiting both commensurate and incommensurate regions. b) Full **Γ** - **K** dispersion on commensurate heterobilayer region, symmetrised around **Γ**. DFT is overlaid for the heterobilayer (red). c) Enlarged region of dashed box in b), in order to see the bands at **K** whihc are highlighted with blue arrows d) Line profile taken along the blue dashed line in c), with the three bands highlighted with blue arrows. Scale bars are $0.3\,\text{Å}^{-1}$.

with a 180° rotation between layers, because at that angle the layers sit very close together with small interlayer spacing they have a greater momentum overlap and a significantly larger hybridisation [151]. There is very little change to the bands at **K** as there is almost no momentum overlap and thus minimal hybridisation occurs, as with homobilayers.

Fig. 3.5 a) shows a MoS_2/WS_2 heterobilayer. The panel on the left shows the band at **Γ** for ML MoS_2 and the panel on the right shows WS_2. The centre panel shows the bands at **Γ** for the HS region. Each band has been fit with a parabolic dispersion and the band maximum, $E_{\mathbf{\Gamma}}$, is given in the schematic below each corresponding panel, ii). The local maximum at **Γ** has moved upwards in the HS region as predicted for hybridised bands, higher than each individual material. Therefore, in this region the flakes are well aligned and hybridised.

Fig. 3.5 b) shows a graphene capped $gr/MoS_2/WS_2$ HS. Each panel shows the respective ML and HS region. The bands of the MLs and HS have been shifted due to the graphene cap, as outlined in the previous section. In the centre panel, which shows the HS, three bands are visible instead of two. The lowest and top most band are the two bands associated with the hybridised bilayer, as their separation of $(0.73 \pm 0.03)\,\text{eV}$ is comparable to the separation in Fig. 3.5 a) of $(0.70 \pm 0.03)\,\text{eV}$. However, the third band at $(1.50 \pm 0.02)\,\text{eV}$ is not associated to the heterobilayer.

The most likely origin of the third band is from an area of the sample which has not hybridised which the spot size of the ARPES beam is also covering, therefore it must be from the original MLs. As hybridisation depends on interlayer spacing,

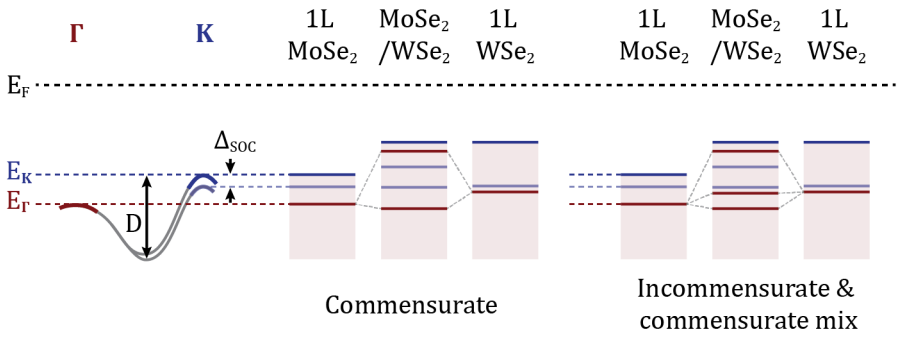

Figure 3.7: Schematic of band alignment and hybridisation within a $MoSe_2/WSe_2$ heterobilayer. Blue lines indicate **K** bands, red indicate **Γ**. For the commensurate HS, the band at **Γ** hybridise to two band. Three bands will be observed at **K**. For the mixed incommensurate and commensurate regions there are three bands at **Γ**.

for a region to remain un-hybridised the spacing between layers must be larger. This could be the due to a number of factors. As we have seen in Chapter 2, the fabrication of these HS can result in bubbles forming between layers which contain dirt and contamination, leaving an otherwise pristine interface. The bubbles would increase the spacing in very localised regions, which would be enough to prevent hybridisation.

Another reason for increased spacing could be the formation of commensurate and incommensurate regions across the sample [88]. A commensurate region is when the two layers are aligned with the same atomic positions, lattice spacings and periodicity. An incommensurate region is when the layers have different lattice spacing and could also include angular rotation between layers. There is a small lattice mismatch between MX_2 materials so when the angle between layers is small enough, $<1°$, it is possible for the MLs to form regions of commensurate HS surrounded by strained, incommensurate regions. This has been observed in similar HSs, including a hBN/graphene HS [152]. These commensurate and incommensurate domains are of finite size, usually less than the size of the ARPES photon beam. Thus it would be possible to get emission from both the commensurate and incommensurate concurrently which is likely the reason three bands are visible [88].

In Fig. 3.5 b) the energy of the third band does not exactly correlate with either ML in this case. However, it is still the most likely origin of the third band and an additional strain in the system, possibly from within the incommensurate regions themselves, could cause the energy of the band to shift [153].

This mix of both commensurate and incommensurate regions has also been measured in other samples. Fig. 3.6 shows a $MoSe_2/WSe_2$ sample with both com-

mensurate and incommensurate regions. Fig. 3.6 a) shows band dispersion at **Γ** taken on a region exhibiting three bands, indicating a mix [88]. Fig. 3.6 b) shows the full **Γ** - **K** band dispersion of a commensurate heterobilayer region. At **Γ** the bands have hybridised into two bands, similar to a homobilayer, as the layers are close enough together for the out-of-plane orbitals which contribute to the bands at **Γ** overlap.

Fig. 3.6 c) and d) shows the bands at **K**, where three bands are visible. Two are clear and a third, fainter band is just visible above them. This is indicative of a fully hybridised heterobilayer as the **K** points overlap in momentum, meaning the flakes are well aligned, $<1°$. There is only weak hybridisation at **K** due to the in-plane nature of the orbital contributing to the bands at **K**. Therefore, the bands at **K** remain predominantly unchanged from the original MLs.

DFT for the heterobilayer is overlaid in red. It has been aligned such that DFT matches the energy of the bands at **Γ**. The bands qualitatively look similar for theory and experiment. However, they do not match quantitatively as the exact band energies are not correct. While the energies do not match, the DFT helps demonstrate that two band are expected at **Γ** and three bands at **K**. While there are four bands in total at **K**, two from each ML, two of them overlap very closely and are not resolvable in the limit of the energy resolution. Thus, we expect to see only three in the spectra, which matches our experimental data. For better energy estimation, GW calculations could prove more accurate though more computationally expensive [142].

Fig. 3.7 helps to illustrate the band hybridisation and visible bands for commensurate and mixed regions. The band maxima at both **Γ** (red) and **K** (blue) are shown for each ML and for the HS. In commensurate regions, two bands are visible at **Γ** and three at **K**, as is seen in the results. The **Γ** bands from each ML has hybridised to two bands, while the four bands at **K** overlaps such that three are visible. In the mixed region, **K** is unchanged, while three band are visible at **Γ**: two from hybridisation and one from the MLs, as observed experimentally.

Similar measurements of band alignments have been performed for a number of different MX_2 HSs. Table 3.3 shows all the HS we have successfully fabricated and studied, with the top flake along the top row and the bottom flake indicated by left columns. These were measured at either Elettra SPECTROMICROSCOPY, Soleil ANTARES or Diamond I05 as indicated in the table.

For each sample, the local band maximum at **Γ** was measured and fit for each individual ML and associated HS. The measured band alignments are shown in table Table 3.4 for each sample HS.

Bottom\Top	MoS_2	$MoSe_2$	WS_2	WSe_2
MoS_2	-			
$MoSe_2$	D** ***	-		
WS_2	A*, B*		-	
WSe_2		E*, F*	C**	-

Table 3.3: The heterostructures fabricated and measured experimentally using spatially resolved ARPES. Top most flake is indicated along the top row and bottom most flake is indicated along the left. * for samples measured at Elettra. ** for samples measured at Soleil. *** for samples measured at Diamond.

From this table and band shifts we can draw some important conclusions. In most cases we observe two hybridised bands at $\mathbf{\Gamma}$ for the HS, although we do also observe the mixed three bands on sample B. This shows that the fabrication and alignment technique used is effective for creating hybridised HS. We also note that for the hybridised bands, the local maximum at $\mathbf{\Gamma}$ always increases in energy. This is important for optoelectronics and intralayer excitons, as the band maximum may cause the layers to become indirect bandgap semiconductors. It is not possible to tell for sure as the CB is not visible here [18].

We also note that using a graphene cap does not prevent hybridisation, as a number of the hybridised samples have been protected with graphene. This is useful as it means it can be used for a contact without effecting that part of the hybridised band structure and protects of the HS.

Sample D was studied at both Soleil and Diamond. The exact band maximums have shifted between measurements which indicates some doping occurred in-between. This is reasonable, as many months passed between measurements, and studies have shown that these sample can become doped when stored in air and defects can move between the layers over time [154]. It is worth noting though that the relative band alignments are in agreement across beamlines.

3.3 Conclusions

Using spatially resolved ARPES, we have been able to map and measure the band structure of the full MX_2 family. The measured band structures and trends observed in the band parameters help illuminate the in-plane and out-of-plane orbital contributions in order to further understand these materials.

The layer dependent band structure of WS_2 helps to extend our descriptions and understanding to include interlayer interactions and confirms both in-plane and

Sample	Top flake, $E_{\mathbf{\Gamma}}$ (eV)	HS, $E_{\mathbf{\Gamma}}$ (eV)	Bottom flake, $E_{\mathbf{\Gamma}}$ (eV)
A	MoS_2	MoS_2/WS_2	WS_2
	2.05 ± 0.02	1.46 ± 0.02	1.82 ± 0.02
		2.12 ± 0.02	
B*	gr/MoS_2	$gr/MoS_2/WS_2$	gr/WS_2
	1.83 ± 0.02	1.27 ± 0.02	1.65 ± 0.02
		1.50 ± 0.02	
		2.00 ± 0.02	
C*	gr/WS_2	$gr/WS_2/WSe_2$	gr/WSe_2
	1.87 ± 0.03	1.40 ± 0.03	1.58 ± 0.03
		1.94 ± 0.02	
D*	gr/MoS_2	$gr/MoS_2/MoSe_2$	$gr/MoSe_2$
	1.76 ± 0.03	1.37 ± 0.03	2.19 ± 0.03
		2.15 ± 0.03	
D*	gr/MoS_2	$gr/MoS_2/MoSe_2$	$gr/MoSe_2$
	1.53 ± 0.05	1.05 ± 0.05	1.15 ± 0.05
		1.49 ± 0.05	
E*	$gr/MoSe_2$	$gr/MoSe_2/WSe_2$	gr/WSe_2
	1.42 ± 0.03	1.06 ± 0.03	1.58 ± 0.02
		1.62 ± 0.02	
F	$MoSe_2$	$MoSe_2/WSe_2$	WSe_2
	1.74 ± 0.02	1.08 ± 0.02	1.59 ± 0.02
		1.52 ± 0.02	
		1.74 ± 0.02	
F	$MoSe_2$	$MoSe_2/WSe_2$	WSe_2
	1.74 ± 0.02	1.06 ± 0.02	1.59 ± 0.02
		1.72 ± 0.02	

Table 3.4: HS band alignments measured using ARPES. Band maxima at $\mathbf{\Gamma}$, $E_{\mathbf{\Gamma}}$, is quoted for each ML flake and their associated heterostructures. All the samples were aligned to within a few degrees during fabrication, from using a straight edge on the exfoliated flake. Exact angle alignment is not possible to quote, and they could potentially be 30 or 60° rotated. * indicates graphene capped samples. All others are exposed.

out-of-plane characteristics of the interactions. From the increase in band maximum at $\mathbf{\Gamma}$ and the corresponding lack of change at $\mathbf{K}$ we can indirectly observe the transition from direct to indirect bandgap with the increase of layers. However, this description is currently based on the VB alone and will be extended to include the CB in the next chapter.

We have also shown how the substrate and dielectric environment can effect band structure. Graphene acts to slightly change the dielectric environment of the ML and contributes a small amount of charge transfer. It can be used effectively to

protect and encapsulate samples, while not disrupting the top most valence band structure. In future chapters we will see that this is crucial as it also an effective 2D contact and will be used extensively as such.

ARPES has also been used to study HS band alignment. The band structure of several MX_2 HSs have been studied in order to understand and illustrate the conditions required to form heterobilayers. Hybridisation occurs when the layers are close enough for orbitals in adjacent layers to overlap. The effect of hybridisation is seen strongest at $\mathbf{\Gamma}$ where they have the same energy, momentum, and out-of-plane orbital overlap. In contrast, there is almost no observable change at $\mathbf{K}$ for these structures. We also see that HS samples can form regions of finite commensurate and incommensurate domains, given their slight lattice mismatches. This is an important consideration for HS samples and device design.

Understanding the undoped bandstructures of MLs and HSs is crucial for band structure engineering in future as this will then allow us to compare and look at how these parameters might change in gated devices, which will be the topic of further chapters.

Chapter 4

Gating MX_2 heterostructures

4.1 Introduction

Andre Geim and Konstantin Novoselov won the 2010 Nobel Prize in Physics for their work regarding graphene. What made their work so significant was that they were able to elucidate a way of controlling the carrier concentration within the sample and were therefore able to modulate the conductivity of semi-metallic graphene. It was this crucial matter of electrostatically doping, or gating, the 2D material that illuminated graphene's unique and promising properties, both for studying fundamental physics as well as creating a new field of building 2D devices [7]. In their early graphene paper in 2004, they used single and few layer graphene to create a "metallic field-effect transitior" by stacking the flake vertically on an oxidised Si substrate, on top of n-doped silicon to which they applied a gate voltage [7]. This method of applying a gate voltage vertically through a dielectric is known as back gating. The geometry allows uniform gating of a 2D material in a way that is impossible for bulk materials, as the gate induced charge is screened by charge carriers inside a 3D material.

Potential 2D devices include semiconductor devices [4, 39, 155] such as FETs [63], spintronic devices [24, 25, 28] and optoelectronic devices [59], along with many other applications. They all depend on the ability to efficiently gate the 2D material, and a significant number employ back gating exfoliated flakes in vertical HSs.

Many applications, such as optoelectronic devices, depend on the band alignment within the sample to function efficiently. This requires understanding properties such as band offsets, band alignment between layers and the bandgaps of each material [156]. These dictate the functional properties such as interlayer excitons and gating dependent band alignment. As such, it is important to quantify these

band parameters in order to ensure efficient charge injections.

However, there are large discrepancies in quoted band parameters, in particular bandgaps, for 2D and MoWSeS materials. This is crucially important for understanding excitonic and interlayer excitonic behaviour. Different studies report a range of bandgaps, for example WSe_2's reported bandgap ranges from 1.4 eV up to 2.21 eV [92, 157–160].

The techniques typically used to measure bandgaps rely on indirect measurements; such as STM, STS, inverse photoemission and two-photon absorption [157–161]. As shown in previous chapters, we are able to directly probe the valence band structure of 2D materials using ARPES. By gating ARPES samples *in situ*, this would give control over carrier concentration, populating the conduction band and hence allow the bandgap and gate effects to be measured directly.

Conventionally, electron doping in ARPES is achieved by depositing electropositive atoms onto the surface, usually alkali metals [92, 102, 104–106, 162]. This introduces excess carriers to dope the top layer of a material. Under enough n-doping, the occupied electron states within a semiconductor sample can be increased to the point where the conduction band becomes occupied and therefore is visible on the measured photoemission spectra. However, this technique has limitations. The doping levels are hard to control or measure accurately and it is only reversed by a high-temperature anneal which can potentially damage the sample. It also does not dope uniformly and can change the chemical nature of the sample in an unpredictable manner.

Electrostatically doping the sample with contact electrodes and back-gate eliminates these limitations, while still doping the sample enough to study the conduction band and study the fundamental physics relevant to 2D materials. It also gives access to smaller carrier densities than alkali metal doping, which more accurately mimics the behaviour and densities relevant to practical devices.

This chapter will display and discuss our work using spatially resolved ARPES to study the band structure and development of electrostatically gated MX_2 heterostructures, focusing on WSe_2.

4.2 Results and discussion

4.2.1 Electrostatic doping of graphene

We first demonstrate the technique using a relatively simple electrostatically gated graphene heterostructure. The schematic of the graphene device used is given in Fig. 4.1 a). The flakes were mechanically exfoliated, as outlined in Chapter 2.

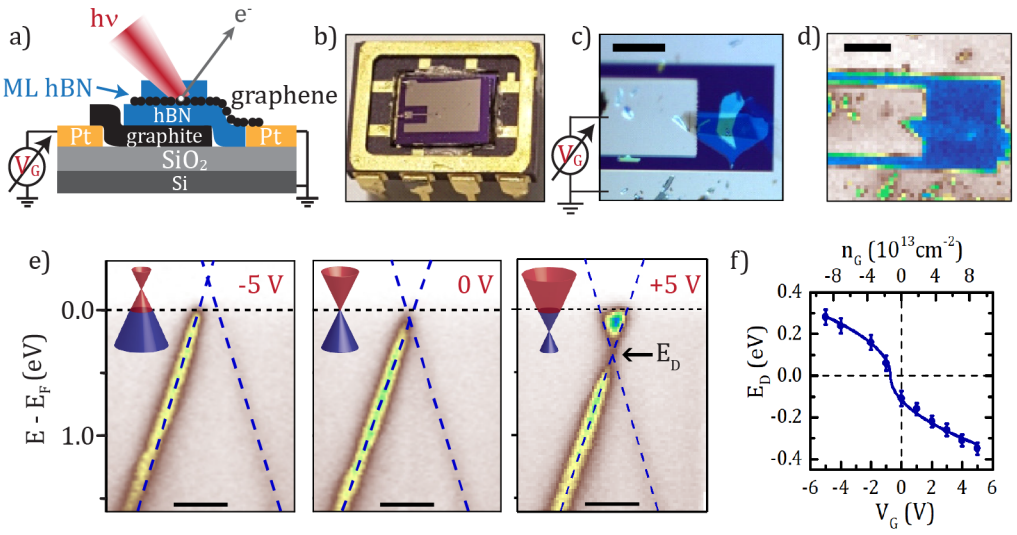

Figure 4.1: (a) Schematic of a 2D HS device of hBN-encapsulated graphene. The graphene is grounded while a gate voltage, V_{G}, is applied to the graphite back-gate. (b) Optical image of a device mounted in a standard 8-pin chip carrier. (c) Higher magnification optical image and (d) SPEM image showing the sample. Scale bar 50 µm. (e) Energy-momentum slices near the graphene **K**-point at the gate voltages labelled. Scale bars are 0.2 $\mathrm{\AA}^{-1}$. The dashed lines are linear fits where the Dirac point energy, E_{D}, is given from their intersection. (f) Gate dependence of E_{D}. The solid line is the prediction based on a linear dispersion, with the gate-induced electron density, n_{G}, (top axis) calculated from the capacitance.

In this sample, ML hBN was used to cap the graphene region, stacked onto a hBN dielectric on top of a graphite back-gate. The graphite is connected to the gate electrode, which is the small electrode in the bottom left of Fig. 4.1 b). The top graphene is connected to the grounded electrode, the large electrode covering the remainder of the chip. The large grounded electrode helps to minimise stray fields during gated measurements, which could potentially distort the flight of the emitted photoelectrons. The HS is located in the gap between the two electrodes, as shown by the optical image in Fig. 4.1 c). The same region is shown in the SPEM map used to locate the sample, in Fig. 4.1 d).

With the beam held fixed, energy-momentum slices were taken through the graphene Dirac point, **K**, shown in Fig. 4.1 e) for gate voltages $V_{\mathrm{G}} = -5$, 0 and 5 V. Each slice is taken close to the **Γ** - **K** direction of graphene's BZ, resulting in the reduced intensity on one side of the Dirac cone [110]. The bands show the expected linear dispersion consistent with being taken around the **K** point. The positive gate voltage has n-type doped the graphene layer, causing the Dirac point to shift down with respect to E_{F}. The negative gate voltage has done the opposite, shifting the

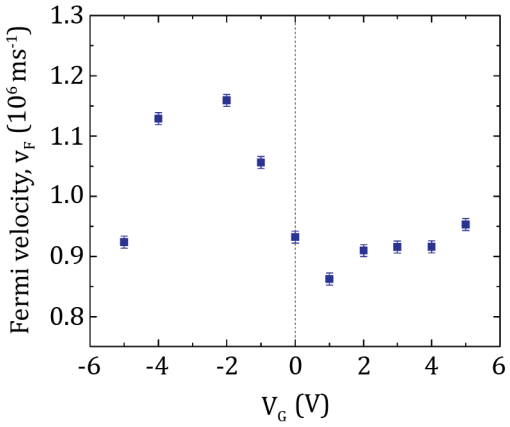

Figure 4.2: Extracted Fermi velocities verse gate voltage from the linear fitting of the Dirac cone dispersion of graphene. In cases where the intensity of the Dirac cone was much greater on side than the other, the more intense side was used to calculate v_F.

Dirac point up.

To determine the Dirac point energy, E_D, a linear fit was performed on each side of the cone within $E - E_F < 1\,eV$. The gradient of the fit gives the Fermi velocity, v_F, while the intersection of the lines on each side of the Dirac cone gives E_D.

The calculated Fermi velocity as a function of gate voltage is shown in Fig. 4.2. Previous studies report evidence for a reduction of up to 20 % in v_F for graphene films near E_D, for low doping levels ($\sim 1 \times 10^{12}\,cm^{-1}$) [163, 164]. This would lead to a slight distortion in the bands near the Dirac point. However, the spectrometer at Elettra where these samples were measured is not currently capable of resolving these differences. The variations seen in measured velocity is from the systematic errors of the experimental limitations such as the weak emission from one side of the cone and the extreme sensitivity to the exact alignment between energy-momentum slice and Dirac point.

The shift in E_D with respect to V_G is shown in Fig. 4.1 f). The fit for this data (solid blue line) is from considering the relationship given in Eq. 1.7 in Chapter 1, where E_D is related to carrier concentration in graphene. By considering both the intrinsic carrier concentration, n_0, and the gate induced carrier concentration, n_G, Eq. 1.7 becomes

$$E_D^2 = \pi\hbar^2 v_F^2 (n_0 + n_G) \tag{4.1}$$

where n_0 is given by the carrier concentration at $V_G = 0\,V$. The gate induced carrier concentration can be calculated by treating the heterostructure as a parallel plate

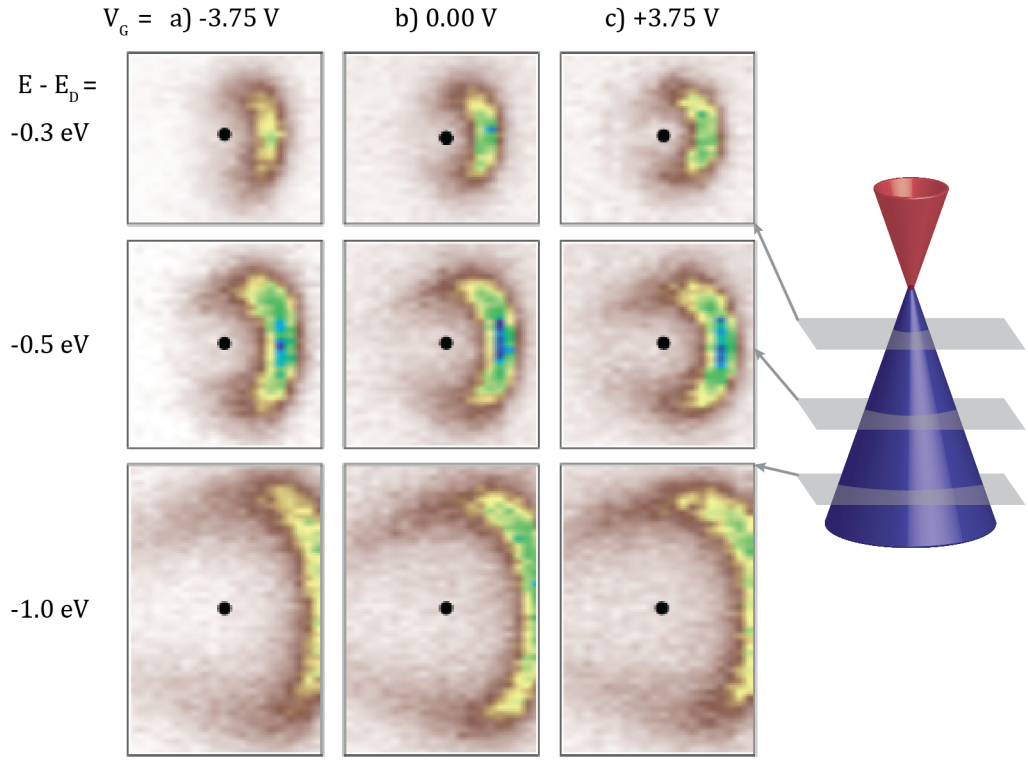

Figure 4.3: Constant energy slices through a graphene Dirac cone at the stated gate voltages. **K** is indicated with the black dots. Each panel is $4\,\text{Å}^{-1}$ wide.

capacitor, therefore

$$n_{\text{G}} = C_{\text{A}} V_{\text{G}} \tag{4.2}$$

where C_{A} is the capacitance per area. This then gives

$$E_{\text{D}} = \hbar v_{\text{F}} \sqrt{\pi (n_0 + C_{\text{A}} V_{\text{G}})}. \tag{4.3}$$

To fit the data in Fig. 4.1 f), C_{A} and n_0 were kept as free fitting parameters while a fixed value of $v_{\text{F}} = (9.3 \pm 0.1) \times 10^5\,\text{ms}^{-1}$ was taken from the linear dispersion fitting of the graphene bands at $V_{\text{G}} = 0\,\text{V}$. This fit gave an intrinsic carrier concentration of $n_0 = (1.8 \pm 0.1) \times 10^{12}\,\text{cm}^{-2}$ and capacitance of $C_{\text{A}} = (2.2 \pm 0.2) \times 10^{-7}\,\text{Fcm}^{-2}$. This is a relatively high n_0 for graphene, which even at room temperature usually only reaches roughly $9 \times 10^{10}\,\text{cm}^{-2}$ [13, 163] while our measurements were taken at 100 K, indicating some sample contamination. For capacitance, this can be com-

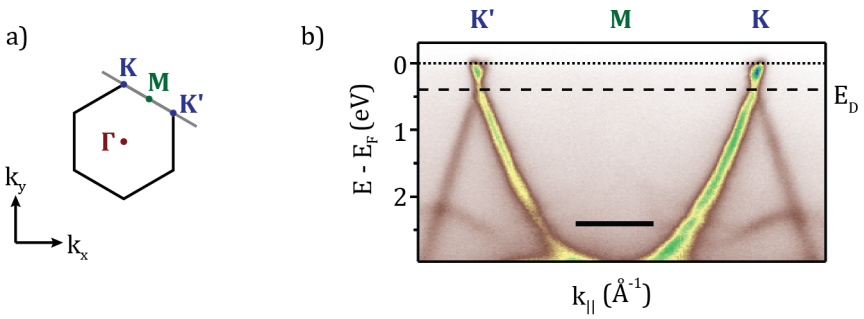

Figure 4.4: a) Schematic of the BZ, showing the direction through **K** and **K′** of the b) energy-momentum slice of gated graphene at $V_G = +3.35\,V$. Scale bar $0.5\,Å^{-1}$. The longer dashed line shows the energy of the Dirac points. In this sample, measurements were performed on a graphene layer stacked on top of ML WSe_2, which is responsible for the faint bands around 2 eV and lower.

pared to the expected areal capacitance

$$C_A = \frac{\epsilon_0 \epsilon_{BN}}{d_{BN}} \tag{4.4}$$

where d_{BN} is dielectric thickness, ϵ_0 is the vacuum permittivity and ϵ_{BN} is the relative permittivity of hBN. Using $d_{BN} = (14 \pm 1)\,nm$ obtained from AFM measurements, and $\epsilon_{BN} = 4.5$ from literature [16, 165], then $C_A = (2.5 \pm 0.2) \times 10^{-7}\,Fcm^{-2}$ and the value measured is reasonable. Quantum capacitance corrections are negligible for this case and will be discussed in full in Section 4.2.3. This fit gives agreement with both data and theory, showing that the electrostatic doping is effecting the graphene in a predictable and reliable manner.

However, it is important to check that the gating does not have an unexpected effect on the photoemitted electrons, crucially that stray electric fields within the set-up do not distort the measured dispersions. Fig. 4.3 shows constant energy slices extracted from the graphene Dirac cone, at different energies and gate voltages. The trigonal characteristics of the Dirac cones away from the Dirac point is not distorted by the gating. This indicates the emitted photoelectrons are not significantly distorted.

This is further confirmed by the undistorted dispersion shown in Fig. 4.4 b). On a similar graphene sample gated at $V_G = +3.35\,V$, the energy-momentum profile along the BZ boundary has extracted along the **K** - **K′** direction shown in Fig. 4.4 a). The spectrum is symmetric about **M**, seen by the fact the Dirac point energy is the same at both **K** and **K′**, and is consistent with a uniform graphene band structure.

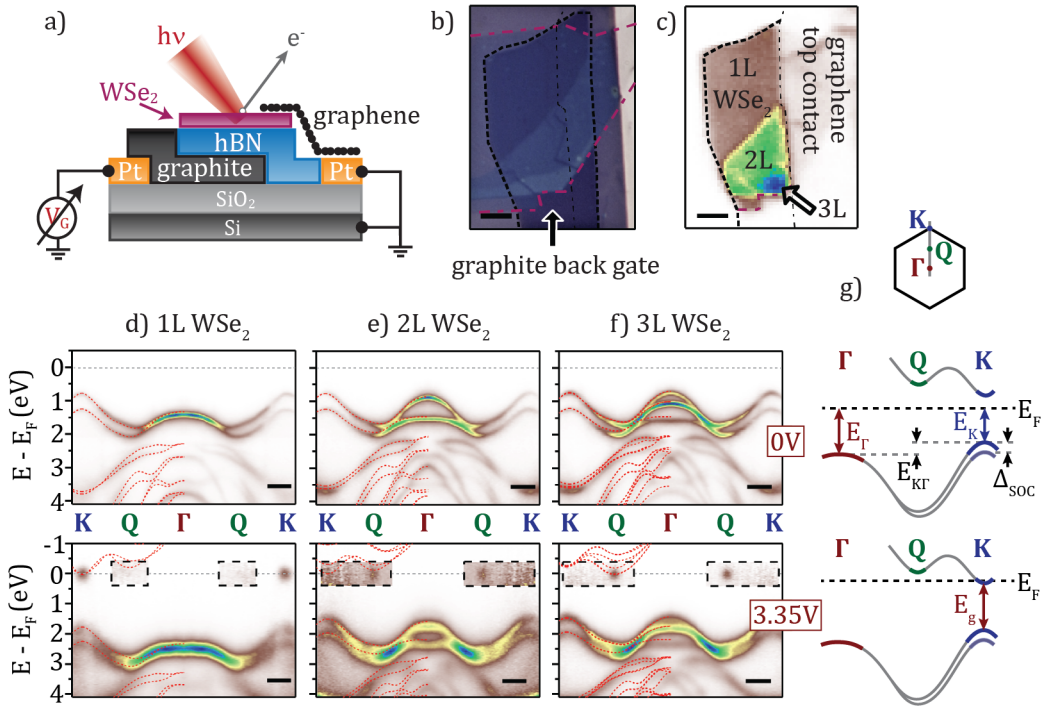

Figure 4.5: a) Device schematic where the graphene contact is grounded and the gate voltage is applied to the graphite back-gate. b) Optical and c) SPEM images of a WSe_2 device with ML, BL and TL regions identified. Scale bars are 5 µm. d) - f) Energy-momentum slices along **Γ** - **K** for ML, BL, and TL regions respectively. In each case, the upper panel is at $V_G = 0$ and the lower at $V_G = +\ 3.35$ V. Scale bars are 0.3 $Å^{-1}$. The data have been reflected about **Γ** in order to compare it to GW predictions (red dashed lines) performed by the Hine group. The intensity in the dashed boxes is multiplied by 20 to enhance the weak **Q** point features. (g) BZ of MX_2, and schematic of bands along **Γ** - **K**, showing definitions of energy parameters for both undoped (top) and doped (bottom).

To our knowledge, the measurements taken on graphene are the first to demonstrate the viability of gating samples during spatially resolved ARPES and quantitatively validate the technique.

4.2.2 Doping 2D semiconductors

We have also used gated ARPES to study other ML materials, including MX_2 samples. An exfoliated MX_2 flake can be incorporated into the stack between the dielectric hBN and graphene. A schematic of the MX_2 sample is given in Fig. 4.5 a). The graphene partially encapsulates the MX_2 flake, to provide contact while leaving a region exposed. No ML hBN was used to encapsulate the top of this sample.

Fig. 4.5 b) and c) are optical and SPEM images of the device, highlighting the ML, BL and TL regions of the flake. Fig. 4.5 d) - f) are energy-momentum slices measured from each region, respectively. The slice is taken along the **Γ** - **K** direction of the 2D BZ, as shown by the grey line in Fig. 4.5 g), as well as the measurable band parameters described in Chapter 3.

The top row shows measurements taken at $V_G = 0\,V$ which show only the valence band. The band progresses with layers as expected [18, 29, 38], the maxima at **Γ** rises with increased layers, overtaking **K** as VBM for TL.

Electrostatic doping populates the conduction band which can be seen in the bottom row, taken at $V_G = +3.35\,V$. The CBM becomes visible at **K** for ML WSe_2, and at **Q** for BL and TL (roughly halfway between **Γ** and **K**). This is consistent with the predicted transition from direct bandgap in ML MX_2, to indirect bandgap in BL and higher.

For ML WSe_2, both the VBM and CBM are at **K**, giving a direct bandgap. For BL WSe_2, the valence band at **Γ** has risen but the VBM is still at **K**. However, the CBM has shifted to **Q** instead of **K** resulting in an indirect bandgap. For TL, the valence band at **Γ** has over taken **K** to become the VBM and the CBM is still at **Q**, giving an indirect bandgap. It follows that with subsequent layers, and in bulk form, the bandgap will also be indirect as the VBM stays at **Γ**. This has been observed indirectly with methods such as photoluminescence [21, 22, 166] and has been predicted theoretically [141, 142, 167], but here is clear direct measurement of the transition. GW calculations are overlaid in red on the reflected half of the spectrum and agree with the measurements.

We successfully studied the full family of MoWSeS materials using the same technique. Samples were made with ML MoS_2, $MoSe_2$, and WS_2, with an example schematic shown in Fig. 4.6 a). Fig. 4.6 b) shows a schematic of the bands at **K**. Fig. 4.6 c) - e) show energy-momentum slices taken at **K** for each material. Each shows the ungated measurement, along with a gated measurement where the voltage is just high enough for the conduction band to become visible. Table 4.1 displays all the measured band parameters for ML, BL and TL WSe_2, as well as ML MoS_2, $MoSe_2$, and WS_2. In addition to all the standard band parameters one can obtain from μ-ARPES covered in Chapter 3, electrostatic doping allows us to directly measure the bandgap for these materials.

The bandgap of a TMD is given by $E_g = E_C - E_{\mathbf{K}}$. The energy of the CBM, E_C, can be estimated for a given carrier concentration, which for these measurements is $\sim 10^{13}\,cm^{-2}$, as discussed later in Section 4.2.3. The density of states at a single

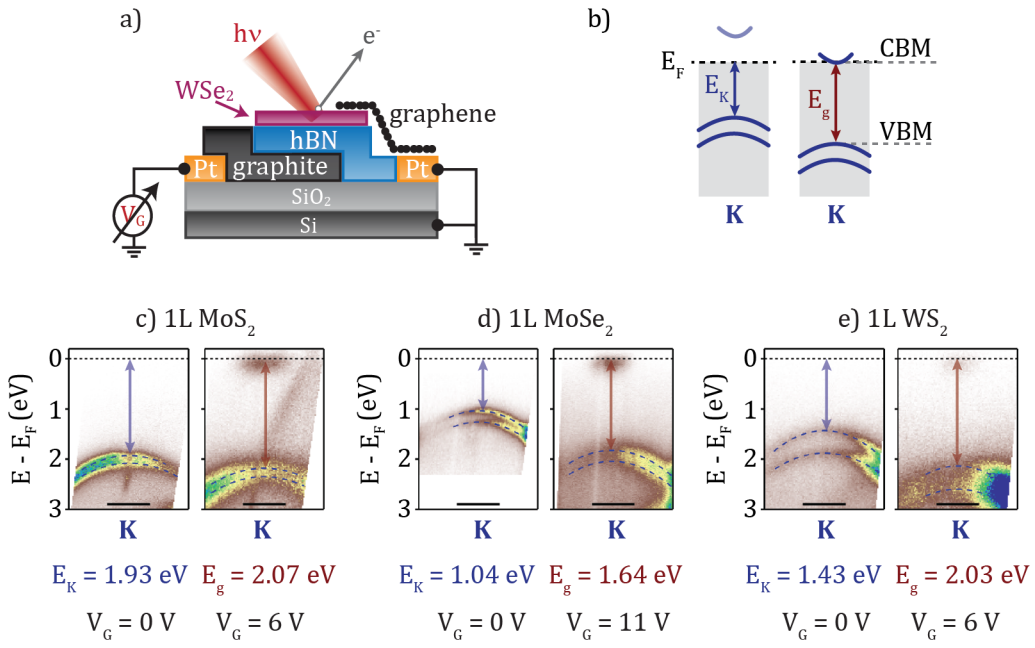

Figure 4.6: a) Device schematic where the graphene contact is grounded and the gate voltage is applied to the graphite back-gate. b) Schematic of the bands near **K** at zero gate voltage, and at a gate voltage high enough to bring the Fermi level to the conduction band edge. (c)-(e) Energy-momentum slices through **K** for ML MoS_2, $MoSe_2$, and WS_2 respectively. Scale bars are $0.3\,\text{Å}^{-1}$.

band edge, g_{2D}, is

$$g_{2D} = \frac{g_s g_\nu m^*}{\hbar^2} \tag{4.5}$$

where g_s and g_ν are spin and valley degeneracy respectively, and m^* is the effective mass. For ML WSe_2, $g_\nu = 2$ as the conduction band minima are at the inequivalent **K** points. The dispersion of the conduction band is not measurable with the ARPES here, so we use a DFT calculated effective mass of $m^* \approx 0.3m_e$ and a conduction band spin-splitting of $\approx 40\,\text{meV}$ [141]. The band is therefore spin-polarised giving $g_s = 1$. The carrier concentration is given by

$$n_G = \int_{E_C}^{\infty} F(E) g_{2D} dE \tag{4.6}$$

The Fermi-Dirac distribution, $F(E)$, is

$$F(E) = \frac{1}{e^{(E-E_F)/k_B T} + 1} \tag{4.7}$$

where k_B is Boltzmann's constant and T is absolute temperature [13].

For the experimental conditions used here ($n_G < 1.0 \times 10^{13}\,\mathrm{cm}^{-2}$ and $k_B T = 9\,\mathrm{meV}$) then $E_F - E_C \lesssim 30\,\mathrm{meV}$. Therefore, E_F was determined by fitting the Fermi edge with a Fermi-Dirac distribution and E_C was calculated from this. However, the difference between them is not resolvable as the dominant error from the spectrometer is greater than 30 meV.

Returning to Table 4.1, with increasing numbers of layers the bandgap decreases and transitions from direct to indirect. The main trends seen are that the bandgap depends more on the chalogen while the SOC depends more on the transition metal which is consistent with predictions made in the literature [141].

4.2.3 Calculating carrier concentration

Electrostatically doping samples in this fashion gives fine control of the carrier concentration. The samples can be compared to a parallel plate capacitor, where an hBN dielectric is sandwiched between a graphite gate and a top graphene contact (or an MX_2 layer and then graphene). As mentioned previously, the capacitance is given by Eq. 4.4 and the gate induced carrier concentration is $n_G = CV$, where the voltage, V, is the sum of all the potentials acting on the sample.

During photoemission, the beam excites electrons out of the sample creating a photocurrent, I_{PE}, and a potential difference, ΔV, between the beam region and the gate or contact. In our samples, this can cause lateral current flow in from the graphene contact, I_C. The beam also generates electron-hole pairs within the hBN dielectric, which acts as a large bandgap semiconductor, producing photoconductivity within the hBN so current can flow from the gate, I_G. The total photoemitted current is the sum of the lateral contribution from the contact, and the vertical current through the hBN, shown top left in Fig. 4.7. This will reduce the effective gate voltage to $V_G - \Delta V$. The gate doping also shifts the chemical potential, $\Delta\mu$, of the sample, as we saw previously with the change in Dirac point energy for graphene. This gives a total sum of the potentials as $V = (V_G - \Delta V - \Delta\mu)$.

The gate induced carrier concentration is then

$$n_G = C_G(V_G - \Delta V - \Delta\mu/e) \tag{4.8}$$

where $\Delta\mu = \Delta(E_F - E_D)$.

For a graphene device, the contact resistance through the graphene sheet is small ($R < \sim 1\,\mathrm{k\Omega}$). Therefore ΔV is negligible ($\Delta V < \sim 2\,\mu\mathrm{V}$) and the current is dominated by I_C. $\Delta\mu$ is given by the change in Dirac point energy i.e. $\Delta\mu = \Delta E_D$, which can be measured directly from the ARPES spectra at each given voltage. This

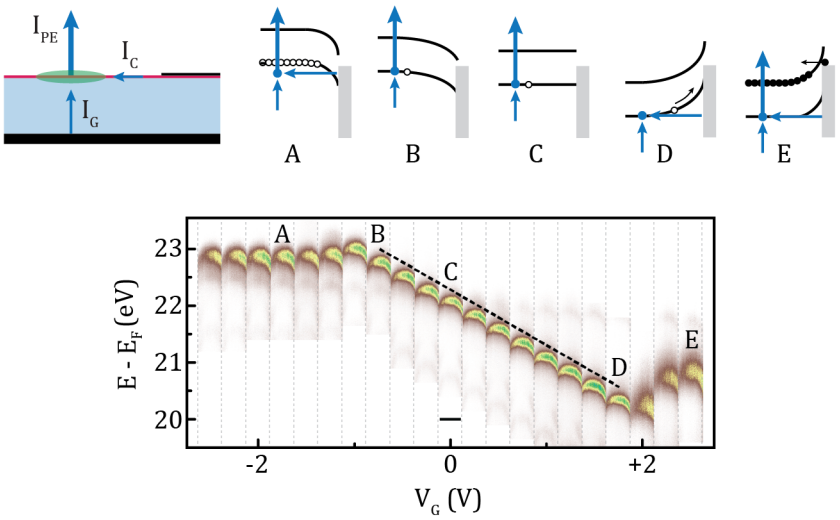

Figure 4.7: Top left shows the photoemission current I_{PE}, current from the graphene contact I_{C}, and current from the gate through the hBN layer I_{G}. The schematics to the right illustrate the band situation at each labelled gate voltage (A-E). The grey rectangle represents E_{F} for the graphene contact, the black lines are the WSe_2 conduction and valence bands, and the arrows indicate when I_{G} and I_{C} are significant. For the bottom graph, each vertical strip is an energy-momentum slice through $\mathbf{\Gamma}$ in ML WSe_2, measured at the gate voltage given. Each slice is $0.6\,\mathrm{\AA}^{-1}$ wide.

is found to be negligible with respect to the gate voltage ($\Delta E_{\mathrm{D}} \leq 0.3\,\mathrm{eV} \ll V_{\mathrm{G}}$). Therefore $n_{\mathrm{G}} \approx C_{\mathrm{G}} V_{\mathrm{G}}$ to within a $< 10\%$ accuracy. This relationship was used to convert the graphene gate voltages in Fig. 4.1. The accuracy in n_{G} is dominated by the accuracy of d_{BN} measured using AFM, typically of order $(10.0 \pm 0.5)\,\mathrm{nm}$, and uses $\epsilon_{\mathrm{BN}} = 4.5$ from literature [16, 165].

For samples with an MX_2 layer, the situation is more complicated as the in-plane resistance varies with voltage. Studying the shift in energy of the band in the MX_2 layer as the gate voltage is varied helps to understand the relevant potentials and currents. Fig. 4.7 shows the changing location of $E_{\mathbf{\Gamma}}$ as a function of V_{G} for a WSe_2 device. The graph shows vertical strips of energy-momentum slices taken through $\mathbf{\Gamma}$ as a function of V_{G}. The top row of schematics show the band diagrams and current flows at the corresponding gate voltages.

Between B and D, the bands track linearly with gate voltage. For small gate voltages the chemical potential is within the WSe_2 bandgap thus the in-plane resistance is high and I_{G} dominates. At A and E, the bands are stationary and independent of gate voltage. This indicates that the MX_2 has become conductive. At E and above, a threshold voltage is exceeded and the electrons begin to populate the conduction band within WSe_2. Electrons flow in from the graphene contact,

increasing I_C, and the conduction band becomes pinned near the graphene Fermi level. At A, the same occurs as holes accumulate in the valence band and pin the band edge to the gate Fermi level. There is an overshoot at the transitions near D and B as there is a Schottky barrier between WSe_2 and graphene contact which must be overcome.

From the slices shown in Fig. 4.7, there is no increase in band width at $\mathbf{\Gamma}$ between B and D. This is while the WSe_2 is insulating and therefore the band shifts uniformly under an applied gate potential. At A and E the bands broaden considerably, likely due to the inhomogeneous electric potential in the WSe_2 across the beam spot resulting from the lateral current flow.

For small gate voltages, when the electrochemical potential is within the MX_2 bandgap, the in-plane resistance is high and ΔV becomes substantial. For larger gate voltages, once the chemical potential reaches either the conduction or valence bands, the shifts in $\Delta\mu$ are negligible due to the Fermi level pinning. Therefore the $\Delta V - \Delta\mu$ term in Eq. 4.8 can be measured directly from the electrostatic shift in a WSe_2 band feature, such as the band at $E_{\mathbf{\Gamma}}$, i.e. $\Delta V - \Delta\mu = \Delta E_{\mathbf{\Gamma}}$. Then Eq. 4.8 becomes

$$n_G = C_G(V_G - \Delta E_{\mathbf{\Gamma}}/e). \tag{4.9}$$

Fig. 4.8 a) shows $\Delta E_{\mathbf{\Gamma}}$ change linearly with gate voltage for small V_G. This is emphasised by plotting $V_G - \Delta E_{\mathbf{\Gamma}}$ in Fig. 4.8 b) and the flat trend around zero. Within this region, the WSe_2 bands are rigidly shifted with V_G as the photoconductivity generated in the hBN allows the potential of the ML layer to be kept close to that of the gate, and no charge accumulates in the WSe_2.

For larger gate voltages, $\gtrsim 2\,\mathrm{V}$, $V_G - \Delta E_{\mathbf{\Gamma}}/e$ becomes more linear with V_G. This is expected behaviour for doping sufficiently to populate the conduction band and confirms the Fermi energy no longer changes as it is pinned to the bottom edge of the conduction band due to its large DOS. The converse is true for voltages $\lesssim -1\,\mathrm{V}$, where the Fermi level is pinned to the valence band edge.

Fig. 4.8 c) shows the current measured though the device as a function of V_G. This is explained in more detail in Chapter 6. But briefly, in the central region, the photocurrent increases as the field across the hBN layer increases with V_G as the beam is close to the graphene - if the beam was further away, we would not expect any current. More importantly, the increase in photocurrent at the threshold voltages (the shaded regions) is consistent with the MX_2 becoming conducting.

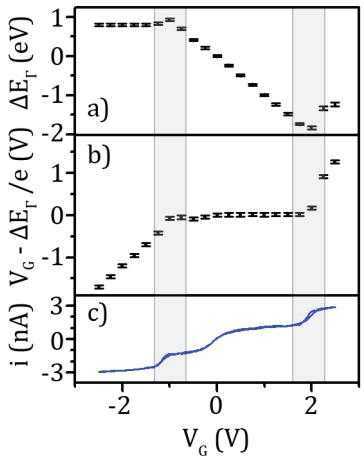

Figure 4.8: a) $\Delta E_{\mathbf{\Gamma}}$ vs V_{G} for ML WSe_2. b) $V_{\mathrm{G}} - \Delta E_{\mathbf{\Gamma}}/e$ vs V_{G}. c) Current from gate to ground vs V_{G}. The grey shaded regions indicate the threshold regions in which the WSe_2 becomes conducting.

4.2.4 Doping dependence on electronic structure

This technique with fine control of the gate voltage enables the study of band structure as a function of carrier concentration. Fig. 4.9 a) shows a **Γ** - **K** slice of ML WSe_2, taken at increasing carrier concentrations. The conduction band becomes visible at **K** for $n_{\mathrm{G}} \gtrsim 1 \times 10^{12}\,\mathrm{cm}^{-2}$. Above $n_{\mathrm{G}} \gtrsim 1 \times 10^{13}\,\mathrm{cm}^{-2}$ the second conduction band minimum becomes visible at **Q**. This confirms that the two conduction band minima are very close together, within $\approx 30\,\mathrm{meV}$ of each other, as discussed in Section 4.2.3. It also confirms that **K** is lower as it appears first and independently of **Q**, i.e. ML WSe_2 has a direct bandgap which is consistent with theory [141].

The rigid structure of the valence band, such as $E_{\mathbf{\Gamma K}}$, does not change significantly with increasing carriers, as we saw in Section 4.2.2. However, the valence band rises and $E_{\mathbf{K}}$ increases while the conduction band remains pinned at E_{F}, as shown in Fig. 4.9 a). As such, the measured bandgap decreases with increasing carrier concentration. This is indicative of bandgap renormalisation, where the bandgap decreases due to free carrier screening [140, 168, 169].

As we have used the same sample design for our ARPES samples which is used for optical spectroscopy, we can compare the same sample across techniques. The inset in Fig. 4.9 b) shows the photoluminescence data taken from the same sample as Fig. 4.9 a). Comparing the values from both help us understand the change in bandgap.

The solid black circles in Fig. 4.9 b) are the bandgap measurements from the

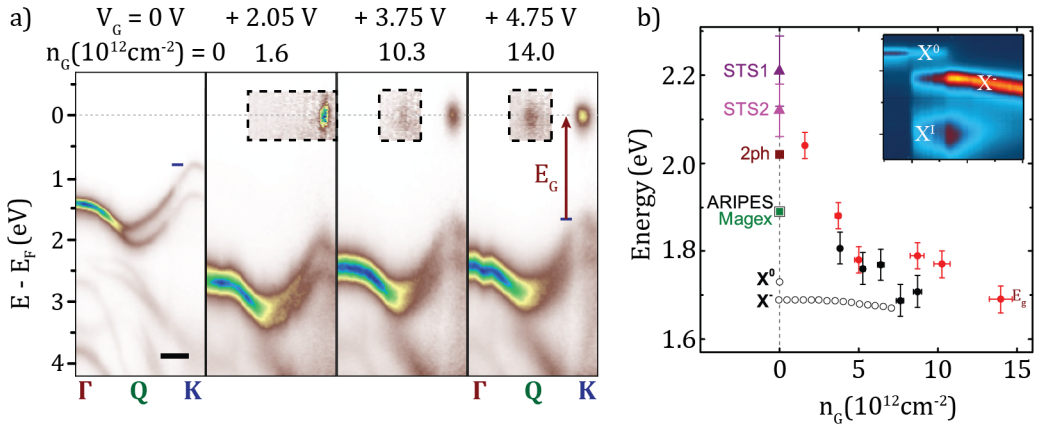

Figure 4.9: a) Energy-momentum slices from **Γ** - **K** for ML WSe_2 at given V_G (and therefore n_G). Scale bar is 0.3 $Å^{-1}$. The intensity in the dotted box is multiplied by 20 at 2.05 V, and by 40 for higher voltages. b) Band gap dependence on n_G. Red and black solid circles are for devices measured with gated ARPES. Black open circles are photoluminescence peak positions for the neutral exciton (X^0) and negative trion (X^-) of the same device as the black circles. The inset shows the photoluminescence data. The points at $n_G = 0$ are measurements of the bandgap from other techniques in the literature: STS1 [157] (purple triangle) and STS2 [158] (pink triangle) are from STS measurements, ML WSe_2 on graphite at $T = 4.5$ K and 77 K respectively; 2ph (brown square) is from two-photon absorption [159], on SiO_2 at 300 K; ARIPES (black open square) is from inverse photoemission [160], on sapphire at 300 K; and Magex (green solid square) is from magneto-optical measurements [161], encapsulated in hBN at 4 K.

device shown on the left. The empty black circles are the photoluminescence peak positions for neutral (X^0) and charged (X_-) excitons obtained from ML WSe_2 as a function of gate doping at 100 K. The values of E_g from a separate device are also shown as red solid circles and agree within the uncertainty. The results show that E_g decreases systematically by ≈ 400 meV as n_G rises to around 10^{13} cm^{-2}. This behaviour resembles band renormalisation previously reported for ML $MoSe_2$ [140].

Band renormalisation appears to be an important consideration when measuring bandgaps in 2D materials. The effect of dielectric environment on bandgap has previously been measured. Ryon *et al.* reported that the calculated bandgap for MoS_2 changes by up to 0.9 eV depending the dielectric environment due to environmental dielectric screening, though experiments show less than this [170]. Raja *et al.* report direct measurements which support that the dielectric environment controls both the bandgap and the exciton binding energy of 2D materials (WS_2 and WSe_2) by several 100's of meV.

Here, we report that the gate induced carrier concentration can change the bandgap by almost 0.5 eV. While gate induced band renormalisation is not new,

compared to typical 3D semiconductors which have reported bandgap changes of order a few meV, this large renormalisation for 2D samples is perhaps surprising [140]. However, it reflects the increased free carrier screening within MLs and could account for the discrepancies in measured bandgaps across techniques as each technique accesses different ranges of carrier concentrations.

Fig. 4.9 b) also includes bandgap measurements for $n_G = 0$. These are inferred from STS [157, 158], two-photon absorption [159], inverse photoemission [160], and magneto-optic [161] studies. By extrapolating back from the photoemission data towards $n_G = 0$, the bandgaps are reasonably consistent with each other. The smaller values of E_g reported in MLs highly doped with alkali metals (down to 1.4 eV for ML WSe_2) are consistent with extrapolating this renormalisation process to higher n_G [168].

4.3 Conclusions

To our knowledge, these are the first reported direct *in operando* ARPES measurements. They reveal new details about the band structure and bandgaps of 2D ML materials; including graphene, WSe_2, $MoSe_2$, MoS_2, WS_2. Through direct observation, our work confirms that the conduction band minima is at **K** for these MX_2 materials, as predicted [141]. For WSe_2, the second conduction band minima was also observed at **Q** for higher carrier concentrations. The layer dependent electronic structure of WSe_2 has been observed, as it progresses from direct to indirect bandgap with increasing layers. The technique has also enabled the study of gate dependent effects such as bandgap renormalisation and the subsequent decrease in bandgap for increased carrier concentration.

The ability to measure changes in the electronic bands in field-effect devices opens up many possibilities. For example, in multi-layer 2D HS devices it could be used to study the perpendicular electric-field dependence of the bands (which will be discussed in Chapter 5) [102, 171], including band inversion and possible topological phase transitions [172]. It could potentially be used to investigate the doping dependence in superconductors, charge-density-wave materials, and excitonic insulators. It could be used to study moiré effects in similar 2D samples, including magic-angle twisted bilayer graphene [173, 174]. This technique has great potential for expansion, with the addition of circularly polarized light or a spin-resolved spectrometer [66], and could be extended to study more complex 2D systems.

TMD	$\Delta_{\mathbf{SOC}}$ (eV)	$E_{\mathbf{K}}$ ($V_{\mathrm{G}} = 0$) (eV)	$E_{\mathbf{\Gamma K}}$ ($V_{\mathrm{G}} = 0$) (eV)	$m^*_{\mathbf{K}}/m_e$	$E_{\mathbf{g}}$ (eV)	$n_{\mathbf{G}}$ (cm^{-2})	T (K)
1L MoS_2	0.17 ± 0.04	1.93 ± 0.02	0.14 ± 0.04	0.7 ± 0.1	2.07 ± 0.05	12.0 ± 0.8	105
1L $MoSe_2$	0.22 ± 0.03	1.04 ± 0.02	0.48 ± 0.03	0.5 ± 0.1	1.64 ± 0.05	10.4 ± 0.7	105
1L WS_2	0.45 ± 0.03	1.43 ± 0.02	0.39 ± 0.02	0.5 ± 0.1	2.03 ± 0.05	9.4 ± 0.6	105
1L WSe_2	0.49 ± 0.01	0.80 ± 0.01	0.62 ± 0.01	0.42 ± 0.05	1.79 ± 0.03	8.7 ± 0.4	100
2L WSe_2	0.50 ± 0.01	0.75 ± 0.01	0.14 ± 0.01	0.41 ± 0.05	1.51 ± 0.03	7.1 ± 0.5	100
3L WSe_2	0.50 ± 0.01	0.74 ± 0.01	0.00 ± 0.01	0.40 ± 0.05	1.46 ± 0.03	8.7 ± 0.4	100

Table 4.1: Measured band parameters of MX_2 semiconductors. Δ_{SOC} is the spin-orbit coupling of the valance band at $\mathbf{K}$; $E_{\mathbf{K}}$ the valence band energy at $\mathbf{K}$ at $V_{\mathrm{G}} = 0$; $E_{\mathbf{\Gamma K}}$ is the difference in energy for the valence band at $\mathbf{K}$ and $\mathbf{\Gamma}$ at $V_{\mathrm{G}} = 0$; $m^*_{\mathbf{K}}$ is the effective mass of the valence band edge at $\mathbf{K}$ (measured in the $\mathbf{\Gamma}$ — $\mathbf{K}$ direction using data within $0.1\,\mathrm{\AA}^{-1}$ of $\mathbf{K}$) in units of the free electron mass m_e; E_{g} is the bandgap; n_{G} is the gate induced carrier density and T is the stage temperature. All samples were on a hBN substrate with no graphene cap.

Chapter 5

Band shifts across graphene-MX_2 heterostructures with gating

5.1 Introduction

The previous chapter studied the effect on band structure of controlling carrier concentration of ML materials. Electric fields can also be used to control band structure by changing band alignments and enables band engineering within van der Waals heterostructures [8, 64].

Many potential applications of 2D HS rely on the application of an electric field across the sample and the associated field dependent effects. Better understanding of field dependent band parameters such as band offsets, band alignments across layers and band behaviours could lead to better device engineering [59, 175, 176].

In 2D electronics, graphene can be used to make an ohmic contact to the 2D semiconductors due to field effect tuning of the work function [61]. The Fermi level in graphene can change significantly for small changes in carrier concentration, due to its low DOS. This gate tuneability makes it attractive as a contact electrode in van der Waals HS. The Schottky barrier height can be minimised due to the field effect tuning [49], which gives more efficient charge injection to TMDs for example. As with controlling carrier concentration for 2D TMD HSs, an electric field can be applied using a back-gate geometry [53]. For example, vertical field effect transistors have used it in functioning devices like g/hBN/gr or gr/MoS_2/metal [59, 139, 175, 177]. The barrier height can be determined from the band alignments, hence it is

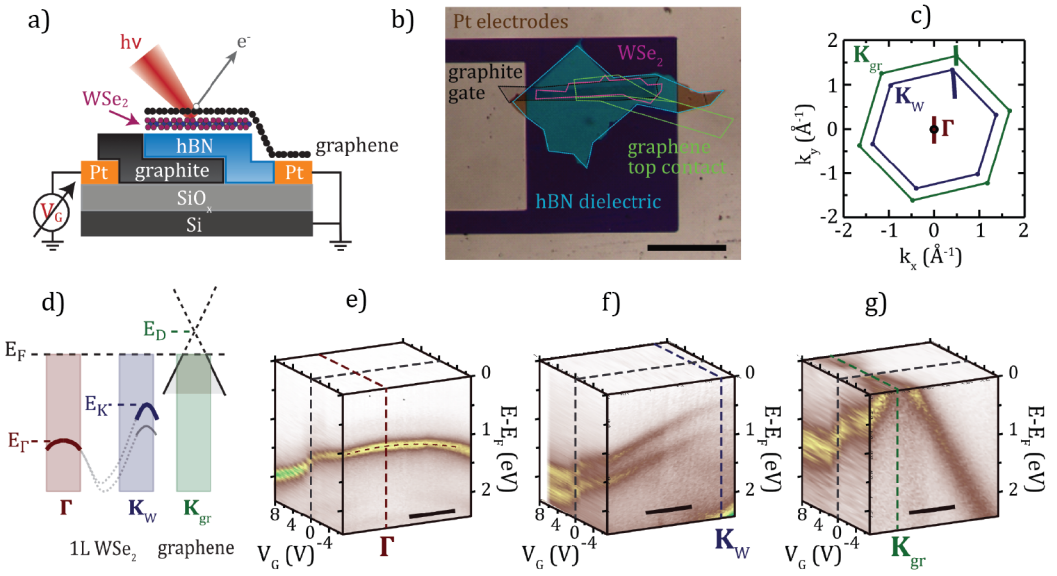

Figure 5.1: a) Schematic and b) optical microscope image of the gated WSe_2 sample, with labels and outlines showing each relevant flake. Scale bar 20 µm. c) Plot in reciprocal space of the first BZs of WSe_2 (blue hexagon) and graphene (green hexagon), with the positions of the energy-momentum slices marked as solid lines. d) Energy-momentum schematic of band energies. Photoemission intensity as a function of energy, momentum, and gate voltage, I(E, $\mathbf{k}_{||}$, V_G), around e) $\mathbf{\Gamma}$, f) $\mathbf{K}$ point of WSe_2 and g) $\mathbf{K}$ point of graphene. Scale bars are 0.3 $Å^{-1}$.

important to understand how the band alignments change with electric field.

Scanning probe studies such as STM and STS have been used to study the gate-dependence of back-gated 2D HS in order to indirectly infer bandgaps and VB offsets [49, 139]. We have shown that *in situ* gated µ-ARPES can be used to directly measure the band structure of back-gated TMD HSs. This technique can also be used to quantify the effect of electric field on the band alignments.

This chapter will discuss using *in operando* spatially resolved ARPES to study the effect of electric field on back-gated MX_2 HS with graphene top contacts and study changes in the band alignments and offsets with electric field.

5.2 Results and discussion

5.2.1 Field dependent effects across back-gated WSe_2

ARPES was performed on a graphene encapsulated ML WSe_2 gated HS. Fig. 5.1 a) is a schematic of the sample and Fig. 5.1 b) shows an optical micrograph with outlines of electrodes and flakes. The sample was prepared in the same manner as

previous chapters, outlined in Chapter 2.

With the beam stationary on the HS, energy-momentum spectra were acquired as a function of gate voltage. As ARPES is sensitive to the top few layers of a material it was possible to image the WSe_2 bands through the graphene encapsulation layer. For each voltage, the analyser was positioned to image the high symmetry points of the WSe_2 flake and the graphene. The three points of interest here are: the BZ centre, $\mathbf{\Gamma}$, the corner of the first BZ of WSe_2, $\mathbf{K}_{\mathrm{W}}$, and the Dirac point at the corner of the first BZ of graphene, $\mathbf{K}_{\mathrm{gr}}$. Fig. 5.1 c) shows the reciprocal space plot of the first BZs of WSe_2 and graphene. It also includes the momentum coordinates, (k_x, k_y), and orientation of the slices taken at each symmetry point. Fig. 5.1 d) shows a relative band energy schematic of $\mathbf{\Gamma}$, $\mathbf{K}_{\mathrm{W}}$ and $\mathbf{K}_{\mathrm{gr}}$ with respect to E_{F}, as discussed in Chapter 4. Fig. 5.1 e) - g) show the measured photoemission as a function of energy, momentum, and gate voltage, I(E, $\mathbf{k}_{||}$, V), for each symmetry point.

The band energies were extracted from each energy-momentum slice. For $\mathbf{\Gamma}$ and $\mathbf{K}_{\mathrm{W}}$, the bands were fit with a parabolic function to obtain the band maximum energies, $E_{\mathbf{\Gamma}}$ and $E_{\mathbf{K}}$ respectively. For graphene, a linear fit was performed on each side of the canonical graphene Dirac dispersion. The Dirac point energy, E_{D}, was given by the intersection of both lines, the same treatment as Section 4.2.1. All energies are quoted in terms of binding energies. E_{F} was found by fitting a Fermi-Dirac distribution over the photoemission threshold, acquired on the Pt electrode.

The band parameters measured at $V_{\mathrm{G}} = 0\,\mathrm{V}$ are consistent with our previous reports on similar MX_2 samples [88, 127]. The measured VBM at $\mathbf{K}_{\mathrm{W}}$ gives $E_{\mathbf{K}} = (0.85 \pm 0.05)\,\mathrm{eV}$. The band maximum at $\mathbf{\Gamma}$ gives a $\mathbf{\Gamma}$ - $\mathbf{K}$ offset of $E_{\mathbf{K}} - E_{\mathbf{\Gamma}} = (0.55 \pm 0.05)\,\mathrm{eV}$. The spin splitting of WSe_2 valence band at $\mathbf{K}_{\mathrm{W}}$ is measured as $\Delta_{\mathrm{SOC}} = (0.48 \pm 0.03)\,\mathrm{eV}$.

The chemical potential is near the centre of the bandgap for this sample. In Chapter 4, we have shown that ML WSe_2 has a direct bandgap, and for low carrier concentrations the bandgap tends to $E_{\mathrm{g}} = 2.1\,\mathrm{eV}$. Therefore, given the VBM measured here, the chemical potential must be close to the centre of the bandgap. However, it is hard to give an exact energy for the CBM due to increased dielectric screening from the graphene layer on top, which likely reduces the bandgap of WSe_2 due to changes in the dielectric environment [170].

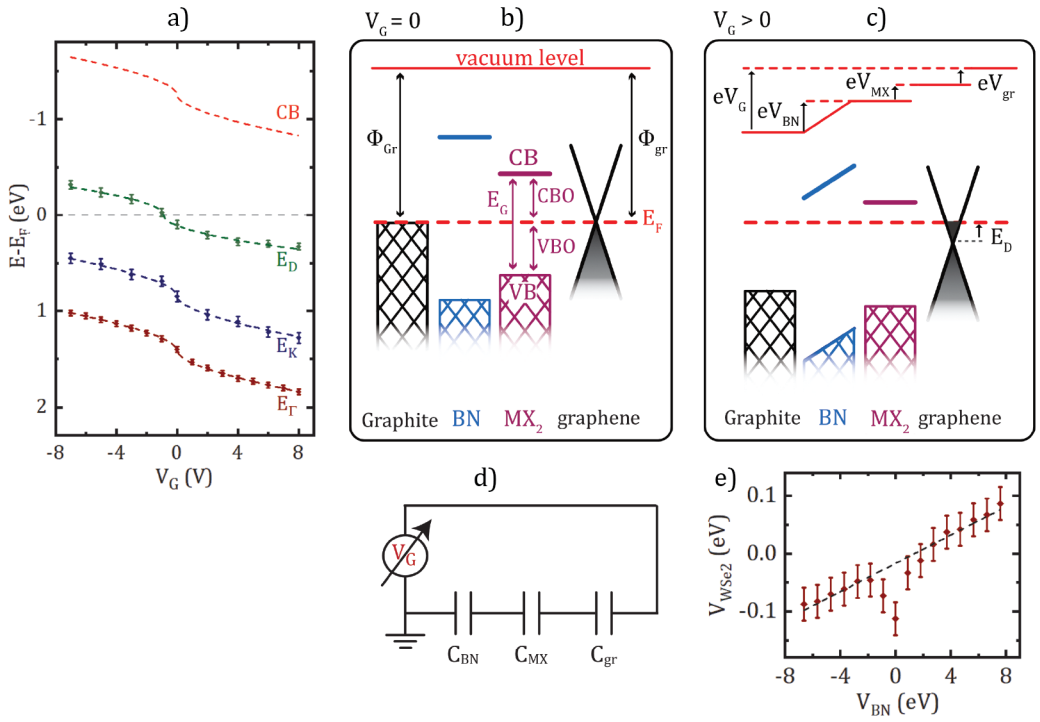

Figure 5.2: a) Band energies as a function of V_{G}, extracted from the data in 5.1 for E_{D} (green), $E_{\mathbf{K}}$ (blue) and $E_{\mathbf{\Gamma}}$ (maroon). Fits to the data are given by dashed lines of the corresponding colour. The red dashed line is the expected position of the CBM, with the assumption that the bandgap for WSe_2 is $E_{\mathrm{g}} = 2.1\,\mathrm{eV}$. Band diagram schematic for b) $V_{\mathrm{G}} = 0\,\mathrm{V}$ and c) $V_{\mathrm{G}} > 0\,\mathrm{V}$. d) Equivalent circuit for the heterostructure. e) Plot of the potential drop across the ML WSe_2 against the potential drop across the hBN dielectric. The dashed line is the linear fit from which the dielectric ratio is obtained.

5.2.2 Modelling capacitances and field dependent band shifts across MX_2 heterostructures

The shift in band maximum of each high symmetry point, $\mathbf{\Gamma}$, $\mathbf{K}_{\mathrm{W}}$ and $\mathbf{K}_{\mathrm{gr}}$, is shown in Fig. 5.2 a). The bands shift as a result of the voltage across the sample creating an electric field through the HS. The WSe_2 valence band appears to shift rigidly within the electric field, as there is no evidence for a change in the $\mathbf{\Gamma}$ - $\mathbf{K}$ alignment (i.e. $E_{\mathbf{K}} - E_{\mathbf{\Gamma}}$ remains constant with changing gate voltages). The graphene band behaves as expected over a gate voltage range of $V_{\mathrm{G}} = -7\,\mathrm{V}$ to $8\,\mathrm{V}$, for a hBN thickness of $d_{\mathrm{BN}} = (25 \pm 1)\,\mathrm{nm}$. The Dirac point shifts by $\Delta E_{\mathrm{D}} = (0.65 \pm 0.04)\,\mathrm{eV}$ as expected for field-effect tuning of graphene, as discussed in Chapter 4 [58, 61]. Over the same gate voltage range, the WSe_2 valence band moves by $\Delta E_{\mathbf{K}} = (0.83 \pm 0.05)\,\mathrm{eV}$. This is significantly greater than the shift seen in graphene alone, indicating more than the change in work function of graphene is causing the band shifts in WSe_2.

Considering a band diagram of the system helps to understand this behaviour. Fig. 5.2 b) shows the static band alignment between the layers of the HS for $V_{\mathrm{G}} = 0\,\mathrm{V}$. In this model, the graphene is undoped and the work function of graphene, Φ_{gr}, is taken to be the same as that of the graphite back-gate, Φ_{Gr}. E_{F} is taken to lie roughly in the middle of the bandgaps of both the hBN and the semiconducting WSe_2, as determined from the ARPES measurements.

Fig 5.2 shows the band alignment for a gate voltage $V_{\mathrm{G}} < 0\,\mathrm{V}$. This results in an electric field across the layers. The voltage causes charge to accumulate in the graphene top layer. The low DOS in graphene means the charge changes the chemical potential with respect to the Dirac point, resulting in the observed shift of E_{D}. This changes the work function and results in a potential drop across graphene, V_{gr}, of

$$V_{\mathrm{gr}} = \frac{\Delta E_{\mathrm{D}}}{e} \tag{5.1}$$

where the change in E_{D} is measured relative to its value at $V_{\mathrm{G}} = 0\,\mathrm{V}$.

There are also potential drops across the MX_2, V_{MX}, and hBN, V_{hBN}. From Kirchhoff's second law, the sum of all the potential drops must equal the gate voltage. This gives that

$$V_{\mathrm{gr}} + V_{\mathrm{MX}} + V_{\mathrm{BN}} = V_{\mathrm{G}} \tag{5.2}$$

where V_{gr} is defined above, and the remaining potentials can be read off directly from the band dispersions and the measured band shifts. V_{MX} is given by the difference between the change in energy of the VBM of the MX_2 band (i.e. the change in $E_{\mathbf{K}}$), and the change in energy of the Dirac point (i.e. the change in E_{D}). This gives

$$V_{\mathrm{MX}} = \frac{\Delta E_{\mathbf{K}} - \Delta E_{\mathrm{D}}}{e}. \tag{5.3}$$

V_{hBN} is found by combining Eqs. 5.2 and 5.3 to give

$$V_{\mathrm{BN}} = \frac{V_{\mathrm{G}} - \Delta E_{\mathbf{K}}}{e}. \tag{5.4}$$

In order to form a quantitative model for the system, we begin by assuming clean interfaces with no charge traps or mid-gap states. The MX_2 layer and hBN can be treated as separate, ideal dielectrics and it is assumed that the chemical potential is far from any band edges (i.e. CBM$>>k_{\mathrm{B}}T$ and VBM$>>k_{\mathrm{B}}T$). Applying Gauss's law over the HS layers, and further assuming no free charges, gives an equivalent circuit (shown in Fig. 5.2) of three capacitors in series: C_{BN}, C_{MX}, and C_{gr}. C_{BN} is the geometric areal capacitance of a parallel plate capacitor with the hBN layer

as the dielectric, given by

$$C_{\mathrm{BN}} = \frac{\epsilon_0 \epsilon_r^{\mathrm{BN}}}{e d^{\mathrm{BN}}} \tag{5.5}$$

where ϵ_0 is the permittivity of free space, ϵ_r^{BN} is the relative permittivity or dielectric constant of hBN, e is the elementary charge and d^{BN} is the thickness of the hBN layer. Similarly, C_{MX} is the geometric areal capacitance of the MX_2 layer in a parallel plate capacitor, given by

$$C_{\mathrm{MX}} = \frac{\epsilon_0 \epsilon_r^{\mathrm{MX}}}{e d^{\mathrm{MX}}} \tag{5.6}$$

where ϵ_r^{MX} is the relative permittivity or dielectric constant of the MX_2 and d^{MX} is the thickness of the layer.

For graphene, the capacitance is treated as the quantum capacitance of graphene, a property of 2D systems with low DOSs, which is a capacitance in addition to, and different from, the classical areal capacitance. The additional capacitance originates from the band filling and emptying with additional charge carriers. For low DOSs, such as graphene, this change can be considerable and is seen clearly by the change in Dirac point energy. The change in chemical potential is equivalent to a change in voltage. This imitates a capacitor in parallel to the classical geometric capacitance, which is known as the quantum capacitance [13, 178, 179]. The quantum capacitance of graphene, C_{gr}, is of the form

$$C_{\mathrm{gr}} = \frac{4e^2}{a^2\sqrt{3}\pi(\hbar v_{\mathrm{F}})^2}|E_{\mathrm{F}} - E_{\mathrm{D}}| = \frac{4e^2}{a^2\sqrt{3}\hbar v_{\mathrm{F}}\sqrt{\pi}}\sqrt{n} \tag{5.7}$$

where $a = 2.46\,\text{Å}$ is the lattice spacing, $\hbar$ is reduced Plank's constant and v_{F} is the Fermi velocity.

The dashed lines in Fig. 5.2 a) are fits to data based on this three capacitor model. Graphene has been fit in the same manner as described in Chapter 4. The valence bands of WSe_2 have been fit using graphene's fitting parameters and then an additional linear term on top. These fits agree well with the data, indicating that the model is valid for describing this data and sample set up.

The potential drops across each material can help us understand the band alignments between each layer. From the equivalent circuit, we can treat them as capacitors in series, and the charge remains constant across the circuit. If we consider the ratio of potential drops across the hBN and MX_2 with Eqs. 5.5 and 5.6, then

$$\frac{V_{\mathrm{MX}}}{V_{\mathrm{BN}}} = \frac{C_{\mathrm{BN}}}{C_{\mathrm{MX}}} = \frac{\epsilon_r^{\mathrm{BN}}}{\epsilon_r^{\mathrm{MX}}}\frac{d^{\mathrm{MX}}}{d^{\mathrm{BN}}}. \tag{5.8}$$

By considering this ratio of potential drops, this give a ratio of capacitances and therefore of dielectric constants.

Fig 5.2 e) is a plot of the potential drops across hBN and WSe_2, as defined in Eqs. 5.4 and 5.3 respectively. There is a clear linear dependence as expected, excluding the two points around zero. The linear fit shown was performed excluding these two points. The gradient of the fit gives the ratio of dielectric constants from Eq. 5.8. Using $d^{\mathrm{BN}} = (25 \pm 1)\,\mathrm{nm}$ and $d^{\mathrm{WSe_2}} = (0.7 \pm 0.1)\,\mathrm{nm}$, then $\epsilon_r^{\mathrm{WSe_2}} = (2.1 \pm 0.4)\ \epsilon_r^{\mathrm{BN}}$. Using $\epsilon_r^{\mathrm{BN}} = 4.5$ from our previous work [127], then $\epsilon_r^{\mathrm{WSe_2}} = (9.6 \pm 1.7)$. This is close to values reported by other studies, although our value is slightly larger than the one reported in the study by Kim *et al.* where $\epsilon_r^{\mathrm{WSe_2}} = (7.2 \pm 0.3)$ [180]. However, their study only looked at thin layers and extrapolated back to ML which could account for the differences.

The band offset between WSe_2 and graphene gives the barrier height for charge injection from the graphene. A low barrier height can indicate that graphene is an efficient contact electrode for electron or hole conduction, with the height of barrier given by either the CBM or VBM respectively. The change in CBM (or VBM) is given by the sum of V_{gr} (which varies with $\sqrt{V_{\mathrm{G}}}$) and V_{MX} (which varies linearly with V_{G}). At low V_{G}, changes in V_{gr} dominate. At higher V_{G}, V_{gr} is comparable to V_{MX}. Both are limited by the dielectric break down field of the dielectric, independent of the thickness of the dielectric, which for hBN is $E^{\mathrm{BN}} \approx 0.7\,\mathrm{V nm^{-1}}$. By taking this value and assuming graphene is undoped at $V_{\mathrm{G}} = 0\,\mathrm{V}$, then over the full gate range the bands shifts by almost 1 eV as a result of the change in work function of graphene and an additional $\sim 0.5\,\mathrm{eV}$ as a result of the field across the WSe_2. These results agree with predictions of Schottky barrier heights in back-gated MoS_2 [53].

The two points around zero which deviate from the linear dependence indicate limitations to this simple model. Defects and contamination could cause additional charge in the MX_2 or at the interfaces. These measurements were performed at low temperature (100 K) in UHV, after a long anneal to reduce surface adsorbates and contaminants. This also reduces interlayer contamination from the fabrication, as trapped contaminants will tend to bind together and move out from the under the layers [181]. However, the anomalous points around zero gate voltage indicate some excess charge or defects are still present. For the range around zero of $\sim$2 V, this would equate to an additional charge concentration of almost $2 \times 10^{12}\,\mathrm{cm^{-2}}$.

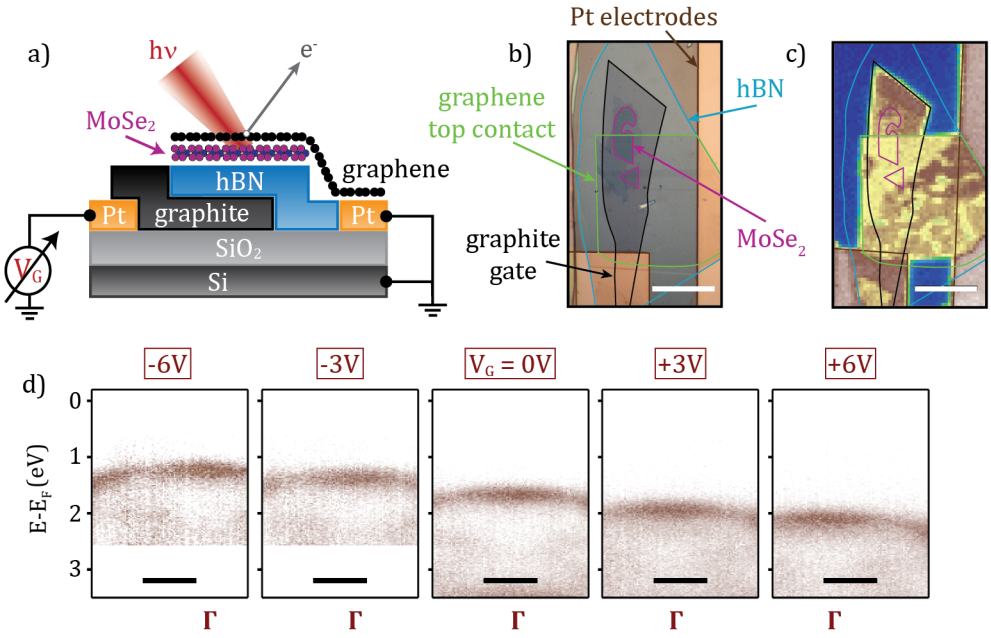

Figure 5.3: a) Schematic and b) optical microscope image of a back-gated $MoSe_2$ sample, with labels and outlines showing each relevant flake. c) SPEM map of the sample region shown in b). Flake outlines help identify locations. Scale bars for b) and c) are 20 µm. d) Energy-momentum slices taken of the valence band of encapsulated $MoSe_2$, taken at **Γ** (i.e. around the BZ centre) as a function of gate voltage, V_G. Scale bars are 0.2 $Å^{-1}$.

5.2.3 Field dependent effects across back-gated $MoSe_2$

Greater evidence for additional trapped charge and defects is seen on a similar $MoSe_2$ sample. Fig 5.3 a) shows a schematic and b) optical micrograph of a $MoSe_2$ HS fabricated in the same manner as the previous sample. The stacking order is the same, with ML $MoSe_2$ replacing the WSe_2. Fig. 5.3 c) shows a SPEM image with the relevant flakes outlined. Fig. 5.3 d) shows energy-momentum spectra taken on the HS at a range of gate voltages, from −6 V to 6 V. The slices show the $MoSe_2$ valence band at **Γ** and shows the band moving with gate voltage as expected.

Fig 5.4 a) shows the measured band shifts for $MoSe_2$ as a function of gate voltage. The shift in graphene Dirac point energy is measured and fit using the same method as the previous sample. For the $MoSe_2$ band, spectra were only acquired and fit from the valence band at **Γ**. The photoemission from the valence band at **K** was too weak to measure. This was due to a combination of lower sample quality (seen clearly by the increased background in Fig. 5.3 d)) and the lower photoemission cross-section of $MoSe_2$ at $\mathbf{K}_W$, described in Chapter 2. The WSe_2 shows that **Γ** - **K** alignment does not change significantly with gate voltage. Therefore, $E_{\mathbf{K}}$ was

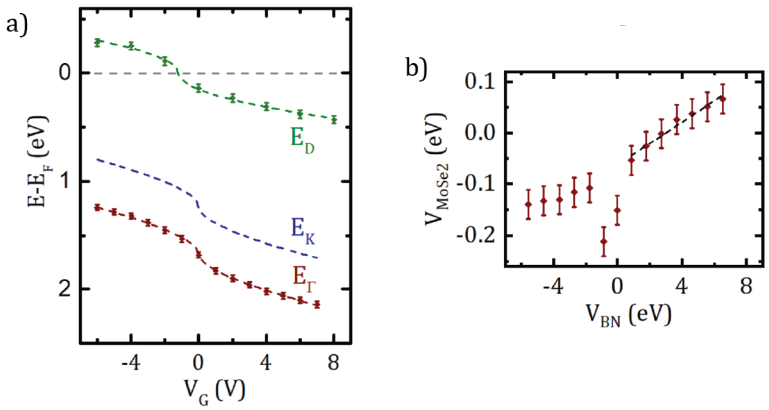

Figure 5.4: a) Band energies as a function of V_{G} extracted from the sample in 5.3 for E_{D} (green), $E_{\mathbf{K}}$ (blue) and $E_{\mathbf{\Gamma}}$ (maroon). Fits to the data are given by dashed lines. b) Plot of the potential drop across the ML $MoSe_2$ against the potential drop across the hBN dielectric. The dashed line is the linear fit from which the dielectric ratio is obtained.

calculated from $E_{\mathbf{\Gamma}}$ using $E_{\mathbf{K}} - E_{\mathbf{\Gamma}} = (0.44 \pm 0.03)\,\mathrm{eV}$, measured on previous samples [88]. The band shifts for this sample are qualitatively similar to those of the WSe_2 sample shown in Fig. 5.2.

The VBM for $MoSe_2$ is much higher than WSe_2, $E_{\mathbf{\Gamma}} = (1.24 \pm 0.04)\,\mathrm{eV}$ at $V_{\mathrm{G}} = 0\,\mathrm{V}$. Both materials have a similar bandgap so the higher VBM indicates initial n-doping of the $MoSe_2$. This is more clearly shown by the plot of $V_{\mathrm{MoSe_2}}$ against V_{BN} in Fig. 5.4 b), which demonstrates a larger deviation from the linear model around zero. The plot is only linear at positive gate voltage, which has been fit to find the ratio of dielectric constants as before. For $d^{\mathrm{BN}} = (19.0 \pm 0.5)\,\mathrm{nm}$ and $d^{\mathrm{MoSe_2}} = (0.7 \pm 0.1)\,\mathrm{nm}$, then $\epsilon_r^{\mathrm{MoSe_2}} = (1.6 \pm 0.4)\,\epsilon_r^{\mathrm{BN}}$ which gives $\epsilon_r^{\mathrm{MoSe_2}} = (9.6 \pm 1.7)$. We see the same deviation around zero as Fig. 5.2. For negative voltage it appears that $V_{\mathrm{MoSe_2}}$ remains roughly constant and independent of V_{BN}. This would be consistent with Fermi-level pinning within $MoSe_2$ from mid-gap or defect states [139, 182, 183]. Others have reported that $MoSe_2$ is more prone to defects than WSe_2 [18], which would also help explain these differences.

5.3 Conclusions

We have shown that *in situ* gated ARPES can be used to isolate the field dependent effects from carrier concentration effects by probing through a graphene top layer.

The gate dependent band shifts across layers of the HS can be described

using a simple three capacitor model. This indicates the semiconducting MX_2 layer acts as dielectric in series with the hBN and graphene's quantum capacitance. Using this fact, important material properties have been calculated, including the dielectric constants of both WSe_2 and $MoSe_2$, as well as estimates for Schottky barrier heights. We have shown that WSe_2 typically has fewer defects and lower contamination than $MoSe_2$, as seen by different VBMs. We have also seen evidence for Fermi-level pinning within $MoSe_2$, despite the same fabrication process used for both samples. This is consistent with other reports of Fermi-level pinning in MoS_2 and shows the simple model requires further work to be fully comprehensive.

In situ gated ARPES is viable for use on several samples, and many more materials could be studied with the technique. It can provide insight into the behaviour of field effect encapsulated HS devices, and changes in carrier concentration of exposed samples. Gathering this information helps improve our understanding of graphene as an effective contact for these MX_2 materials and devices.

Chapter 6

Photoemission current during ARPES with *in situ* gating

6.1 Introduction

The previous chapters have illustrated that *in situ* electrostatic gating during μ-ARPES is a powerful technique for studying 2D materials and devices. It has been used to study the fundamental physics at work within 2D materials including gated electronic structure, carrier concentration dependent effects and field dependent effects. The results obtained from this technique have the potential to be used in the future for effective sample design and operation.

It is important to understand how the technique employed effects the results in order to carefully analyse the data. Insight can be gained by measuring the current flow through the HS and the changes induced by the high energy and high fluence photon beam. This has components due to photoconductivity of the different layers within the HS and due to photoemission.

Scanning with the high energy photon beam is, in essence, similar to scanning photocurrent microscopy (SPCM), a scanning probe technique which generates photocurrent by optical excitation with a laser to generate a spatial photocurrent map. SPCM can be used to determine carrier diffusion lengths, recombination lifetimes and doping concentrations [184]. It has been used on semiconductor nanostructures [185] and nanowires [186] to determine electronic properties. In recent years, the technique had also been used to study vertical MoS_2 heterostructures where Yu *et al.* showed the photocurrent generation can be controlled with external electric fields [175]. Another study by Britnell *et al.* has also used the technique to study flexible WS_2 heterostructures to study potential transistor behaviours [64].

The same descriptions used to describe SPCM can be applied to our HS samples in ARPES in order to understand the I-V characteristics and photocurrent generation. This chapter will focus on the origin and description of photocurrent, in order to better understand gated ARPES heterostructure results and progress the technique as a powerful analytical tool.

6.2 Results and discussion

6.2.1 Quantifying photocurrent from ARPES measurements

Fig. 6.1 shows a typical sample studied at Diamond Light Source, nanoARPES I05 beamline. The sample was prepared using mechanical fabrication onto a SiO_2 substrate and glued onto a standard 8-leg DIP chip carrier. The chip carrier was then slotted into a custom-made alumina holder with electrical contacts between the chip carrier's legs and the pins at the bottom of the UHV plate, shown in Fig. 6.1 a). These pins, once situated in vacuum, allow gating of the sample during measurement within the I05 analysis chamber as outlined in Section 2.4.2.

Optical images of the mechanically exfoliated sample are shown in Fig. 6.1 b). The larger image shows the sample region, located near the top right of the image, with metal contact legs drawing away from the sample and a large electrode surrounding the top and sides. The inset is a zoomed out image showing the contact legs extending to the contact pads which are wire bonded to the chip carrier frame.

Fig. 6.1 c) shows the sample region with outlines for each material: metal contacts (light grey), gate graphite (white), hBN (green), ML WS_2 (purple) and graphene (black). There is also ML hBN towards the bottom third, used to cover the graphene and bottom contacts, but this is not relevant to this discussion, and thus has been omitted. A schematic of the sample is given in Fig. 6.1 d) showing the vertical layers, the contacts and direction of the photon beam used for ARPES measurements. The gate voltage, V_G, is applied to the back-gate (BG), with the top contact (TC) completing the circuit.

Fig. 6.1 e) is a SPEM map of the same region as Fig. 6.1 c) with $V_G = 0\,V$. Each pixel is the total photoemission intensity as measured by the detector at a point, integrated in both energy and angular ranges. From this we can identify different regions based on emission intensity, as described in previous chapters.

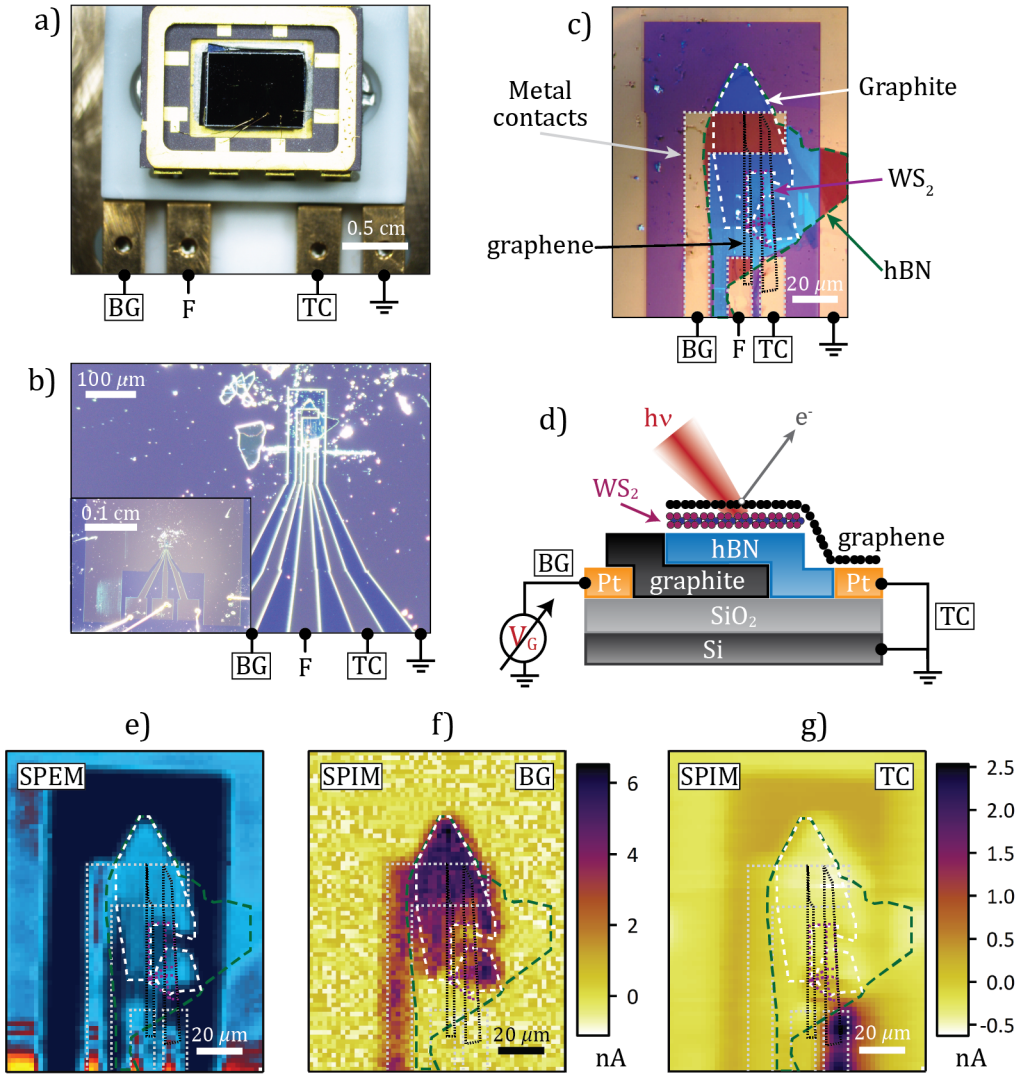

Figure 6.1: a) Image of the silicon chip glued on the 8 leg chip carrier, held with an alumina holder on a UHV plate for Diamond I05 beamline. b) Large optical images of the sample region, with metal contacts visible. c) Optical of just the sample region. Outlines of the metal contacts (grey), graphite gate (white), hBN (green), WS_2 (purple) and graphene (black). Contact legs go to the back-gate (BG), top contact (TC) or are floating (F) or grounded as labelled. d) Schematic of the sample. e) SPEM map of the sample region with flake outlines. f) SPIM map of the sample, measured through the BG and g) the TC.

Photocurrent from ungated samples

As the beam scans across the sample, the photoexcitation process emits photoelectrons [111]. This induces a current flow to replace the photoelectrons, which is measured as the photocurrent. The photocurrent is measured using a

current pre-amplifier connected to the contact pins to measure the current through the sample which, as Fig. 6.1 f) and g) show, is of order nA. For I05 at Diamond light source, a DDPCA-300 Sub Femto Ampere Current Amplifier is used to measure the current whilst at SPECTROMICROSCOPY at Elettra, a Keithley 487 Picoammeter is used. This measured photocurrent is the total integrated photoemission from the sample, for all allowed photoemission energies and momenta. This is comparable to the integrated intensity of a photoemission survey scan, commonly used in XPS studies [111].

The measured photocurrent is dependent on a number of factors, such as: beam energy (increases with beam energy) [114], beam flux (increases with flux) [108], and the material's electronic structure. For example, materials with strong core levels will have a much higher photocurrent than a material with only valence bands being probed when the photon energy exceeds the binding energy of the core levels.

This allows a new, simple method of mapping a sample in ARPES which is not normally used. By measuring the photocurrent during a scan we can construct an image of the sample very quickly, a technique we have called scanning photocurrent microscopy (SPIM). Fig. 6.1 f) and g) are SPIM maps of the sample, with $V_G = 0\,V$. A SPIM map is analogous to a SPEM map, where each pixel represents a integrated intensity. In a SPIM map, each pixel represents the measured sample photocurrent, i.e. the integrated photoemission from the sample across all energy and momenta, whilst a SPEM map is from the limited angular and energy range of the analyser's detector. Note that there are other potential contributions to the measured SPIM current, as discussed later in this chapter. During imaging, the energy and flux of the beam are constant and therefore variations of the measured photocurrent originate from changes in the material being probed. Consequently, the contrast in a SPIM map can be used to identify different sample regions, giving an easily acquired imaging mode.

Fig. 6.1 f) is a measurement of the photocurrent through the graphite back-gate. An increase in current is measured over the back-gate electrode and the graphene back-gate flake due to photoconductivity of the hBN as discussed in Section 6.2.2. Other contrast changes, for the other flakes, are much smaller in magnitude as the flakes are not directly connected and therefore no current is measured through the back-gate electrode.

Fig. 6.1 g) is a measurement of the photocurrent through the graphene top gate. In this SPIM map, the contrast between large metal contact and SiO_2 substrate is visible. The samples flakes are also outlined due to changes in photoemission

intensity. The biggest current is measured through the top gate contact, as this is connected directly to the ammeter.

The SPEM and both SPIM maps can be recorded concurrently and can be used to effectively identify sample location. The SPIM maps can also be used to give information of material properties and can be used to understand the effect that gating can have on photocurrent.

6.2.2 Photocurrent from gated graphene

To better understand the I-V characteristics of the sample with an applied electric field, the first region to consider is gated graphene where a hBN dielectric is sandwiched between the graphene top contact and the graphite back-gate. Regardless of gate voltage, a photoemission induced photocurrent, J_{ph}, is measured on graphene connected to the contact electrode. In addition to the photoelectron emission, the photon beam also induces electron-hole pair generation within the hBN layer, which acts as a large bandgap semiconductor. This results in beam induced photoconductivity of the hBN which, under an applied electric field, results in an increase of measured photocurrent.

In order to understand changes in photocurrent with gate voltage, we begin with developing a simple model of carrier generation and movement to describe the photocurrent measured through the graphene encapsulated hBN.

Modelling photocurrent through hBN

The high energy photon beam used during ARPES causes electron-hole pair generation within the hBN. The carriers will drift, diffuse and recombine within the semiconductor at a rate determined by the material properties (i.e. carrier mobilities and lifetimes), the applied gate voltage, and the dielectric environment. If the carriers recombine before reaching an electrode then no current will be measured. This is the case shown in Fig. 6.2 a) for $V_{\mathrm{G}} = 0\,\mathrm{V}$. If the carriers reach the electrodes before recombination, from a greater drift or diffusion length due to an applied electric field, then a photocurrent will be measured. This is the case shown in Fig. 6.2 b) for $V_{\mathrm{G}} \neq 0\,\mathrm{V}$.

As is typical for describing bulk semiconductors, we begin with the continuity equation

$$\frac{1}{e}\frac{\partial \rho}{\partial t} = G - R - \frac{1}{e}\vec{\nabla} \cdot \vec{J} \tag{6.1}$$

where e is electric charge, ρ is carrier concentration, G is generation rate, R is recombination rate and $\vec{J}$ is current density [185, 187]. The total current density is

given by

$$\vec{J} = \vec{J_n} + \vec{J_p} \tag{6.2}$$

where n and p denote the electron and hole contributions respectively. Each individual current component is given by

$$\vec{J_n} = ne\mu_n\vec{E} - eD_n\vec{\nabla}n \tag{6.3a}$$

and

$$\vec{J_p} = pe\mu_p\vec{E} - eD_p\vec{\nabla}p \tag{6.3b}$$

where n and p denote the respective charge concentrations, μ_n and μ_p are the respective carrier mobilities, D_n and D_p are the respective carrier diffusion coefficients.

In order to obtain a relation for current, first we need to obtain the carrier concentration profile through the hBN layer. We will begin with one carrier, n, and then extend it to p. To simplify the problem, we shall assume the diffusion, mobility and lifetime of the electrons and holes are the same, i.e.

$$\mu_n = \mu_p = \mu \tag{6.4}$$

$$\tau_n = \tau_p = \tau \tag{6.5}$$

$$D_n = D_p = D \tag{6.6}$$

where τ is carrier lifetime. We also assume the net generation rate is equal for both carriers, and constant throughout the hBN i.e.

$$G = g_n = g_p = g. \tag{6.7}$$

This net generation is the photon absorption rate minus the constant loss from photoemission. We shall also assume the recombination rate is the same and given by

$$R = -\frac{n}{\tau} = -\frac{p}{\tau}. \tag{6.8}$$

Beginning with a single carrier, n, in the 1-dimensional (1D) case where x is vertical through the hBN. In steady state, where $\frac{\partial n}{\partial t} = 0$, substituting in Eqs. 6.3a, 6.7 and 6.8 changes the continuity equation to

$$0 = g - \frac{n}{\tau} + D\frac{\partial^2 n}{\partial x^2} + \mu E\frac{\partial n}{\partial x} + \mu n\frac{\partial E}{\partial x} \tag{6.9}$$

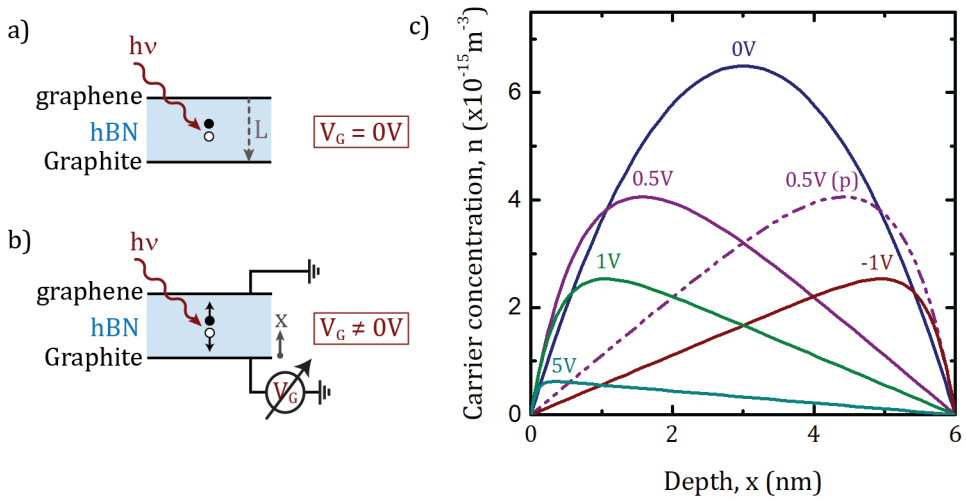

Figure 6.2: a) Pair generation within hBN for $V_G = 0\,V$. HBN thickness is given by L. b) Pair generation and drift under applied gate voltage. c) Typical carrier concentrations across the HS, for n, at positive and negative gate voltages. A single p value is shown in dashed pink.

where E is the applied electric field in the x-direction, given by

$$E = \frac{V_G}{L}. \tag{6.10}$$

V_G is the gate voltage and L is the thickness of the hBN layer. Assuming the electric field is constant throughout the hBN for a given gate voltage, Eq. 6.9 becomes

$$D\frac{\partial^2 n}{\partial x^2} + \mu E\frac{\partial n}{\partial x} - \frac{n}{\tau} + g = 0. \tag{6.11}$$

In order to solve this inhomogeneous second order differential equation we must consider the boundary conditions of our system. At the boundaries with graphene and graphite, the chemical potential will lie in the bandgap of hBN. Therefore the equilibrium carrier concentration in the hBN at the interfaces is effectively zero. We assume that there is little-to-no barrier to the transfer of out-of-equilibrium photoexcited electrons (holes) from the conduction band (valence band) in the hBN to the graphene or graphite. As a result there would be no charge accumulation at the interface and any charge carriers generated in the hBN layer next to the interfaces would transfer directly to the contacts. So, under these assumptions and to a good approximation, we expect the boundary condition of zero carrier concentration to describe our experimental data.

By applying the boundary conditions that the carrier concentration is zero

at each electrode, i.e. $n(x=0)=0$ and $n(x=L)=0$, the solution to Eq. 6.11 is

$$n(x) = g\tau\frac{1-e^{\lambda_2 L}}{e^{\lambda_2 L}-e^{\lambda_1 L}}e^{\lambda_1 x} - g\tau\frac{1-e^{\lambda_1 L}}{e^{\lambda_2 L}-e^{\lambda_1 L}}e^{\lambda_2 x} + g\tau \tag{6.12}$$

where

$$\lambda_1 = \frac{-L_{dr}+\sqrt{L_{dr}^2+4L_D^2}}{2L_D^2} \tag{6.13}$$

$$\lambda_2 = \frac{-L_{dr}-\sqrt{L_{dr}^2+4L_D^2}}{2L_D^2} \tag{6.14}$$

and drift length, L_{dr}, and diffusion length, L_D, are given by

$$L_{dr} = \mu\tau E \tag{6.15}$$

$$L_D = \sqrt{D\tau} \tag{6.16}$$

[188]. The same analysis can be done for p carriers and results in

$$p(x) = g\tau\frac{1-e^{-\lambda_2 L}}{e^{-\lambda_2 L}-e^{-\lambda_1 L}}e^{-\lambda_1 x} - g\tau\frac{1-e^{-\lambda_1 L}}{e^{-\lambda_2 L}-e^{-\lambda_1 L}}e^{-\lambda_2 x} + g\tau \tag{6.17}$$

Fig. 6.2 c) shows the carrier concentration for n and p through the depth of the hBN, for different voltages. This is plotted with $L = 6\,\text{nm}$ and material properties determined by the fit of a sample dataset, shown later in Fig. 6.4. The graph shows that the carriers shift towards the electrodes as V, and therefore E, increases. The greater the voltage, the greater the shift. For negative voltage, the carriers drift towards the opposite electrode. It also shows the difference in behaviour of n and p carriers for the same voltage, 0.5 V, and shows that they drift in opposite directions, as expected.

From Eqs. 6.3a and 6.3b, the current is given by

$$\vec{J_n} = -eDg\tau\frac{\lambda_2(1-e^{\lambda_1 L})(1+e^{\lambda_2 L}) - \lambda_1(1-e^{\lambda_2 L})(1+e^{\lambda_1 L})}{e^{\lambda_2 L}-e^{\lambda_1 L}} \tag{6.18a}$$

and

$$\vec{J_p} = eDg\tau\frac{\lambda_2(1-e^{-\lambda_1 L})(1+e^{-\lambda_2 L}) + \lambda_1(1-e^{-\lambda_2 L})(1+e^{-\lambda_1 L})}{e^{-\lambda_2 L}-e^{-\lambda_1 L}} \tag{6.18b}$$

This gives a total current, from Eq. 6.2, that depends on electric field, sample thickness, and carrier mobility coefficients [188].

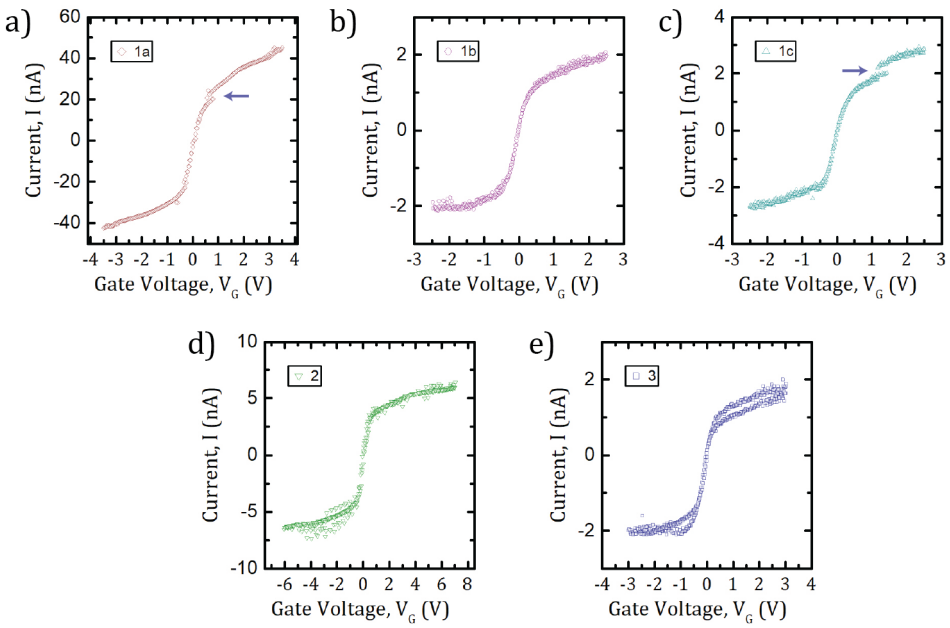

Figure 6.3: Measured photocurrent as a function of gate voltage a) with 74 eV beam energy. The rest are at 27 eV beam energy, with 1, 2 and 3 denoting different samples. e) Scaled photocurrent of all locations and samples as a function of electric field. Small jumps in data are shown with blue arrows.

Fig. 6.3 shows $I-V$ measurements for multiple samples at different sample locations, beam energy and hBN thickness's. It illustrates that the current can vary greatly with beam energy, and the voltages vary due to thickness and generation rate. There are also small, unidentified jumps at positive gate voltages in some datasets, highlighted with the blue arrows in Fig 6.3 a) and c). There is some hysteresis visible in a few of the line profiles, and the gradients change.

Fig 6.4 shows the measured photocurrent, scaled in order to compare the different samples directly. The voltage has been divided by L to convert to electric field and the current of each has been scaled by dividing by the measured current at $E = 0.3\,\mathrm{Vnm}^{-1}$, in order to account for different generation rates. With this scaling, the line profiles now look comparable. The difference between samples can be seen at the turning points, as the lines disperse out as shown in Fig. 6.4.

The data is fit to

$$J = J_n + J_p + mV_\mathrm{G} + J_\mathrm{ph} \tag{6.19}$$

where J_ph is the ungated photocurrent contribution and V_G is an additional linear

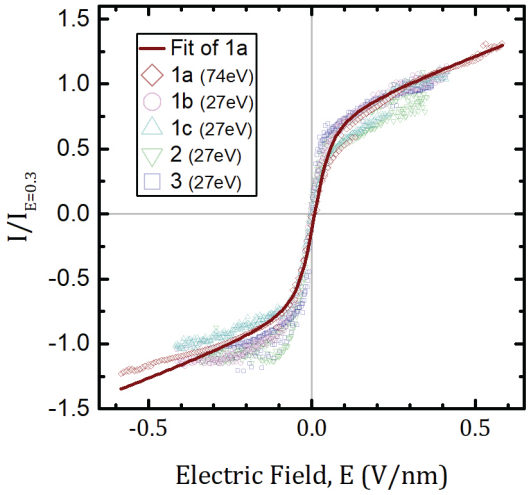

Figure 6.4: Scaled photocurrent measurements with a fit for total current given in the text. 1, 2 and 3 are different samples.

term of gradient m. This improves the quality of fit as it accounts for any potential drops across the sample due to additional resistance in parallel. The fit also gives a slight voltage offset, such that $V = V_{\mathrm{G}} + V_{\mathrm{offset}}$, to account for any in-built electric field within the samples.

For the fit shown in Fig. 6.4 the behaviour looks in good agreement with all of the profiles. It gives a small voltage offset, $V_{\mathrm{offset}} = (-80 \pm 5)\,\mathrm{mV}$, which is in agreement with gating results in Chapter 4. The fit gives a value for the carrier mobility lifetime product of hBN, $\mu\tau = (8 \pm 1) \times 10^{-10}\,\mathrm{m^2V^{-1}}$. This is a value typically used for quantifying semiconductors, used as a metric for carrier transport as well as detector and photovoltaic efficiency [189, 190]. Other studies have reported carrier mobility lifetime value for hBN between $5.4 \times 10^{-10}\,\mathrm{m^2V^{-1}}$ [190] to $5 \times 10^{-12}\,\mathrm{m^2V^{-1}}$[191]. Our value is in agreement with these.

However, other studies show that the product is different for n and p carriers in-plane, values of $\mu_n\tau_n = 2.8 \times 10^{-9}\,\mathrm{m^2V^{-1}}$ to $\mu_p\tau_p = 4.85 \times 10^{-10}\,\mathrm{m^2V^{-1}}$ [192]. Our model has assumed they are equal, so this could be the origin for some of the fit issues at the turning points, but it is still a reasonable fit overall.

This model also assumes that the net generation rate is equal for both carrier. However, at large bias the photocurrent due to drift and diffusion is much larger than the current due to photoemission alone which indicates that only a small fraction of the generated carriers are photoemitted. The comparatively small photoemission rate would still leave an asymmetry in electron and hole concentrations, but this has been neglected in order to achieve the model, similarly to the asymmetry in

effective mass and mobility of the electrons and holes.

The model does not account for the hysteresis observed, or the jumps observed at positive voltage, indicated with blue arrows in the figure. These could be due to defects in the material caused by defect bands, issues with the contacts or the difference in n and p carriers. Further measurements would be needed to isolate each factor in future.

This relatively simple model gives a reasonable approximation for $I-V$ behaviour of our samples and helps to describe the origin of photoconductivity in the hBN layer and photocurrent in these samples. We note that this photoconductivity induced photocurrent is much larger than the photoemission and scales with thickness. But when the dielectric thickness is much bigger than the diffusion length, no photoconductivity is induced and the graphene flake on top is isolated from the gate electrode.

6.2.3 Photocurrent from gated MX_2 flakes

Developing our understanding further, it is important to consider how the addition of the MX_2 layer affects photocurrent, and if measuring photocurrent and SPIM mapping can improve our understanding of MX_2 gating and device design.

Photocurrent through semiconducting flakes

The following ARPES measurements of a gated sample were performed at Spectromicroscopy at Elettra, Italy. Fig. 6.5 a) shows a schematic of a BL WSe_2 sample, fabricated in the same manner as before. Instead of using an alumina holder to mount the chip carrier, it was mounted directly onto a UHV chamber plate with wires connecting the chip carrier legs to the pins at the bottom of the UHV plate, as shown in Fig. 6.5 b). The pins were used for gating and measuring the current of the sample during ARPES measurements as outlined in Section 2.4.2.

The optical image in Fig. 6.5 c) shows the exfoliated flakes: graphene (orange) on BL WSe_2 (purple) on hBN (green) on a graphite back-gate (white). The BL WSe_2 is only partially capped with graphene to form the contact. This allows the sample to be gated as shown in the schematic and allows the study of both capped and exposed BL WSe_2 regions.

Fig. 6.5 d), f) and h) show SPEM maps at gate voltages of 5 V, 0 V and -5 V respectively. The corresponding SPIM map of each is shown in Fig. 6.5 e), g) and i). The ungated SPEM map in Fig. 6.5 f) shows a substantial difference in intensity for capped and exposed regions. The whole WSe_2 flake (purple outline)

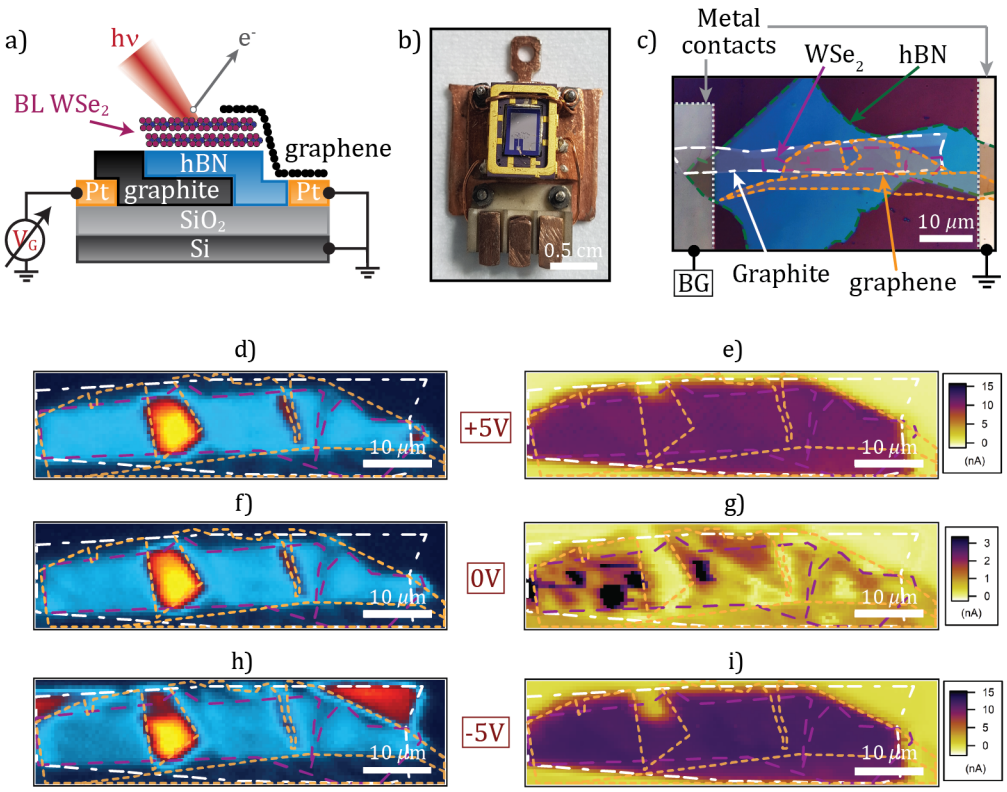

Figure 6.5: a) Schematic of the sample. b) Optical of the sample mounted onto the Elettra UHV plate. c) Optical of the sample region with metal contacts (grey), graphite gate (white), hBN (green), WSe_2 (purple) graphene (orange). d), f) and h) are SPEM maps at 5 V, 0 V and −5 V respectively. e), g) and i) are SPIM maps at 5 V, 0 V and −5 V respectively.

has some photoemission, with a bright yellow region showing the exposed section i.e. the region with no graphene (orange outline) on top. The graphene reduces the photoemission intensity of the WSe_2 flake. It contributes no emission itself, within the angular and kinetic energy range of the detector used for this map. In this case, the detector is aligned to measure the top few eV around the Fermi edge near to $\mathbf{\Gamma}$. Therefore, the valence band of WSe_2 provides intensity but the valence band of graphene is not included. The graphite back-gate (white outline) is not visible in the SPEM map for the same reason.

With a positive gate voltage of 5 V, the SPEM map in Fig. 6.5 d) is not significantly different from 0 V in f). With a negative voltage of −5 V, the SPEM map in Fig. 6.5 h) shows a small change as the back-graphite gate is visible. This is due to the gate bias shifting the graphite bands closer to the Fermi level, such that they are now within the integrated energy window of the detector.

Fig. 6.5 e), g) and i) are the corresponding SPIM maps for 5 V, 0 V and −5 V respectively. The photocurrent measured across the graphene capped region in Fig. 6.5 g) is non zero as there is now beam assisted photoconductivity in the hBN due to carrier generation. The extra WSe_2 layer acts as an additional semiconductor in series with the hBN. Therefore, it is the same as the case discussed in the previous section. From the fitting in Fig 6.4, we note there is a small in-built electric field within the hBN. This causes some carrier transport even at zero gate voltage and results in the small current measured in the capped region of Fig. 6.5 g). The variations in current across the region is likely due to variations in the in-built field, for example due to a build-up of dirt between layers.

For the graphene capped region, the model outlined Section 6.2.2 is sufficient to describe the current behaviour. The graphene regions in Fig. 6.5 e) and i) exhibits a higher current. The gate voltage creates a greater field across the hBN and MX_2 causing more carriers to reach the contacts, resulting in a higher current as expected.

In order to describe the current in the exposed WSe_2 region, consider the data shown in Fig. 6.6. Some of this data is shown previously in Chapter 4 but can now be explained in more detail.

Fig. 6.6 a) show a schematic of the current contributions for the beam on an exposed flake, next to a graphene contact. I_{PE} is the photoemission current leaving the sample. This is replaced by contributions from I_{G} and I_{C}. I_{G} is the current which flows up from the back-gate, through the photoconductive hBN. I_{C} is the current which flows laterally in from the graphene contact to the beam spot.

Fig. 6.6 b) shows data from an exposed ML WSe_2 region on a device measured at Elettra. Fig. 6.6 b) i) shows the shift in position of the WSe_2 VBM measured at $\mathbf{\Gamma}$, measured with respect to the band position at zero gate voltage, i.e. $\Delta E_{\mathbf{\Gamma}}$. Fig. 6.6 b) ii) shows the band shift scaled to gate voltage, i.e. $V_{\mathrm{G}} - \Delta E_{\mathbf{\Gamma}}/e$. Fig. 6.6 b) iii) shows the photocurrent measured through the sample, at a point on the exposed flake next to the graphene contact, as the schematic in Fig. 6.6 a) demonstrates. The grey shaded areas highlight the voltage threshold regions.

At low gate voltages, in between the shaded regions of Fig. 6.6 b) i), the bands shift linearly with gate voltage. The WSe_2 flake is insulating, therefore there are no free carriers for transport within the flake. As such, the resistance to the graphene contact is high and I_{C} is small. Resistance through the hBN is low due to the beam induced photoconductivity within the layer. Therefore, current can flow in easily from the gate and I_{G} dominates. The potential of the flake tracks linearly with that of the back-gate, as the Fermi level is pinned to the gate potential. We see this more clearly in Fig. 6.6 b) ii) which emphasises deviation between the flake

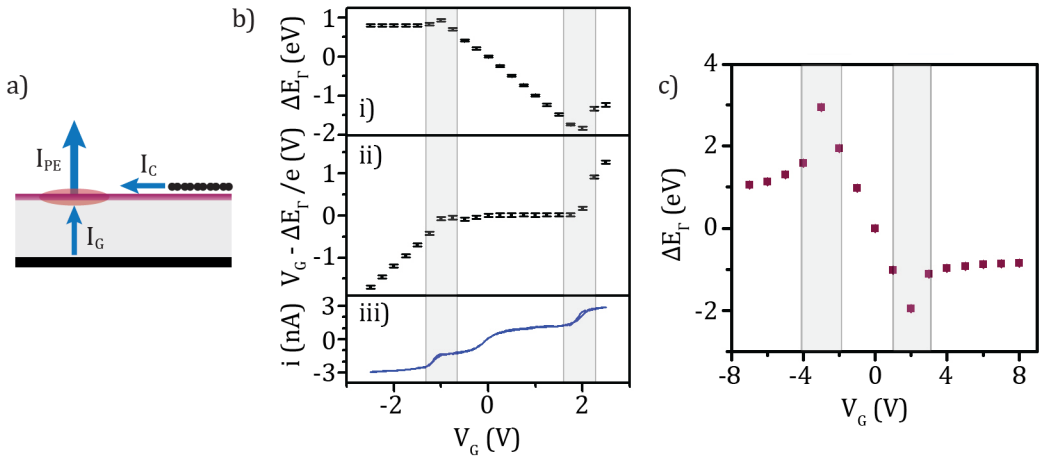

Figure 6.6: a) Schematic of photocurrent from ARPES beam on an exposed MX_2 flake next to a graphene current. The photoemitted current, I_{PE}, is balanced by the gate current, I_G, and the contact current, I_C. b) Data from an exposed WSe_2 ML. i) Shift in band position of VBM at $\mathbf{\Gamma}$, $\Delta E_{\mathbf{\Gamma}}$. ii) $\Delta E_{\mathbf{\Gamma}}$ scaled to gate voltage, V_G iii) measured current through the sample, with beam stationary on the exposed flake next to graphene contact. c) $\Delta E_{\mathbf{\Gamma}}$ for exposed BL WSe_2 from the exposed region in Fig. 6.5.

and gate voltage. Between the threshold regions, there is minimal deviation and the trend is flat.

Following this argument, the current shown in Fig. 6.6 b) iii) should be flat between the threshold regions. However, while the magnitude of current is reduced, we see current behaviour similar to that observed with the beam on graphene, described in Section 6.2.2. This is because the beam spot is situated on the exposed flake close to the graphene contact and the part of the beam spills on to the graphene region also. However, for these measurements it is important to keep the beam as close as possible to the graphene, as shall be discussed later.

At high gate voltages, above the shaded threshold region, the Fermi level has been shifted high enough that the flake has become conductive. Electrons accumulate in the CB and carriers are available in the flake for conduction. The resistance to the graphene contact is low and I_C increases accordingly. As charge can now flow in from the contact, the Fermi level of the flake at the CB is effectively pinned to the Fermi level of the graphene contact. This results in the change in behaviour of $\Delta E_{\mathbf{\Gamma}}$ seen in Fig. 6.6 b) i) and ii), going from a linear gate dependence to almost no gate dependence. The increase in current from I_C can be seen in the threshold region of Fig. 6.6 b) iii) where there is a sharp jump up in current, a sign the flake has become conductive.

The same argument is true for negative voltages greater than the threshold.

Holes accumulate in the VB causing conduction in the flake. The resistance to graphene is lowered and I_C increases, seen as another jump in current in Fig. 6.6 b) iii). In this case, the VB is now effectively pinned to the graphene Fermi level, and we see the same flattening behaviour below the threshold in Fig. 6.6 b) i) and ii).

Within the threshold regions, there is a band overshoot seen in Fig. 6.6 b) i). This is due to a contact resistance between the graphene and the WSe_2. A Schottky barrier between the two prevents the carriers flowing in fast enough to accumulate in the flake, thus generates a slight overshoot until efficient charge flow is achieved.

Fig. 6.6 c) shows the shift in the VBM at $\mathbf{\Gamma}$, $\Delta E_{\mathbf{\Gamma}}$, for the BL WSe_2 sample given in Fig. 6.5. Current was not measured as a function of gate voltage for a single location on the exposed flake. However, similar behaviour is observed for $\Delta E_{\mathbf{\Gamma}}$ in both WSe_2 samples. Therefore, we can justify the same argument for the current flows.

This helps to explain the behaviour seen in the SPIM maps in Fig. 6.5 for the exposed regions. In Fig. 6.5 g) no current is measured in the exposed region as the flake is insulating, and there is no lateral flow from the graphene contact to complete the circuit. In Fig. 6.5 e) and i), the flake has become conductive which allows for current to flow into the flake from the graphene contact as we measured a higher current in these regions. It is worth noting that not all of the exposed flake is conductive at these gate voltages. In Fig. 6.5 i), part of the exposed flake closest to the top, and therefore furthest from the graphene surrounding it, is not fully conductive. Resistance will be lowest closest to the graphene flake, so conduction will spread outwards from graphene with increasing gate voltage. At even higher gate voltages, we would expect the whole exposed region to be conductive. However, we are still limited by the dielectric break down field limit of hBN, as mentioned in Section 6.2.2. As such, this conductive behaviour spreading out from the contact, and being spatially dependent, is an important consideration for designing devices, both for transport measurements and for ARPES measurements.

Understanding gating effects using KFGM

To ensure our understanding of the gate effects without the beam is correct, KFGM was performed on the same sample. KFGM is an extension of AFM which can map the change in surface potential of a sample. An image is created by raster scanning the surface of a sample and mapping each line twice. On the first pass, regular AC AFM is used to map the surface topography, as described in Section 2.3. On the second pass, the tip is lifted a specified height and the line scan is repeated, maintaining the same lift height throughout - this is called nap mode.

During the nap mode, a bias of $V_{\text{tip}} = V_{\text{AC}} \sin(\omega t) + V_{\text{bias}}$ is applied to the tip, creating an electrostatic force between the surface and cantilever. This can be treated as a parallel plate capacitor and thus the energy stored, U, is given by

$$U = \frac{1}{2} C V^2 \tag{6.20}$$

where C is the capacitance and V is the potential difference between tip cantilever and sample [193]. The force, F, is then

$$F = -\frac{\partial U}{\partial z} = -\frac{1}{2}\frac{\partial C}{\partial z} V^2 \tag{6.21}$$

where z is the separation. The potential difference is given by the sum of all the potentials acting on the system, given by

$$V = V_{\text{AC}} \sin(\omega_{\text{AC}} t) + V_{\text{DC}} \tag{6.22}$$

where V_{AC} is the applied AC bias, V_{DC} is the sum of the DC components given by

$$V_{\text{DC}} = V_{\text{bias}} + V_{\text{CPD}}, \tag{6.23}$$

where V_{bias} is the DC part of the voltage applied to the tip and V_{CPD} is the contact potential difference between the tip and sample. This gives

$$V^2 = V_{\text{AC}}^2 \sin^2(\omega_{\text{AC}} t) + V_{\text{DC}}^2 + 2 V_{\text{DC}} V_{\text{AC}} \sin(\omega_{\text{AC}} t) \tag{6.24}$$

$$= (\frac{1}{2} V_{\text{AC}}^2 + V_{\text{DC}}^2) + 2 V_{\text{DC}} V_{\text{AC}} \sin(\omega_{\text{AC}} t) + \frac{1}{2} V_{\text{AC}}^2 \cos(2\omega_{\text{AC}} t). \tag{6.25}$$

The force gradient is then given by

$$\frac{\partial F}{\partial z} = -\frac{1}{2}\frac{\partial^2 C}{\partial z^2} V^2 \tag{6.26}$$

$$= -\frac{1}{2}\frac{\partial^2 C}{\partial z^2}\left(\frac{1}{2} V_{\text{AC}}^2 + V_{\text{DC}}^2\right) \tag{6.27}$$

$$-\frac{1}{2}\frac{\partial^2 C}{\partial z^2}\left(2 V_{\text{DC}} V_{\text{AC}} \sin(\omega_{\text{AC}} t)\right) \tag{6.28}$$

$$-\frac{1}{2}\frac{\partial^2 C}{\partial z^2}\left(\frac{1}{2} V_{\text{AC}}^2 \cos(2\omega_{\text{AC}} t)\right). \tag{6.29}$$

This relation can be separated into three parts: the DC component in Eq. 6.27, the ω_{AC} component in Eq. 6.28 and the $2\omega_{\text{AC}}$ component in Eq. 6.29.

We begin by considering the ω_{AC} component, Eq. 6.28. As we scan an

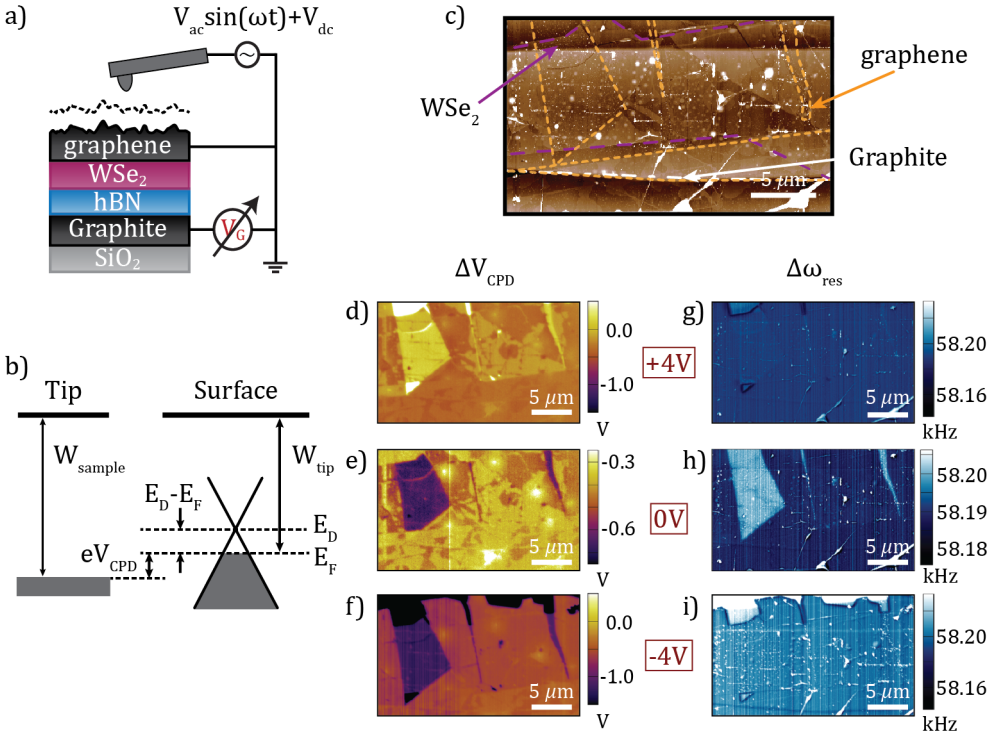

Figure 6.7: a) Schematic of KFGM used for surface mapping, with the AC and DC voltage applied to the tip. b) Energy diagram of the contact potential difference between tip and sample for a graphene surface. c) AFM topography of a WSe_2 heterostructure with graphene (orange), WSe_2 (purple) and graphite (white) outlined. ΔV_{CPD} maps at d) 4 V, e) 0 V and f) −4 V. $\Delta\omega_{\mathrm{res}}$ maps at g) 4 V, h) 0 V and i) −4 V. Scale bar 5 µm.

area, changes in the electrostatic field between tip and sample act to change the resonant frequency of oscillation of the cantilever [194, 195]. This causes a change to the phase response when oscillated at a set frequency, as outline in Eq. 2.28. We employ frequency modulation on the measured phase by using a feedback loop to maintain $\phi = 90°$ by changing the mechanical oscillation frequency, ω_{res}, of the tip and cantilever used for tapping mode [194].

The measured output of ϕ is passed into a lock-in amplifier, which measures the oscillation amplitude of change in ϕ at the frequency of ω_{AC}. The amplitude is then passed into a Kelvin loop which changes V_{bias}, applied to the tip, in order to minimise the amplitude. The amplitude is dependent on the ω_{AC} component of force gradient. If we consider this component, given in Eq. 6.28, then minimising the amplitude minimises the ω_{AC} component and the amplitude is minimised when

$V_{\mathrm{DC}} = 0$. Therefore, from Eq. 6.23, when $V_{\mathrm{DC}} = 0$ then

$$\Delta V_{\mathrm{bias}} = \Delta V_{\mathrm{CPD}}. \tag{6.30}$$

So during KFGM we acquire a map of ΔV_{bias} which relates to changes in the local surface potential of the sample [196, 197].

Now we consider the DC component in Eq. 6.27. Given that V_{DC} has been nulled with the Kelvin loop, and using Eq. 2.32 to relate change in resonant frequency, then the DC component becomes

$$\Delta\omega_{\mathrm{res}} \propto \frac{\partial F}{\partial z} \propto V_{\mathrm{AC}}^2 \frac{\partial^2 C}{\partial z^2}. \tag{6.31}$$

So during KFGM we can acquire a map of the local change in resonant frequency of the cantilever, which relates to the change in sample capacitance [193].

Fig. 6.7 a) is a schematic of KFGM performed on a HS sample. As with ARPES measurements, the gate voltage is applied to the graphite back-gate and the graphene is grounded. The AC and DC voltages are applied to the tip as shown. Fig. 6.7 b) shows how the change in V_{CPD} relates to the change in chemical potential for a graphene surface, thus a map of ΔV_{CPD} is proportional to ΔE_{F} for graphene. Fig. 6.7 c) is a tapping mode AFM topography map of the same sample as Fig. 6.5, with relevant flakes outlined. Both exposed and graphene encapsulated WSe_2 are included in the scan.

Fig. 6.7 d) - f) are ΔV_{CPD} maps of the sample at 4 V, 0 V and −4 V respectively. Much like the SPEM data, there is a contrast change between the graphene capped region and the exposed WSe_2 region at 0 V, as they are at different potentials.

Fig. 6.7 g) - i) are $\Delta\omega_{\mathrm{res}}$ maps of the sample at 4 V, 0 V and −4 V respectively. Fig. 6.7 g) and i) have the same colour scale, while Fig. 6.7 h) has a smaller range. These maps show the change in capacitance with gate voltage. At 0 V, there is a contrast change between the capped and exposed regions. This is because the graphene is conductive, while for the exposed region, the WSe_2 is insulating and acts as a dielectric between the tip and conductive gate underneath. This therefore changes the capacitance and changes the resonant frequency, as outlined in Eq. 6.31. With positive gate, Fig. 6.7 g) shows the change in capacitance between the exposed and capped regions is dramatically reduced, almost non existent. This is explained by the exposed flake becoming conductive, just as the SPIM maps in Fig. 6.5 indicate. The gate has shifted the chemical potential within the WSe_2 to the point where the conduction band begins to fill and the region becomes conductive.

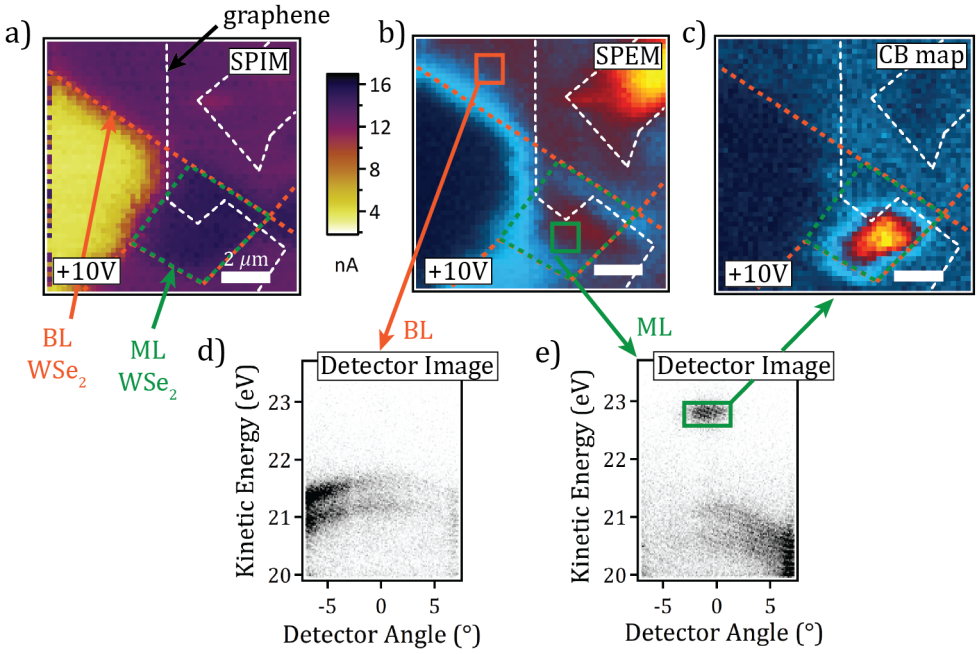

Figure 6.8: a) SPIM map of sample at 10 V with outlines for graphene (white), BL WSe_3 (orange) and ML WSe_2 (green). b) SPEM map for the sample at 10 V, with the analyser oriented to include the **K** point of WSe_2.d) and e) are raw detector images regions of interest highlighted in b) for BL and ML WSe_2 respectively. c) is a conduction band (CB) map for the integrated intensity within the box outlined in e), for each pixel's in d)'s raw detector image. Scale bars are 2 µm.

The same is true for the negative gate voltage, in 6.7 i), where holes have begun to populate the valence band, and the region becomes conductive. The contrast between capped and exposed is therefore also dramatically reduced, due to the sample capacitance changing as the WSe_2 transitions from insulating to conductive.

Identifying conductive regions

KFGM and SPIM show that we expect to see the CBM when the flake is conducting. This happens when there is effective current dissipation through the flake and should therefore occur most easily closest to the graphene flake. SPEM can be used to confirm this by mapping out where the CBM is visible across a sample. Fig. 6.8 shows conduction band mapping for a gated WSe_2 sample. The sample has an exposed ML WSe_2 region, surrounded by BL WSe_2, which is partially capped with graphene. Fig. 6.8 a) is a SPIM map of the sample at $V_G = 10$ V with outlines for each material. This shows that at 10 V the sample is fully conductive in the exposed ML region as the measured current is high. Fig. 6.8 b) is a SPEM

map taken with the analyser focused around the WSe_2 **K** point. Each point has saved the raw detector image, as well as the integrated intensity for the pixel value. Fig. 6.8 d) and e) show the raw detector images (summed over the region of interest boxes in Fig. 6.8 b)) for exposed BL and ML WSe_2 respectively.

For the BL region in Fig. 6.8 d), the WSe_2 spin split bands at **K** are visible. No conduction band is visible here, because BL WSe_2 is an indirect bandgap, and as shown previously in Fig. 6.1, the CBM is at **Q** not **K**. For the ML region in Fig. 6.8 e) the conduction band is visible at **K**, further confirming that region is conductive due to the conduction band being brought below the Fermi level.

Fig. 6.8 c) is a conduction band map. Each pixel value is given by integrating the detector image of each pixel in the SPEM map, within the region of interest box shown in Fig. 6.8 e), and assigning the new integrated intensity as a pixel value. This shows the conduction band is doped across the ML region, with higher intensity closest to the graphene. This is as expected, as closer to the graphene flake current can flow through the flake and allows for charge to dissipate through the MX_2 flake and graphene. This technique can reveal exactly where the conductive regions are and could be used to study edge effects or identify if specific channels are more or less conductive than others.

6.3 Conclusions

This chapter has focused on the practical aspects of interpreting the results of gated ARPES, regarding the origin and description of photocurrent for 2D HSs. We have shown how the current can be measured directly during measurements and how this can be used to identify different regions. This can include determining where a sample is conductive and mapping to find conducting regions. This is particularly useful for locating positions to measure the conduction bands of MX_2 materials and their associated bandgaps.

Measuring the current also helps to explain the behaviour of the sample under the high energy beam and with gating, and SPIM is a useful and efficient technique for ARPES. A simple model can be used to understand the photocurrent within the hBN. It helps us to identify what behaviour is a result of the beam, such as hBN photoconductivity, and what behaviour is a result of the MX_2 materials becoming conductive, such as the increased conduction and increase in current associated with CBM or VBM population. It also illuminates that a thin dielectric minimises the photocurrent, so is better suited for gated measurement of semiconductors.

Combining the results of different techniques, ARPES and KFGM, gives

powerful insight into exactly how these samples are behaving, both with the gate and with the beam, and assists in isolating different behaviours as KFGM allows us to isolate just the gate dependent behaviour separate to beam effects. KFGM reveals that, in order to see and study the conduction band of gated MX_2 samples, we require current dissipation through the flake. This fact is a key consideration for future μ-ARPES device design.

Chapter 7

Conclusion

This work aimed to measure the electronic structure of ML MX_2 materials and HSs. By using *in situ* ARPES to measure back-gated samples, we have been able to directly observe and measure the band behaviour with changing carrier concentration, as well as field dependent effects in 2D van der Waals HSs.

Chapter 3 shows direct band structure measurements of MX_2 exfoliated flakes, including ML WSe_2, WS_2, $MoSe_2$, MoS_2. From these measurements, we have characterised the VB parameters for these materials and observed the layer dependent VB structure of WS_2. ARPES was used to study changes in band structure and hybridisation in HSs and heterobilayers, measuring a number of MX_2/MX_2 HSs. We have used this information to describe and understand the band alignment and interlayer effects, including the requirements for band hybridisation in HSs and formation of commensurate and incommensurate regions in stacked layers. This information on undoped systems provides a platform for understanding the exfoliated flakes and expanding into gated measurements.

In Chapter 4, we demonstrated successful *in situ* ARPES measurements of gated MoWSeS flakes. Incorporating a gate electrode gave control over the carrier concentration within the flake, which can be measured directly with ARPES. Under sufficient gating, the CB is brought below the chemical potential and becomes visible in the measurements. This technique was used to successfully measure the band structure of doped ML, BL and TL WSe_2, where the measurements show the layer dependent transition from direct bandgap in ML to indirect in multilayer. The doping reveals the CBM shifts from the **K** point in ML to the **Q** point in multilayer, and the VBM shifts from the **K** point to **Γ**.

We were able to directly measure the bandgap for ML, BL and TL WSe_2, and ML WS_2, $MoSe_2$, MoS_2. We measured the bandgap as a function of carrier

concentration and observed the bandgap decreasing in ML WSe_2 as carrier concentration increased. This is a sign of bandgap renormalisation, due to extra screening from the increased number of carriers, a potential explanation for the variation in quoted bandgaps across literature.

In Chapter 5 we studied field dependent effects across gated MoWSeS HSs. We used ARPES to measure the gate dependent band shifts across the HS and saw that the bands behave as though the flakes are capacitors in series with each other. We were able to get estimates for dielectric constants of the flakes and saw evidence for Fermi-level pinning in $MoSe_2$. This information is important for future device design and shows how ARPES is effective in probing device physics in 2D HSs.

In Chapter 6 we studied the generation of photocurrent within MX_2 samples during ARPES measurements. The current through the sample during *in situ* gated ARPES measurements was described by a simple model incorporating carrier generation and the photo conductivity induced within hBN which leads to photon assisted tunnelling through the dielectric. From this, we explain why thinner dielectric layers are required for ARPES measurements to allow for dissipation of the photoemitted current, allowing us to map the sample and identify conductive and insulating regions in order to explore the sample behaviour during ARPES. It also provides a convenient and fast imaging mode for ARPES measurements, which we term SPIM. In order to isolate beam effects from gating effects and device operation, we combined ARPES measurements with KFGM. KFGM maps the surface potential and was used to identify conductive and insulating regions of the sample under gating. This revealed the sample geometry required for effective charge injection and dissipation, surrounding a flake with graphene encapsulation.

From understanding the ML electronic structure through to gating effects and effective sample geometries, these results help to develop our understanding of key considerations for effective design of future 2D devices and ARPES measurements to study the fundamental physics of these new materials. Using the knowledge developed here of ML and HS band structure, gating effects, and measurement effects, future studies could probe fundamental physics within other 2D materials and HS.

ARPES could be used to study the electronic structure of other 2D materials, such as charge density wave materials [198] and excitonic insulators [199]. Recent studies have looked at different MX_2 alloys such as $Mo_xW_{(x-1)}S_2$ and $Mo_xW_{(x-1)}Se_2$. These alloys show variation in band gap and SOC due to different contributions from the transition metals d-orbitals. The amount of alloying can be used to vary these quantities and tune the degree of spin or valley polarisation [200–202]. The change

in structure has been seen in bulk crystals and, by using the same sample prep, ARPES could be used to characterise the ML flakes and examine how the band structures change. By combining this with gating, the band engineering from the alloying and the control in carrier concentration from the gate could give greater control over the desired studies.

Spatially-resolved ARPES could be used to study stacking effects in other structures, such as moiré features which can form in layered samples. For example, it could be used to directly measure moiré effects in the band structure of twisted BL graphene, shown to give rise to correlated electronic phases [174]. Similar studies have seen moiré patterns form in other 2D TMD HSs and ARPES could be used to look at periodic variations in band structure and band gaps predicted from theory [203].

Another avenue would be to incorporate gating with polarisation studies of 2D materials. By using different beam polarisations, available at some beamlines such as Diamond Light Source, one could probe the spin and valley physics within these materials. Incorporating this with gating measurements, we could probe the gate dependent valley physics. A recent area of research has started looking at TMD materials for applications in spin and valleytronic devices [26, 204]. The idea for these devices is that the valley and spin indexing is used to transport information. Studies have shown it could be possible to create memory devices from exfoliated TMDs HS [205]. The band alignment within these devices allow for charge collection in order to store memory. *In situ* ARPES would be useful in visualising and directly observing the charge within the devices, in order to better understand them. Combining this with different beam polarisations to utilise the valley-dependent optical selection rules, or even with spin-resolved ARPES [206], could be a very powerful technique to analyse these devices.

Several studies have looked at the excitonic properties of 2D HSs [207], and interlayer valley excitons [129]. ARPES could greatly aid these studies, by directly measuring the band alignment across layers as well as using the gating to probe the CB and relevant bandgaps. In a similar vein, it could be used to study other optoelectronic devices like photodetectors. By measuring the sample current, *in situ* ARPES could be used to measure the gate tuneable photocurrent and band alignment and help develop more efficient photodetectors.

Another natural extension to this work would be to look at fully functioning 2D FET devices. Plenty of studies have focused on TMD FETs and use an almost identical fabrication technique to manufacture them from exfoliated flakes [155]. In order to modify our samples, it would only require a third contact to be included

and a slight modification to stacking sequence. This would then enable us to directly measure FETs during operation, in order to study charge flow, field effects, carrier concentration effects and band alignments. Such studies could improve our understanding of these devices and would prove a powerful diagnostic tool.

A lot of potential applications rely of the ability to make electrical contact to the sample, therefore gated ARPES could study the effectiveness of new 2D contacts [51]. There is still debate over the best contact to use, graphene or other metals, to minimise Schottky barrier height [52]. Also, the most effect contact geometry is still discussed, such as side or top contact [56], aspects which could be probed with *in situ* ARPES.

2D materials have also been used effectively to make a number of sensors as they have a high surface to volume ratio. Some of these devices work due to charge redistribution when exposed to a particular chemical, which then changes transport characteristics [38]. This change in behaviour could be measured using ARPES, as well as measuring the *in situ* band response to exposure.

These studies could be difficult as ARPES requires UHV conditions, though it could be possible to sputter the exposure. It could be easier instead to use KFGM to measure such samples. While it does not give direct band structure information, it is still effective at mapping surface potential and has the added benefits of operating in ambient conductions. It can also measure the relative changes in conductivity across a sample, which would be useful for 2D sensors. KFGM could be used to support a wide range of ARPES studies and could also be used to study the response of devices in ambient conditions without the rigorous requirements of sample preparation for UHV.

In situ gated ARPES has been shown to be a powerful technique for studying 2D materials and HS as it can effectively probe their band structures, band alignments and interlayer effects. It provides a new technique to study fundamental physics and develop our understanding of the key considerations for future 2D device design.

Bibliography

[1] Foundation, N. *The Nobel Prize in Physics* 2010.

[2] Miró, P., Audiffred, M. & Heine, T. An atlas of two-dimensional materials. *Chemical Society Reviews* **43,** 6537–6554. doi:10.1039/c4cs00102h (2014).

[3] Geim, A. K. & Grigorieva, I. V. Van der Waals heterostructures. *Nature* **499,** 419–25. doi:10.1038/nature12385 (2013).

[4] Novoselov, K. S., Mishchenko, A., Carvalho, A. & Castro Neto, A. H. 2D materials and van der Waals heterostructures. *Science* **353,** aac9439. doi:10.1126/science.aac9439 (2016).

[5] Lin, Z. *et al.* 2D materials advances: from large scale synthesis and controlled heterostructures to improved characterization techniques, defects and applications. *2D Materials* **3,** 042001. doi:10.1088/2053-1583/3/4/042001 (2016).

[6] Choi, W. *et al.* Recent development of two-dimensional transition metal dichalcogenides and their applications. *Materials Today* **20,** 116–130. doi:10.1016/j.mattod.2016.10.002 (2017).

[7] Novoselov, K. S. Electric field effect in atomically thin carbon films. *Science* **306,** 666–669. doi:10.1126/science.1102896 (2004).

[8] Castro Neto, A. H. *et al.* The electronic properties of graphene. *Reviews of Modern Physics* **81,** 109–162. doi:10.1103/RevModPhys.81.109 (2009).

[9] Warner, J. H., Schaffel, F., Rummeli, M. & Bachmatiuk, A. *Graphene: fundamentals and emergent applications* (Elsevier, 2013).

[10] Partoens, B. & Peeters, F. M. From graphene to graphite: Electronic structure around the K point. *Physical Review B* **74,** 075404. doi:10.1103/PhysRevB.74.075404 (2006).

[11] Gao, L. *et al.* Face-to-face transfer of wafer-scale graphene films. *Nature* **505,** 190–4. doi:10.1038/nature12763 (2014).

[12] Katsnelson, M. I. Graphene: carbon in two dimensions. *Materials Today* **10,** 20–27. doi:10.1016/S1369-7021(06)71788-6 (2007).

[13] Fang, T., Konar, A., Xing, H. & Jena, D. Carrier statistics and quantum capacitance of graphene sheets and ribbons. *Applied Physics Letters* **91,** 092109. doi:10.1063/1.2776887 (2007).

[14] Roth, S., Matsui, F., Greber, T. & Osterwalder, J. Chemical vapor deposition and characterization of aligned and incommensurate graphene/hexagonal Boron Nitride heterostack on Cu(111). *Nano Letters* **13,** 2668–2675. doi:10.1021/nl400815w (2013).

[15] Batzill, M. The surface science of graphene: Metal interfaces, CVD synthesis, nanoribbons, chemical modifications, and defects. *Surface Science Reports* **67,** 83–115. doi:10.1016/j.surfrep.2011.12.001 (2012).

[16] Dean, C. R. *et al.* Boron nitride substrates for high-quality graphene electronics. *Nature Nanotechnology* **5,** 722–6. doi:10.1038/nnano.2010.172 (2010).

[17] Mayorov, A. S. *et al.* Micrometer-scale ballistic transport in encapsulated graphene at room temperature. *Nano Letters* **11,** 2396–9. doi:10.1021/nl200758b (2011).

[18] Liu, G.-B., Xiao, D., Yao, Y., Xu, X. & Yao, W. Electronic structures and theoretical modelling of two-dimensional group-VIB transition metal dichalcogenides. *Chemical Society Reviews* **44,** 2643–2663. doi:10.1039/C4CS00301B (2015).

[19] Voß, D., Krüger, P., Mazur, A. & Pollmann, J. Atomic and electronic structure of WSe2 from ab initio theory: Bulk crystal and thin film systems. *Physical Review B* **60,** 14311–14317. doi:10.1103/PhysRevB.60.14311 (1999).

[20] Li, M. *et al.* Electronically engineered interface molecular superlattices: STM study of aromatic molecules on graphite. *Physical Review B* **76,** 155438. doi:10.1103/PhysRevB.76.155438 (2007).

[21] Splendiani, A. *et al.* Emerging Photoluminescence in Monolayer MoS2. *Nano Letters* **10,** 1271–1275. doi:10.1021/nl903868w (2010).

[22] Mak, K. F., Lee, C., Hone, J., Shan, J. & Heinz, T. F. Atomically thin MoS2: A new direct-gap semiconductor. *Physical Review Letters* **105,** 136805. doi:10.1103/PhysRevLett.105.136805 (2010).

[23] Xu, X. *Spin and pseudospins in transition metal dichalcogenides* in *2014 IEEE Photonics Society Summer Topical Meeting Series* (IEEE, 2014), 1–2. doi:10.1109/SUM.2014.8.

[24] Mak, K. F., He, K., Shan, J. & Heinz, T. F. Control of valley polarization in monolayer MoS2 by optical helicity. *Nature Nanotechnology* **7,** 494–498. doi:10.1038/nnano.2012.96 (2012).

[25] Cao, T. *et al.* Valley-selective circular dichroism of monolayer molybdenum disulphide. *Nature Communications* **3,** 887. doi:10.1038/ncomms1882 (2012).

[26] Schaibley, J. R. *et al.* Valleytronics in 2D materials. *Nature Reviews Materials* **1,** 16055. doi:10.1038/natrevmats.2016.55 (2016).

[27] Manzeli, S., Ovchinnikov, D., Pasquier, D., Yazyev, O. V. & Kis, A. 2D transition metal dichalcogenides. *Nature Reviews Materials* **2,** 17033. doi:10.1038/natrevmats.2017.33 (2017).

[28] Xiao, D., Liu, G.-B., Feng, W., Xu, X. & Yao, W. Coupled spin and valley physics in monolayers of MoS2 and other group-VI dichalcogenides. *Physical Review Letters* **108,** 196802. doi:10.1103/PhysRevLett.108.196802 (2012).

[29] Roldán, R. *et al.* Electronic properties of single-layer and multilayer transition metal dichalcogenides MX2 (M = Mo, W and X = S, Se). *Annalen der Physik* **526,** 347–357. doi:10.1002/andp.201400128 (2014).

[30] Qian, X., Liu, J., Fu, L. & Li, J. Quantum spin Hall effect in two-dimensional transition metal dichalcogenides. *Science* **346,** 1344–1347. doi:10.1126/science.1256815 (2014).

[31] Wilson, J. & Yoffe, A. The transition metal dichalcogenides discussion and interpretation of the observed optical, electrical and structural properties. *Advances in Physics* **18,** 193–335. doi:10.1080/00018736900101307 (1969).

[32] Constantinescu, G. C. & Hine, N. D. M. Multi-purpose Black-Phosphorus/hBN heterostructures. *Nano Letters* **16,** 2586–2594. doi:10.1021/acs.nanolett.6b00154 (2016).

[33] Wang, Q. H., Kalantar-Zadeh, K., Kis, A., Coleman, J. N. & Strano, M. S. Electronics and optoelectronics of two-dimensional transition metal dichalcogenides. *Nature Nanotechnology* **7,** 699–712. doi:10.1038/nnano.2012.193 (2012).

[34] Saito, Y., Nojima, T. & Iwasa, Y. Highly crystalline 2D superconductors. *Nature Reviews Materials* **2,** 16094. doi:10.1038/natrevmats.2016.94 (2017).

[35] Li, C., Zhou, P. & Zhang, D. W. Devices and applications of van der Waals heterostructures. *Journal of Semiconductors* **38,** 031005. doi:10.1088/1674-4926/38/3/031005 (2017).

[36] Jariwala, D., Sangwan, V. K., Lauhon, L. J., Marks, T. J. & Hersam, M. C. Emerging device applications for semiconducting two-dimensional transition metal dichalcogenides. *ACS Nano* **8,** 1102–1120. doi:10.1021/nn500064s (2014).

[37] Radisavljevic, B., Radenovic, A., Brivio, J., Giacometti, V. & Kis, A. Single-layer MoS2 transistors. *Nature Nanotechnology* **6,** 147–150. doi:10.1038/nnano.2010.279 (2011).

[38] Kolobov, A. V. & Tominaga, J. *Two-Dimensional Transition-Metal Dichalcogenides* doi:10.1007/978-3-319-31450-1 (Springer International Publishing, Cham, 2016).

[39] Duan, X., Wang, C., Pan, A., Yu, R. & Duan, X. Two-dimensional transition metal dichalcogenides as atomically thin semiconductors: opportunities and challenges. *Chemical Society Reviews* **44,** 8859–8876. doi:10.1039/C5CS00507H (2015).

[40] Jiao, L. *et al.* Molecular-beam epitaxy of monolayer MoSe2: growth characteristics and domain boundary formation. *New Journal of Physics* **17,** 053023. doi:10.1088/1367-2630/17/5/053023 (2015).

[41] Xie, L. M. Two-dimensional transition metal dichalcogenide alloys: preparation, characterization and applications. *Nanoscale* **7,** 18392–18401. doi:10.1039/C5NR05712D (2015).

[42] Bogaert, K. *et al.* Diffusion-mediated synthesis of MoS2/WS2 lateral heterostructures. *Nano Letters.* doi:10.1021/acs.nanolett.6b02057 (2016).

[43] Duan, X. *et al.* Lateral epitaxial growth of two-dimensional layered semiconductor heterojunctions. *Nature Nanotechnology* **9,** 1024–1030. doi:10.1038/nnano.2014.222 (2014).

[44] Li, M.-Y., Chen, C.-H., Shi, Y. & Li, L.-J. Heterostructures based on two-dimensional layered materials and their potential applications. *Materials Today* **19,** 322–335. doi:10.1016/J.MATTOD.2015.11.003 (2016).

[45] Qi, H. *et al.* Production methods of van der Waals heterostructures based on transition metal dichalcogenides. *Crystals* **8,** 35. doi:10.3390/cryst8010035 (2018).

[46] Zomer, P. J., Guimarães, M. H. D., Brant, J. C., Tombros, N. & van Wees, B. J. Fast pick up technique for high quality heterostructures of bilayer graphene and hexagonal boron nitride. *Applied Physics Letters* **105,** 013101. doi:10.1063/1.4886096 (2014).

[47] Haigh, S. J. *et al.* Cross-sectional imaging of individual layers and buried interfaces of graphene-based heterostructures and superlattices. *Nature Materials* **11,** 764–767. doi:10.1038/nmat3386 (2012).

[48] Cao, Y. *et al.* Quality heterostructures from two-dimensional crystals unstable in air by their assembly in inert atmosphere. *Nano Letters* **15,** 4914–4921. doi:10.1021/acs.nanolett.5b00648 (2015).

[49] Liu, Y. *et al.* Toward barrier free contact to molybdenum disulfide using graphene electrodes. *Nano Letters* **15,** 3030–3034. doi:10.1021/nl504957p (2015).

[50] Wang, Y., Wang, Z., Yao, W., Liu, G.-B. & Yu, H. Interlayer coupling in commensurate and incommensurate bilayer structures of transition-metal dichalcogenides. *Physical Review B* **95,** 115429. doi:10.1103/PhysRevB.95.115429 (2017).

[51] Chuang, H.-J. *et al.* Low-resistance 2D/2D ohmic contacts: A universal approach to high-performance WSe2, MoS2, and MoSe2 transistors. *Nano Letters* **16,** 1896–1902. doi:10.1021/acs.nanolett.5b05066 (2016).

[52] Xu, Y. *et al.* Contacts between two- and three-dimensional materials: Ohmic, schottky, and p – n heterojunctions. *ACS Nano* **10,** 4895–4919. doi:10.1021/acsnano.6b01842 (2016).

[53] Stradi, D., Papior, N. R., Hansen, O. & Brandbyge, M. Field effect in graphene-based van der Waals heterostructures: Stacking sequence matters. *Nano Letters* **17,** 2660–2666. doi:10.1021/acs.nanolett.7b00473 (2017).

[54] Wang, L. *et al.* One-dimensional electrical contact to a two-dimensional material. *Science* **342,** 614–617. doi:10.1126/science.1244358 (2013).

[55] Zhao, Y. *et al.* Doping, contact and interface engineering of two-dimensional layered transition metal dichalcogenides transistors. *Advanced Functional Materials* **27,** 1603484. doi:10.1002/adfm.201603484 (2017).

[56] Allain, A., Kang, J., Banerjee, K. & Kis, A. Electrical contacts to two-dimensional semiconductors. *Nature materials* **14,** 1195–205. doi:10.1038/nmat4452 (2015).

[57] Gong, C., Colombo, L., Wallace, R. M. & Cho, K. The unusual mechanism of partial Fermi level pinning at metal–MoS2 interfaces. *Nano Letters* **14,** 1714–1720. doi:10.1021/nl403465v (2014).

[58] Geim, A. K. & Novoselov, K. S. The rise of graphene. *Nature Materials* **6,** 183–191. doi:10.1038/nmat1849 (2007).

[59] Withers, F. *et al.* Light-emitting diodes by band-structure engineering in van der Waals heterostructures. *Nano Letters* **15,** 8223–8228. doi:10.1038/NMAT4205 (2015).

[60] Andrei, E. Y., Li, G. & Du, X. Electronic properties of graphene: a perspective from scanning tunneling microscopy and magnetotransport. *Reports on Progress in Physics* **75,** 056501. doi:10.1088/0034-4885/75/5/056501 (2012).

[61] Yu, Y.-J. *et al.* Tuning the graphene work function by electric field effect. *Nano Letters* **9,** 3430–3434. doi:10.1021/nl901572a (2009).

[62] Zhao, L. *et al.* Influence of copper crystal surface on the CVD growth of large area monolayer graphene. *Solid State Communications* **151,** 509–513. doi:10.1016/j.ssc.2011.01.014 (2011).

[63] Roy, T. *et al.* Field-effect transistors built from all two-dimensional material components. *ACS Nano* **8,** 6259–6264. doi:10.1021/nn501723y (2014).

[64] Britnell, L. *et al.* Field-effect tunneling transistor based on vertical graphene heterostructures. *Science* **335,** 947–950. doi:10.1126/science.1218461 (2012).

[65] Gong, C. *et al.* Band alignment of two-dimensional transition metal dichalcogenides: Application in tunnel field effect transistors. *Applied Physics Letters* **103,** 053513. doi:10.1063/1.4817409 (2013).

[66] Wang, H., Fan, F., Zhu, S. & Wu, H. Doping enhanced ferromagnetism and induced half-metallicity in CrI3 monolayer. *EPL (Europhysics Letters)* **114,** 47001. doi:10.1209/0295-5075/114/47001 (2016).

[67] Rivera, P. *et al.* Observation of long-lived interlayer excitons in monolayer MoSe2–WSe2 heterostructures. *Nature Communications* **6,** 6242. doi:10.1038/ncomms7242 (2015).

[68] Kim, B. S. *et al.* Possible electric field induced indirect to direct band gap transition in MoSe2. *Scientific Reports* **7,** 5206. doi:10.1038/s41598-017-05613-5 (2017).

[69] Chang, T.-R., Lin, H., Jeng, H.-T. & Bansil, A. Thickness dependence of spin polarization and electronic structure of ultra-thin films of MoS2 and related transition-metal dichalcogenides. *Scientific Reports* **4,** 6270. doi:10.1038/srep06270 (2015).

[70] Cha, S. *et al.* Generation, transport and detection of valley-locked spin photocurrent in WSe2–graphene–Bi2Se3 heterostructures. *Nature Nanotechnology* **13,** 910–914. doi:10.1038/s41565-018-0195-y (2018).

[71] Tomadin, A., Guinea, F. & Polini, M. Generation and morphing of plasmons in graphene superlattices. *Physical Review B* **90,** 161406. doi:10.1103/PhysRevB.90.161406 (2014).

[72] Cotrufo, M., Sun, L., Choi, J., Alù, A. & Li, X. Enhancing functionalities of atomically thin semiconductors with plasmonic nanostructures. *Nanophotonics* **8,** 577–598. doi:10.1515/nanoph-2018-0185 (2019).

[73] Lv, B., Qian, T. & Ding, H. Angle-resolved photoemission spectroscopy and its application to topological materials. *Nature Reviews Physics,* 1–18. doi:10.1038/s42254-019-0088-5 (2019).

[74] Ohta, T., Bostwick, A., Seyller, T., Horn, K. & Rotenberg, E. Controlling the electronic structure of bilayer graphene. *Science* **313,** 951–954. doi:10.1126/science.1130681 (2006).

[75] Yuan, H. *et al.* Evolution of the valley position in bulk transition-metal chalcogenides and their monolayer limit. *Nano Letters* **16,** 4738–4745. doi:10.1021/acs.nanolett.5b05107 (2016).

[76] Riley, J. M. *et al.* Direct observation of spin-polarized bulk bands in an inversion-symmetric semiconductor. *Nature Physics* **10,** 835–839. doi:10.1038/nphys3105 (2014).

[77] Pan, Z.-H. *et al.* Electronic structure of the topological insulator Bi2Se3 using angle-resolved photoemission spectroscopy: Evidence for a nearly full surface spin polarization. *Physical Review Letters* **106,** 257004. doi:10.1103/PhysRevLett.106.257004 (2011).

[78] Hart, L. S. *et al.* Electronic bandstructure and van der Waals coupling of ReSe2 revealed by high-resolution angle-resolved photoemission spectroscopy. *Scientific Reports* **7,** 5145. doi:10.1038/s41598-017-05361-6 (2017).

[79] Han, C. Q. *et al.* Electronic structure of black phosphorus studied by angle-resolved photoemission spectroscopy. *Physical Review B* **90,** 085101. doi:10.1103/PhysRevB.90.085101 (2014).

[80] Kim, B. S. *et al.* Determination of the band parameters of bulk 2H-MX2 (M = Mo, W; X = S, Se) by angle-resolved photoemission spectroscopy. *Scientific Reports* **6,** 36389. doi:10.1038/srep36389 (2016).

[81] Alidoust, N. *et al.* Observation of monolayer valence band spin-orbit effect and induced quantum well states in MoX2. *Nature communications* **5,** 4673. doi:10.1038/ncomms5673 (2014).

[82] Tanabe, I. *et al.* Band structure characterization of WS2 grown by chemical vapor deposition. *Applied Physics Letters.* doi:10.1063/1.4954278 (2016).

[83] Jin, W. *et al.* Direct measurement of the thickness-dependent electronic band structure of MoS2 using angle-resolved photoemission spectroscopy. *Physical Review Letters* **111,** 106801. doi:10.1103/PhysRevLett.111.106801 (2013).

[84] Yeh, P.-C. *et al.* Layer-dependent electronic structure of an atomically heavy two-dimensional dichalcogenide. *Physical Review B* **91,** 041407. doi:10.1103/PhysRevB.91.041407 (2015).

[85] Hamer, M. J. *et al.* Indirect to direct gap crossover in two-dimensional InSe revealed by angle-resolved photoemission spectroscopy. *ACS Nano,* acsnano. 8b08726. doi:10.1021/acsnano.8b08726 (2019).

[86] Chen, P. *et al.* Charge density wave transition in single-layer titanium diselenide. *Nature Communications* **6,** 8943. doi:10.1038/ncomms9943 (2015).

[87] Coy Diaz, H. *et al.* Direct observation of interlayer hybridization and dirac relativistic carriers in graphene/MoS2 van der Waals heterostructures. *Nano Letters* **15,** 1135–1140. doi:10.1021/nl504167y (2015).

[88] Wilson, N. R. *et al.* Determination of band offsets, hybridization, and exciton binding in 2D semiconductor heterostructures. *Science Advances* **3,** e1601832. doi:10.1126/sciadv.1601832 (2017).

[89] Eda, G. *et al.* Photoluminescence from chemically exfoliated MoS2. *Nano Letters* **11,** 5111–5116. doi:10.1021/nl201874w (2011).

[90] Ramasubramaniam, A. Large excitonic effects in monolayers of molybdenum and tungsten dichalcogenides. *Physical Review B* **86,** 115409. doi:10.1103/PhysRevB.86.115409 (2012).

[91] Chiu, M.-H. *et al.* Determination of band alignment in the single-layer MoS2/ WSe2 heterojunction. *Nature Communications* **6,** 7666. doi:10.1038/ncomms8666 (2015).

[92] Zhang, Y. *et al.* Electronic structure, surface doping, and optical response in epitaxial WSe2 thin films. *Nano Letters* **16,** 2485–2491. doi:10.1021/acs.nanolett.6b00059 (2016).

[93] Mak, K. F. *et al.* Tightly bound trions in monolayer MoS2. *Nature Materials* **12,** 207–211. doi:10.1038/nmat3505 (2013).

[94] Le Quang, T. *et al.* Scanning tunneling spectroscopy of van der Waals graphene/ semiconductor interfaces: Absence of Fermi level pinning. *2D Materials* **4,** 035019. doi:10.1088/2053-1583/aa7b03 (2017).

[95] Zhou, X. *et al.* Atomic-scale spectroscopy of gated monolayer MoS2. *Nano Letters* **16,** 3148–3154. doi:10.1021/acs.nanolett.6b00473 (2016).

[96] Hsu, W.-T. *et al.* Evidence of indirect gap in monolayer WSe2. *Nature Communications* **8,** 929. doi:10.1038/s41467-017-01012-6 (2017).

[97] Rigosi, A. F., Hill, H. M., Rim, K. T., Flynn, G. W. & Heinz, T. F. Electronic band gaps and exciton binding energies in monolayer Mo(x)W(1-x)S2 transition metal dichalcogenide alloys probed by scanning tunneling and optical spectroscopy. *Physical Review B* **94,** 075440. doi:10.1103/PhysRevB.94.075440 (2016).

[98] Saito, R., Tatsumi, Y., Huang, S., Ling, X. & Dresselhaus, M. S. Raman spectroscopy of transition metal dichalcogenides. *Journal of Physics: Condensed Matter* **28,** 353002. doi:10.1088/0953-8984/28/35/353002 (2016).

[99] Zhang, X. *et al.* Phonon and Raman scattering of two-dimensional transition metal dichalcogenides from monolayer, multilayer to bulk material. *Chemical Society Reviews* **44,** 2757–2785. doi:10.1039/C4CS00282B (2015).

[100] Mlack, J. T. *et al.* Transfer of monolayer TMD WS2 and Raman study of substrate effects. *Scientific Reports* **7,** 43037. doi:10.1038/srep43037 (2017).

[101] Schmidt, H., Giustiniano, F. & Eda, G. Electronic transport properties of transition metal dichalcogenide field-effect devices: Surface and interface effects. *Chemical Society Reviews* **44,** 7715–7736. doi:10.1039/C5CS00275C (2015).

[102] Kang, M. *et al.* Universal mechanism of band-gap engineering in transition-metal dichalcogenides. *Nano Letters* **17,** 1610–1615. doi:10.1021/acs.nanolett.6b04775 (2017).

[103] Zhang, Y. *et al.* Direct observation of the transition from indirect to direct bandgap in atomically thin epitaxial MoSe2. *Nature Nanotechnology* **9,** 111–115. doi:10.1038/nnano.2013.277 (2014).

[104] Eknapakul, T. *et al.* Electronic structure of a quasi-freestanding MoS2 monolayer. *Nano Letters* **14,** 1312–1316. doi:10.1021/nl4042824 (2014).

[105] Riley, J. M. *et al.* Negative electronic compressibility and tunable spin splitting in WSe2. *Nature Nanotechnology* **10,** 1043–1047. doi:10.1038/nnano.2015.217 (2015).

[106] Katoch, J. *et al.* Giant spin-splitting and gap renormalization driven by trions in single-layer WS2/h-BN heterostructures. *Nature Physics* **14,** 355–359. doi:10.1038/s41567-017-0033-4 (2018).

[107] Joucken, F. *et al.* Visualizing the effect of an electrostatic gate with angle-resolved photoemission spectroscopy. *Nano Letters* **19,** 2682–2687. doi:10.1021/acs.nanolett.9b00649 (2019).

[108] Hüfner, S. *Photoelectron spectroscopy* 3rd. doi:10.1007/978-3-662-09280-4 (Springer Berlin Heidelberg, Berlin, Heidelberg, 2003).

[109] Damascelli, A., Hussain, Z. & Shen, Z.-X. Angle-resolved photoemission studies of the cuprate superconductors. *Reviews of Modern Physics* **75,** 473–541. doi:10.1103/RevModPhys.75.473 (2003).

[110] Moser, S. An experimentalist's guide to the matrix element in angle resolved photoemission. *Journal of Electron Spectroscopy and Related Phenomena* **214,** 29–52. doi:10.1016/j.elspec.2016.11.007 (2017).

[111] Suga, S. & Sekiyama, A. *Photoelectron spectroscopy* 3rd, 662. doi:10.1007/978-3-642-37530-9 (Springer Berlin Heidelberg, Berlin, Heidelberg, 2014).

[112] Gierz, I., Henk, J., Höchst, H., Ast, C. R. & Kern, K. Illuminating the dark corridor in graphene: Polarization dependence of angle-resolved photoemission spectroscopy on graphene. *Physical Review B* **83,** 121408. doi:10.1103/PhysRevB.83.121408 (2011).

[113] Seah, M. P. & Dench, W. A. Quantitative electron spectroscopy of surfaces: A standard data base for electron inelastic mean free paths in solids. *Surface and Interface Analysis* **1,** 2–11. doi:10.1002/sia.740010103 (1979).

[114] Hoffman, P. *Surface Physics: An Introduction* (Hoffman, P., 2013).

[115] Mudd, J. J. *Photoelectron Spectroscopy Investigation of CdO* PhD thesis (The University of Warwick, 2014).

[116] Horikawa, Y. Resolution of annular-pupil optical systems. *Journal of the Optical Society of America A* **11,** 1985. doi:10.1364/JOSAA.11.001985 (1994).

[117] Rösner, B., Dudin, P., Bosgra, J., Hoesch, M. & David, C. Zone plates for angle-resolved photoelectron spectroscopy providing sub-micrometre resolution in the extreme ultraviolet regime. *Journal of Synchrotron Radiation* **26,** 467–472. doi:10.1107/S1600577519000869 (2019).

[118] Dudin, P. *et al.* Angle-resolved photoemission spectroscopy and imaging with a submicrometre probe at the SPECTROMICROSCOPY-3.2L beamline of Elettra. *Journal of Synchrotron Radiation* **17,** 445–450. doi:10.1107/S0909049510013993 (2010).

[119] *https://www.elettra.eu/ lightsources/ elettra/elettra-beamlines/ spectro- microscopy/ beamline/all.html. (Accessed: 2019-08-06)*

[120] Kandyba, V. *Electronic structure of single and few layered graphene studied by angle resolved photoemission spectro-microscopy.* PhD thesis (Università degli Studi di Trieste, 2018).

[121] *https://www.diamond.ac.uk/ Instruments/ Structures-and-Surfaces/ I05/ status.html. (Accessed: 2019-07-29)*

[122] *www.scientaomicron.com/ en/ products/ 353/ 1230. (Accessed: 2019-08-19)*

[123] *www.diamond.ac.uk/ Instruments/ Structures-and-Surfaces/ I05/ methods.html. (Accessed: 2019-08-19)*

[124] Avila, J. *et al.* ANTARES, a scanning photoemission microscopy beamline at SOLEIL. *Journal of Physics: Conference Series* **425,** 192023. doi:10.1088/1742-6596/425/19/192023 (2013).

[125] Meyer, E., Hug, H. J. & Bennewitz, R. *Scanning probe microscopy* 210. doi:10.1007/978-3-662-09801-1 (Springer Berlin Heidelberg, Berlin, Heidelberg, 2004).

[126] Duman, M. *et al.* in *Encyclopedia of Biophysics* 1–14 (Springer Berlin Heidelberg, Berlin, Heidelberg, 2018). doi:10.1007/978-3-642-35943-9_496-1.

[127] Nguyen, P. V. *et al.* Visualizing electrostatic gating effects in two-dimensional heterostructures. *Nature* **572,** 220–223. doi:10.1038/s41586-019-1402-1 (2019).

[128] *www.spmtips.com/afm-tip-hq-nsc18-al-bs. (Accessed: 2019-08-07)*

[129] Rivera, P. *et al.* Interlayer valley excitons in heterobilayers of transition metal dichalcogenides. *Nature Nanotechnology* **13,** 1004–1015. doi:10.1038/s41565-018-0193-0 (2018).

[130] Novoselov, K. S. *et al.* A roadmap for graphene. *Nature* **490,** 192–200. doi:10.1038/nature11458 (2012).

[131] Butler, S. Z. *et al.* Progress, challenges, and opportunities in two-dimensional materials beyond graphene. *ACS Nano* **7,** 2898–2926. doi:10.1021/nn400280c (2013).

[132] Mas-Ballesté, R., Gómez-Navarro, C., Gómez-Herrero, J. & Zamora, F. 2D materials: to graphene and beyond. *Nanoscale* **3,** 20–30. doi:10.1039/C0NR00323A (2011).

[133] Bhimanapati, G. R. *et al.* Recent advances in two-dimensional materials beyond graphene. *ACS Nano* **9,** 11509–11539. doi:10.1021/acsnano.5b05556 (2015).

[134] Kang, J., Tongay, S., Zhou, J., Li, J. & Wu, J. Band offsets and heterostructures of two-dimensional semiconductors. *Applied Physics Letters* **102,** 012111. doi:10.1063/1.4774090 (2013).

[135] Chiu, M.-H. *et al.* Band alignment of 2D transition metal dichalcogenide heterojunctions. *Advanced Functional Materials* **27,** 1603756. doi:10.1002/adfm.201603756 (2017).

[136] Pierucci, D. *et al.* Band alignment and minigaps in monolayer MoS2-graphene van der Waals heterostructures. *Nano Letters* **16,** 4054–4061. doi:10.1021/acs.nanolett.6b00609 (2016).

[137] Xi, X. *et al.* Strongly enhanced charge-density-wave order in monolayer NbSe2. *Nature Nanotechnology* **10,** 765–769. doi:10.1038/nnano.2015.143 (2015).

[138] Fang, H. *et al.* Strong interlayer coupling in van der Waals heterostructures built from single-layer chalcogenides. *Proceedings of the National Academy of Sciences* **111,** 6198–6202. doi:10.1073/pnas.1405435111 (2014).

[139] Lu, N. *et al.* MoS2/MX2 heterobilayers: bandgap engineering via tensile strain or external electrical field. *Nanoscale* **6,** 2879–2886. doi:10.1039/C3NR06072A (2014).

[140] Ugeda, M. M. *et al.* Giant bandgap renormalization and excitonic effects in a monolayer transition metal dichalcogenide semiconductor. *Nature Materials* **13,** 1091–1095. doi:10.1038/nmat4061 (2014).

[141] Kormányos, A. *et al.* k.p theory for two-dimensional transition metal dichalcogenide semiconductors. *2D Materials* **2,** 049501. doi:10.1088/2053-1583/2/4/049501 (2015).

[142] Rasmussen, F. A. & Thygesen, K. S. Computational 2D materials database: Electronic structure of transition-metal dichalcogenides and oxides. *The Journal of Physical Chemistry C* **119,** 13169–13183. doi:10.1021/acs.jpcc.5b02950 (2015).

[143] Zhu, Z. Y., Cheng, Y. C. & Schwingenschlögl, U. Giant spin-orbit-induced spin splitting in two-dimensional transition-metal dichalcogenide semiconductors. *Physical Review B* **84,** 153402. doi:10.1103/PhysRevB.84.153402 (2011).

[144] Liu, G. B., Shan, W. Y., Yao, Y., Yao, W. & Xiao, D. Three-band tight-binding model for monolayers of group-VIB transition metal dichalcogenides. *Physical Review B - Condensed Matter and Materials Physics.* doi:10.1103/PhysRevB.88.085433. arXiv: 1305.6089 (2013).

[145] Froehlicher, G., Lorchat, E. & Berciaud, S. Charge versus energy transfer in atomically thin graphene-transition metal dichalcogenide van der Waals heterostructures. *Physical Review X* **8,** 011007. doi:10.1103/PhysRevX.8.011007 (2018).

[146] Ryou, J., Kim, Y.-S., KC, S. & Cho, K. Monolayer MoS2 bandgap modulation by dielectric environments and tunable bandgap transistors. *Scientific Reports* **6,** 29184. doi:10.1038/srep29184 (2016).

[147] Song, J. C. W. & Gabor, N. M. Electron quantum metamaterials in van der Waals heterostructures. *Nature Nanotechnology* **13,** 986–993. doi:10.1038/s41565-018-0294-9 (2018).

[148] Vancsó, P. *et al.* The intrinsic defect structure of exfoliated MoS2 single layers revealed by scanning tunneling microscopy. *Scientific Reports* **6,** 29726. doi:10.1038/srep29726 (2016).

[149] Hong, J. *et al.* Exploring atomic defects in molybdenum disulphide monolayers. *Nature Communications* **6,** 6293. doi:10.1038/ncomms7293 (2015).

[150] Rai, A. *et al.* Progress in contact, doping and mobility engineering of MoS2: An atomically thin 2D semiconductor. *Crystals* **8,** 316. doi:10.3390/cryst8080316 (2018).

[151] Constantinescu, G. C. & Hine, N. D. M. Energy landscape and band-structure tuning in realistic MoS2/MoSe2 heterostructures. *Physical Review B* **91,** 195416. doi:10.1103/PhysRevB.91.195416 (2015).

[152] Woods, C. R. *et al.* Commensurate–incommensurate transition in graphene on hexagonal boron nitride. *Nature Physics* **10,** 451–456. doi:10.1038/nphys2954 (2014).

[153] Su, J. *et al.* Unusual properties and potential applications of strain BN-MS2 (M = Mo, W) heterostructures. *Scientific Reports* **9,** 3518. doi:10.1038/s41598-019-39970-0 (2019).

[154] Velický, M. & Toth, P. S. From two-dimensional materials to their heterostructures: An electrochemist's perspective. *Applied Materials Today* **8,** 68–103. doi:10.1016/j.apmt.2017.05.003 (2017).

[155] Schulman, D. S., Arnold, A. J. & Das, S. Contact engineering for 2D materials and devices. *Chemical Society Reviews* **47,** 3037–3058. doi:10.1039/C7CS00828G (2018).

[156] Qian, X., Wang, Y., Li, W., Lu, J. & Li, J. Modelling of stacked 2D materials and devices. *2D Materials* **2,** 032003. doi:10.1088/2053-1583/2/3/032003 (2015).

[157] Yankowitz, M., McKenzie, D. & LeRoy, B. J. Local spectroscopic characterization of spin and layer polarization in WSe2. *Physical Review Letters* **115,** 136803. doi:10.1103/PhysRevLett.115.136803 (2015).

[158] Zhang, C. *et al.* Probing critical point energies of transition metal dichalcogenides: surprising indirect gap of single layer WSe2. *Nano Letters* **15,** 6494–6500. doi:10.1021/acs.nanolett.5b01968 (2015).

[159] He, K. *et al.* Tightly bound excitons in monolayer WSe2. *Physical Review Letters* **113,** 026803. doi:10.1103/PhysRevLett.113.026803 (2014).

[160] Park, S. *et al.* Direct determination of monolayer MoS2 and WSe2 exciton binding energies on insulating and metallic substrates. *2D Materials* **5,** 025003. doi:10.1088/2053-1583/aaa4ca (2018).

[161] Stier, A. V. *et al.* Magnetooptics of exciton rydberg states in a monolayer semiconductor. *Physical Review Letters* **120,** 057405. doi:10.1103/PhysRevLett.120.057405 (2018).

[162] Bostwick, A., Ohta, T., Seyller, T., Horn, K. & Rotenberg, E. Quasiparticle dynamics in graphene. *Nature Physics* **3,** 36–40. doi:10.1038/nphys477 (2007).

[163] Yu, G. L. *et al.* Interaction phenomena in graphene seen through quantum capacitance. *Proceedings of the National Academy of Sciences* **110,** 3282–3286. doi:10.1073/pnas.1300599110 (2013).

[164] Siegel, D. A., Regan, W., Fedorov, A. V., Zettl, A. & Lanzara, A. Charge-carrier screening in single-layer graphene. *Physical Review Letters* **110,** 146802. doi:10.1103/PhysRevLett.110.146802 (2013).

[165] Kim, K. K. *et al.* Synthesis and characterization of hexagonal Boron Nitride film as a dielectric layer for graphene devices. *ACS Nano* **6,** 8583–8590. doi:10.1021/nn301675f (2012).

[166] Yan, T., Qiao, X., Liu, X., Tan, P. & Zhang, X. Photoluminescence properties and exciton dynamics in monolayer WSe2. *Applied Physics Letters* **105,** 101901. doi:10.1063/1.4895471 (2014).

[167] Kumar, a. & Ahluwalia, P. K. Electronic structure of transition metal dichalcogenides monolayers 1H-MX2 (M = Mo, W; X = S, Se, Te) from ab-initio theory: New direct band gap semiconductors. *The European Physical Journal B* **85,** 186. doi:10.1140/epjb/e2012-30070-x (2012).

[168] Gao, S. & Yang, L. Renormalization of the quasiparticle band gap in doped two-dimensional materials from many-body calculations. *Physical Review B* **96,** 155410. doi:10.1103/PhysRevB.96.155410 (2017).

[169] Coy-Diaz, H. *et al.* Band renormalization and spin polarization of MoS2 in graphene/MoS2 heterostructures. *physica status solidi (RRL) - Rapid Research Letters* **9,** 701–706. doi:10.1002/pssr.201510346 (2015).

[170] Raja, A. *et al.* Coulomb engineering of the bandgap and excitons in two-dimensional materials. *Nature Communications* **8,** 15251. doi:10.1038/ncomms15251 (2017).

[171] Liu, Y. *et al.* Gate-tunable giant stark effect in few-layer black phosphorus. *Nano Letters* **17,** 1970–1977. doi:10.1021/acs.nanolett.6b05381 (2017).

[172] Tong, Q. *et al.* Topological mosaics in moiré superlattices of van der Waals heterobilayers. *Nature Physics* **13,** 356–362. doi:10.1038/nphys3968 (2017).

[173] Cao, Y. *et al.* Unconventional superconductivity in magic-angle graphene superlattices. *Nature* **556,** 43–50. doi:10.1038/nature26160 (2018).

[174] Cao, Y. *et al.* Correlated insulator behaviour at half-filling in magic-angle graphene superlattices. *Nature* **556,** 80–84. doi:10.1038/nature26154 (2018).

[175] Yu, W. J. *et al.* Highly efficient gate-tunable photocurrent generation in vertical heterostructures of layered materials. *Nature Nanotechnology* **8,** 952–958. doi:10.1038/nnano.2013.219 (2013).

[176] Larentis, S. *et al.* Band offset and negative compressibility in graphene-MoS2 heterostructures. *Nano Letters* **14,** 2039–2045. doi:10.1021/nl500212s (2014).

[177] Moriya, R. *et al.* Influence of the density of states of graphene on the transport properties of graphene/MoS2/metal vertical field-effect transistors. *Applied Physics Letters* **106,** 223103. doi:10.1063/1.4921920 (2015).

[178] Kliros, G. in *Graphene Science Handbook* 1st, 171–183 (CRC Press, 2016). doi:10.1201/b19460-15.

[179] Xia, J., Chen, F., Li, J. & Tao, N. Measurement of the quantum capacitance of graphene. *Nature Nanotechnology* **4,** 505–509. doi:10.1038/nnano.2009.177 (2009).

[180] Kim, K. *et al.* Band alignment in WSe2-graphene heterostructures. *ACS Nano* **9,** 4527–4532. doi:10.1021/acsnano.5b01114 (2015).

[181] Purdie, D. G. *et al.* Cleaning interfaces in layered materials heterostructures. *Nature Communications* **9,** 5387. doi:10.1038/s41467-018-07558-3 (2018).

[182] Liu, H. *et al.* Dense network of one-dimensional midgap metallic modes in monolayer MoSe2 and their spatial undulations. *Physical Review Letters* **113,** 066105. doi:10.1103/PhysRevLett.113.066105 (2014).

[183] Yang, Z. *et al.* A Fermi-level-pinning-free 1D electrical contact at the intrinsic 2D MoS2-Metal junction. *Advanced Materials* **31,** 1808231. doi:10.1002/adma.201808231 (2019).

[184] Lang, D. V. & Henry, C. H. Scanning photocurrent microscopy: A new technique to study inhomogeneously distributed recombination centers in semiconductors. *Solid-State Electronics* **21,** 1519–1524. doi:10.1016/0038-1101(78)90235-6 (1978).

[185] Graham, R. & YU, D. Scanning photocurrent microscopy in semiconductor nanostructures. *Modern Physics Letters B* **27,** 1330018. doi:10.1142/S0217984913300184 (2013).

[186] Graham, R., Miller, C., Oh, E. & Yu, D. Electric field dependent photocurrent decay length in single lead sulfide nanowire field effect transistors. *Nano Letters* **11,** 717–722. doi:10.1021/nl1038456 (2011).

[187] Sze, S. M. & Ng, K. K. *Physics of semiconductor devices* 815 (Wiley - Interscience, 2007).

[188] Dan, Y., Zhao, X., Chen, K. & Mesli, A. A photoconductor intrinsically has no gain. *ACS Photonics* **5,** 4111–4116. doi:10.1021/acsphotonics.8b00805 (2018).

[189] Poindexter, J. R., Barnard, E. S., Kurchin, R. C. & Buonassisi, T. Charge-carrier lifetime measurements in early-stage photovoltaic materials: intuition, uncertainties, and opportunities. arXiv: 1805.05832 (2018).

[190] Doan, T. C., Li, J., Lin, J. Y. & Jiang, H. X. Growth and device processing of hexagonal boron nitride epilayers for thermal neutron and deep ultraviolet detectors. *AIP Advances* **6,** 075213. doi:10.1063/1.4959595 (2016).

[191] Ahmed, K. *et al.* Solid-state neutron detectors based on thickness scalable hexagonal boron nitride. *Applied Physics Letters* **110,** 023503. doi:10.1063/1.4973927 (2017).

[192] Dahal, R. *et al.* Anisotropic charge carrier transport in free-standing hexagonal boron nitride thin films. *Applied Physics Express* **9,** 065801. doi:10.7567/APEX.9.065801 (2016).

[193] Palermo, V., Palma, M. & Samorì, P. Electronic characterization of organic thin films by Kelvin probe force microscopy. *Advanced Materials* **18,** 145–164. doi:10.1002/adma.200501394 (2006).

[194] Glatzel, T., Sadewasser, S. & Lux-Steiner, M. Amplitude or frequency modulation - detection in Kelvin probe force microscopy. *Applied Surface Science* **210,** 84–89. doi:10.1016/S0169-4332(02)01484-8 (2003).

[195] Giessibl, F. J. Forces and frequency shifts in atomic-resolution dynamic-force microscopy. *Physical Review B* **56,** 16010–16015. doi:10.1103/PhysRevB.56.16010 (1997).

[196] Ziegler, D. & Stemmer, A. Force gradient sensitive detection in lift-mode Kelvin probe force microscopy. *Nanotechnology* **22,** 075501. doi:10.1088/0957-4484/22/7/075501 (2011).

[197] Melitz, W., Shen, J., Kummel, A. C. & Lee, S. Kelvin probe force microscopy and its application. *Surface Science Reports* **66,** 1–27. doi:10.1016/j.surfrep.2010.10.001 (2011).

[198] Feng, J. *et al.* Electronic structure and enhanced charge-density wave order of monolayer VSe2. *Nano Letters* **18,** 4493–4499. doi:10.1021/acs.nanolett.8b01649 (2018).

[199] Wu, M., Li, Z., Cao, T. & Louie, S. G. Physical origin of giant excitonic and magneto-optical responses in two-dimensional ferromagnetic insulators. *Nature Communications* **10,** 2371. doi:10.1038/s41467-019-10325-7 (2019).

[200] Song, J.-G. *et al.* Controllable synthesis of molybdenum tungsten disulfide alloy for vertically composition-controlled multilayer. *Nature Communications* **6,** 7817. doi:10.1038/ncomms8817 (2015).

[201] Dumcenco, D. O., Kobayashi, H., Liu, Z., Huang, Y.-S. & Suenaga, K. Visualization and quantification of transition metal atomic mixing in Mo(1-x)W(x)S2 single layers. *Nature Communications* **4,** 1351. doi:10.1038/ncomms2351 (2013).

[202] Yoshida, S. *et al.* Microscopic basis for the band engineering of Mo(1-x) W(x) S2- based heterojunction. *Scientific Reports.* doi:10.1038/srep14808 (2015).

[203] Zhang, C. *et al.* Interlayer couplings, Moiré patterns, and 2D electronic superlattices in MoS2/WSe2 hetero-bilayers. *Science Advances* **3,** e1601459. doi:10.1126/sciadv.1601459 (2017).

[204] Joshi, V. K. Spintronics: A contemporary review of emerging electronics devices. *Engineering Science and Technology, an International Journal* **19,** 1503–1513. doi:10.1016/j.jestch.2016.05.002 (2016).

[205] Wang, H. *et al.* Integrated circuits based on bilayer MoS2 transistors. *Nano Letters* **12,** 4674–4680. doi:10.1021/nl302015v (2012).

[206] Bawden, L. *et al.* Spin–valley locking in the normal state of a transition-metal dichalcogenide superconductor. *Nature Communications* **7,** 11711. doi:10.1038/ncomms11711 (2016).

[207] Mueller, T. & Malic, E. Exciton physics and device application of two-dimensional transition metal dichalcogenide semiconductors. *npj 2D Materials and Applications* **2,** 29. doi:10.1038/s41699-018-0074-2 (2018).